TECHNISCHE UNIVERSITÄT MÜNCHEN

Fakultät für Physik

Oskar-von-Miller Lehrstuhl für Wissenschaftskommunikation

From aromatic molecules to nanoarchitectures: Influencing factors in on-surface synthesis

Matthias Rudolf Lischka

Vollständiger Abdruck der von der Fakultät für Physik der Technischen Universität München zur Erlangung des akademischen Grades eines

Doktors der Naturwissenschaften

(Dr. rer. nat.)

genehmigten Dissertation.

Vorsitzender: Prof. Dr. Martin Zacharias

Prüfer der Dissertation:

1. Priv.-Doz. Dr. Markus Lackinger

2. Prof. Dr. Wilhelm Auwärter

Die Dissertation wurde am 24.09.2018 bei der Technischen Universität München eingereicht und durch die Fakultät für Physik am 24.12.2018 angenommen.

Abstract

The present thesis reports the bottom-up approach to create 1D and 2D organic nanostructures by on-surface polymerization on the basis of functionalized arene molecules. The experiments were carried out on metal single crystal surfaces under defined ultra high vacuum conditions. Two well established on-surface polymerization strategies and coupling reactions were studied: surface-assisted Ullmann coupling and surface-mediated metal-organic coordination. The polymerization pathway and coupling mechanism was studied by a complementary approach of surface-sensitive analysis methods. Scanning Tunneling Microscopy provides structural information in real space with submolecular resolution and was complemented by measurements of core level binding energies by X-ray Photoelectron Spectroscopy to obtain information on chemical alterations. Near Edge X-ray Absorption Fine Structure enables detailed insights in unoccupied orbitals and gives further information of geometrical and chemical structures of the polymers, respectively. This thesis includes three studies of the on-surface synthesis of molecular building blocks into polymers to gain further insights in reaction parameters and influencing factors, respectively. The core findings for the surface-assisted Ullmann reaction are: (1) Steric hindrance between two pyrene molecular building blocks prevents covalent coupling and likewise the formation of a flat adsorbed polymer structure, even upon a hierarchical polymerization. (2) The steric hindrance leads to strong C-Au-C linkages on Au(111) and consequently to highly stable organometallic structures shown as organometallic chain formation. On Ag(111) the same molecular building block desorbs from the surface by equal thermal treatment. (3) For another molecular building block the influence of conformational mechanics is shown with a large dihedral angle between the phenyl rings, thus the formation of organometallic chains. The competitive study of a perfluorinated and a hydrogenated four-fold brominated biphenyl tecton leads to an initial 1D organometallic chain formation induced by a didebromination. The site-selectivity is achieved by the large dihedral angle of the precursor, as a result of the intramolecular steric hindrance. (4) Furthermore, the perflourination leads to an unique polymorphism and an unprecedented temperature stability up to 300 °C for organometallic nanostructures, whereas the hydrogenated analogue becomes covalently interlinked after heating to 200 °C. (5) The perfluorinated molecule, in contrast to the hydrogenated analogue, also exhibited larger organometallic domains. A possible explanation could be a higher surface mobility of the tectons by a less strong

interaction of the molecules with the surface by an increased dihedral angle through the intramolecular fluorine-fluorine repulsion. The study of a surface-mediated metal-organic coordination with a hexaaminotriphenylene molecule yielded the following results: (1) Compared to the polymerization of metal-organic coordination structures at the liquid / air interface, a bond reversibility is suppressed by on-surface synthesis. The absence of the liquid subphase hinders an extended growth of organic networks. (2) Preferred adsorption-sites of the aromatic compound and the intrinsic Cu_3 metal coordination centers hamper network formation. (3) Applying a more reactive extrinsic adatom as metal coordination center, the functional amino sites are initially activated by dehydrogenation, followed by metal-organic bond formation. The multitopic coordination leads to strong metal-organic bond formation and excludes a bond reversibility. As a consequence, for this surface-mediated reaction an extended and defect-free 2D nanostructure is not achieved. Nevertheless, the gained information of on-surface synthesis will serve as basis for further developments.

Zusammenfassung

Die vorliegende Arbeit beschreibt den experimentellen Ansatz, 1D und 2D Nanostrukturen mittels bottum-up Strategie auf Basis einer oberflächeninitiierten Polymerisation von funktionalisierten aromatischen Molekülen herzustellen. Die Experimente wurden auf Metalleinkristall-Oberflächen unter definierten Bedingungen des Ultrahochvakuums durchgeführt. Es wurden zwei etablierte oberflächenbasierte Polymerisationsstrategien und Verknüpfungsreaktionen fortführend untersucht: Die Ullmann Reaktion und die metallorganische Koordinationsreaktion. Der Verlauf der Polymerisation, sowie die Verknüpfungsreaktion, wurden durch einen komplementären Ansatz von oberflächensensitiven Messmethoden untersucht. Die Rastertunnelmikroskopie lieferte Realraum Abbildungen der Nanostrukturen mit submolekularer Auflösung, ergänzt durch Messungen der Bindungsenergie von Rumpfelektronen durch die Photoelektronenspektroskopie, um chemische Änderungen festzustellen. Röntgen-Nahkanten-Absorptions-Spektroskopie ermöglicht einen detaillierte Untersuchung der unbesetzten Zustände und liefert zusätzliche Einblicke der geometrischen und der chemischen Struktur der Polymere. Diese Arbeit beschreibt drei Fälle von Oberflächensynthese von molekularen Bausteinen zu Polymeren, um weitere Erkenntnisse der Reaktionsparameter und Einflussgrößen zu erhalten. Die wesentlichen Ergebnisse für die oberflächeninduzierte Ullmann Reaktion sind: (1) Die sterische Hinderung zwischen zwei molekularen Pyren Bausteinen verhindert eine kovalente Verknüpfung und zugleich eine flache Adsorbatstruktur, selbst bei einer hierachischen Reaktion. (2) Auf einer Au(111) Oberfläche führt die sterische Hinderung zwischen den Molekülen zu einer starken organometallischen C-Au-C Bindung, welche sich in einer höchst stabilen organometallischen Kettenstruktur widerspiegelt. Auf der Ag(111) Oberfläche hingegen, desorbieren die Moleküle von der Oberfläche bei gleicher Reaktionstemperatur. (3) Für einen anderen molekularen Baustein wurde der Einfluss der Konformation des intakten Moleküls durch den großen dihedralen Winkel zwischen den Phenylringen gezeigt, und eine daraus resultierende Formation von organometallischen Ketten. Die vergleichende Studie eines perfluorierten und hydrogenierten vierfach bromierten Biphenyl-Moleküls zeigt, dass die unmittelbar einsetzende 1D Kettenformation durch eine Didebromination induziert ist. Die Regioselektivät wird durch die starken dihedralen Winkel als Resultat der intrinsischen sterischen Abstoßung der Moleküle erreicht. (4) Zusätzlich ist hervorzuheben, dass die Perfluorierung zu einem bisher einzigartigen Polymorphismus und zu einer un-

erreichten Temperaturstabilität von organometallischen Netzwerken bis zu 300 °C geführt hat, wohingegen das hydrogenierte Vergleichsmolekül bereits ab einer Heiztemperatur von 200 °C kovalente Verknüpfungen zeigt. (5) Weiterhin zeigt das perfluorierte Molekül, im Gegensatz zu dem hydrogenierten Pendant, größere organometallische Domänen. Mögliche Ursache ist eine höhere Mobilität der Moleküle auf der Oberfläche durch eine reduzierte Wechselwirkung der molekularen Bausteine mit der Oberfläche durch einen vergrößerten dihedralen Winkel der intramolekularen Fluor-Fluor Abstoßung. Die Studie zur metallorganischen Koordination mit einem Hexaaminotriphenylen Molekül zeigte folgende Ergebnisse: (1) Im Vergleich zu einer Polymerisation des Moleküls an der flüssig / fest Grenzfläche, zeigt sich bei der Polymerisation auf Festkörperoberflächen keine Bindungsreversibilität. Die fehlende (sub)Flüssigkeitsphase hindert ein ausgedehntes Wachstum von organischen Netzwerken. (2) Bevorzugte Adsorptionsplätze der Aromaten und der intramolekularen Cu_3 Metalladatomzentren behindern eine Netwerkbildung. (3) Die Anwendung von reaktiveren extrinsischen Metallatomen als Metalladatomzentren führt zur einer initialen Aktivierung der funktionellen Aminogruppen durch eine Dehydrogenierung, gefolgt von einer metallorganischen Koordination. Die mehrfach Koordination des Metallatoms führt zu einer starken Bindungen mit den Molekülen und schließt eine Bindungsreversibilität aus. Daraus folgt, dass durch diese Oberflächenreaktion keine großflächige und defektfreie 2D Nanostruktur entsteht. Nichtsdestotrotz dienen die gewonnen Erkenntnisse der Oberflächensynthese als Grundlage für weiterführende Entwicklungen.

Contents

List of Abbreviations

Br_2I_2Py	1,6-dibromo-3,8-diiodopyrene
Br_4BP	3,3',5,5'-tetrabromobiphenyl
Br_4F_6BP	3,3',5,5'-tetrabromo-2,2',4,4',6,6'-hexafluorobiphenyl
Br_4Py	1,3,6,8-tetrabromopyrene
CHA	**c**oncentric **h**emispherical **a**nalyzer
$CONASH$	**co**ordination **na**no**sh**eet
DFT	**D**ensity **F**unctional **T**heory
E_B	**b**inding **e**nergy of electrons
E_{Kin}	**kin**etic **e**nergy of electrons
FS	**f**inal **s**tate
$FWHM$	**f**ull **w**idth at **h**alf **m**aximum
$HATP$	2,3,6,7,10,11-hexaaminotriphenylene
$HE-SGM$	**h**igh **e**nergy-**s**pherical **g**rating **m**onochromator
$LEED$	**L**ow **E**nergy **E**lectron **D**iffraction
$NEXAFS$	**N**ear **E**dge **X**-ray **A**bsorption **F**ine **S**tructure
PEY	**p**artial **e**lectron **y**ield
$QCMB$	**q**uartz **c**rystal **m**icrobalance
RT	**r**oom **t**emperature
STM	**S**canning **T**unneling **M**icroscope
TS	**t**ransition **s**tate
UHV	**u**ltra-**h**igh **v**acuum
VB	**v**alence **b**and
XPS	**X**-ray **P**hotoelectron **S**pectroscopy

1 Introduction and motivation

The discovery and characterization of graphene, the first one atom thick 2D crystal, in 2004 by Novoselov, Geim and coworkers[1] and the evidence of further thermodynamically stable natural 2D crystals,[2] leaded to a novel class of materials. 2D crystals, especially the most prominent representative graphene, have promising properties to revolutionize the information technology as silicon did in the last century. The manufacturing of extended one atom thick nanostructures in one or two dimensions affords an insight into physics and chemistry which was unattainable before and is expected to lead to novel applications in comprehensive fields, for instance spintronics, photonics, (opto)electronics, energy storage and conversion.[3] As it turned out, the fabrication of 2D crystals with tailored properties by a defined doping[4–6] is challenging. Especially, the structural quality of the crystals with focus on specific applications is not sufficient.[7]

A promising approach to manufacture one layer thin 1D and 2D nanostructures is the on-surface synthesis as bottom-up approach by the controlled interlinking of functionalized precursors (molecular building blocks). Generally, surface-assisted polymerization strategies[8,9] are straightforward and start with the deposition of the reactant, e.g. (poly)arene or porphyrine precursors,[10,11] onto crystalline metal surfaces under clean and highly defined conditions as in ultra-high vacuum. After deposition, the tectons can self-assemble by an interplay of weak hydrogen and / or halogen bonding. The final step is the activation of the precursors, for instance cleaving the leaving group from the organic backbone and the controlled interlinking into polymers. These on-surface polymerization strategies and coupling reactions lead to an unequaled high accuracy up to atomic precision,[12] whereas established top-down approaches of the semiconductor industry are diffraction limited and are not able to achieve the structural accuracy of on-surface synthesis.[10] On the other hand, polymerization strategies at the liquid / liquid and the liquid / air interfaces achieve the structural precision of on-surface synthesis, but this solution chemistry approach does not reach the extended size of on-surface synthesized nanostructures. The size of the growing structures of this solution chemistry approach is limited by an increased indissolubly depending on the size of the polymers and the nanostructures precipitate.[10]

Besides the high structural precision of the polymer, an outstanding attribute is that the functionality of these nanostructures is preprogrammed by the design

of the molecules. The number of activatable sites per precursor determines the dimensionality, e.g. ditopic functionalization leads to 1D chains or ribbons, whereas 2D reticular networks are formed by multitopic tectons, respectively. Previous studies demonstrated that on-surface polymerization is a versatile and powerful tool for manufacturing novel molecular architectures. For instance, altering the edge topology of 1D graphene nanoribbons by changing the precursor leads to spin-polarized edge states (zig-zag),[13] while the band gap (nearly metallic up to semiconduting character) of armchair graphene nanoribbons depends on the width of the structure hence the precursor.[12,14] Furthermore, the cavity size of 2D honeycomb structures can be increased simply by increasing the size of the molecules.[15] One has to point out that the choice of the appropriate molecular building block can lead to important applications as in electronic devices through extended π-conjugation in the networks.[16]

The aim of this thesis is to gain further fundamental knowledge about surface-mediated polymerization and coupling reactions, with focus on the interplay between the design of the molecule, the functional groups, and type of surface. Therefore, it is studied how the reaction parameters like temperature, reactivity vs. mobility of the precursors on the surface and bond type (covalent vs. organometallic / metal-organic in respect to stability) between the organic moieties affect the formation of low-dimensional nanostructures. A profound understanding of the influence of these factors is essential to develop synthesis protocols for structurally defined and extended polymers.

Section 2 describes the theoretical and experimental fundamentals for surface-mediated polymerization, while the role of the solid substrate is summarized in Section 2.1. Two established polymerization strategies are further explored in this thesis: (1) the surface-assisted Ullmann coupling (Sec. 2.2) and (2) the surface–mediated metal–organic coordination (Sec. 2.3). To follow up the adsorption of the molecules and initial structural formation together with continuous observation of the reaction pathway, surface-sensitive analysis techniques were applied and are summarized in Sec. 3. Scanning Tunneling Microscopy (STM) is applied for structural characterization of the reactant and the reaction products in real space with submolecular resolution (Sec. 3.1). Complementary to STM, X-ray Photoelectron Spectroscopy (XPS, Sec. 3.3) provides information about core level binding energies as probes for the chemical environment of specific elements. Further information of the electronic and geometrical structure of the adsorbates is yielded by Near Edge X-ray Absorption Fine Structure (NEXAFS, Sec. 3.4). These surface-sensitive analytical tools are

applied to study different exemplary cases of on-surface synthesis.

For the surface-assisted dehalogenative coupling, detailed studies of two precursors are presented:

(1) A doubly bromine and iodine functionalized pyrene derivative (Sec. 4) with the potential to form 2D conjugated and covalently interlinked nanostructures. Special emphasis is given on the anticipated steric hindrance due to covalent coupling between two pyrene backbones (1/1'-position) by repulsive interaction of hydrogen atoms, as well as the hierarchical polymerization through different temperature thresholds for dissociation of iodine and bromine. Additionally, the distinct surface influence of Ag(111) vs. Au(111) on the network formation is comparatively studied.

(2) The study of a brominated and fluorinated biphenyl precursor on Ag(111) is presented (Sec. 5), with focus on the initial site-selective 3,5'-didebromination and the underlying conformational mechanics. To unveil the influence of perfluorination, the fluorinated tecton is compared with its hydrogenated analogue, with respect to site-selective debromination and formation of 2D organometallic and covalent networks.

The third experimental case presents the study of a surface–confined metal-organic coordination of hexaaminotriphenylene on Cu(111) (Sec. 6). 2D networks of overall neutral hexaaminotriphenylene complex with Cu^{2+} centers prepared at the liquid / air interfaces were reported previously,[17] and showed an electrical conductivity by virtue of the extended π-d conjugation in the 2D sheets. Herein, the focus is given on manufacturing a 2D monolayer by surface-assisted polymerization of the precursor and intrinsic Cu atoms. In addition, the influence of extrinsic Ni atoms on deprotonation, metal-coordination and nanostructure formation is studied. The large asset of these studies at solid surfaces is the possibility of a precise structural characterization by STM and a pristine chemical characterization by in-situ XPS without risk of contamination.

Finally, the findings and results of this thesis are summarized, and the thesis concludes with an outlook on the next steps in on-surface synthesis (Sec. 7).

2 On-surface chemistry on solid surfaces

On-surface chemistry of molecules, acting as building blocks for bottom-up synthesis of ordered nanostructures, gives a great variety of combinations of possible interactions, depending on the surface, the functional groups as well as the tecton's chemical structure. Herein, the focus is on flat absorbed molecular building blocks and their synthesis into ordered structures. In the following, the most recent definition of a 2D polymer after Ref. 18 is used, described as ordered and strongly interlinked molecules, hence including metal-organic frameworks, while elsewhere a 2D polymer is exclusively described as covalently bound molecules.[19,20] It has been established to divide the surface-assisted chemistry of organic adsorbates into two topics: (1) the self-assembly of non-reacted molecular building blocks and (2) activated and interlinked tectons, for instance by bond scission of functional groups (bond dissociation energy is lower than for all other bonds in the molecular framework)[21] from the organic backbone. In this thesis, the surface-assisted Ullmann coupling and surface-confined metal-organic coordination are applied as polymerization strategies and are described, including the polymerization steps, differences, properties and bonding motifs of intramolecular and adsorbate – surface interactions. Both established polymerization strategies are summarized in Figure 2.1. A detailed description of further on-surface polymerization strategies and coupling reactions can be found in Ref. 22.

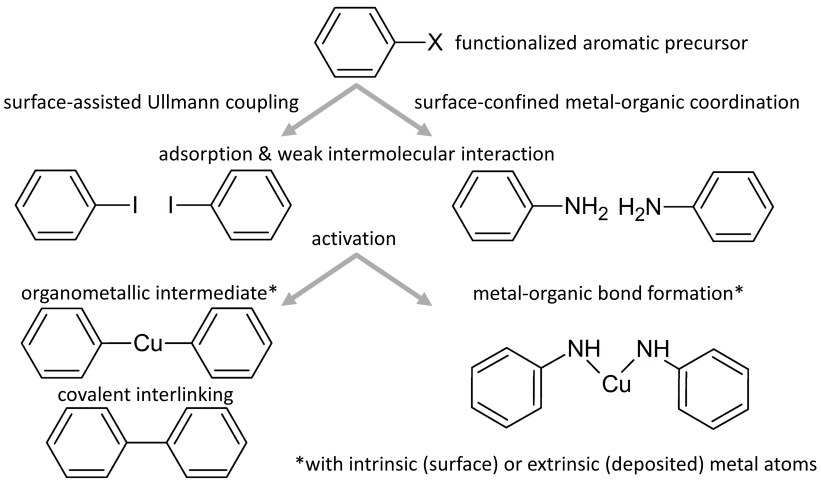

Figure 2.1: On-surface polymerization strategies used in the present thesis: surface-assisted Ullmann coupling by using halogenated aromatic precursors for a halogen cleavage and covalent aryl-aryl coupling (left) and a surface-confined metal-organic coordination by activation of functional heteroatoms at molecular building blocks and metal-organic bond formation (right).

2.1 Role of the metal surface

The basis of surface-confined polymerization is the adsorption of aromatic molecules on the surface, as well as a sufficient mobility on the substrate to drive ordered structure formation.[23] Finally, an induced and / or catalytic activation of the functional groups to form strong (covalent or metal-organic) bonds is necessary. For instance, temperature induced activation can lead to desorption or disintegration of the molecules before an extended network formation is achieved. The molecule – substrate interactions can be distinguished into a strong chemisorption (chemical bond formation upon adsorption) and a weaker physisorption, whereby the transitions between these are fluent. At a certain adsorbate-surface distance (∼3 Å), the adsorbate orbitals can be hybridized with the surface states, which generates either attractive or repulsive coupling.[24] Depending on the filling of bonding or antibonding adsorbate-metal d states and the spatial extension of the d states (which is described by the absolute magnitude of the coupling matrix element), Hammer and Nørskov explain, that the reactivity of coinage metals follows the order: Cu(3d) > Ag(4d) > Au(5d).[24] Furthermore, the metallic-surface can also directly interlink with the aromatic molecules by an organometallic (carbon - metal) or metal-organic (heteroatom - metal) bond formation, with adatoms or surface atoms. Intrinsic adatoms are mobile on the surface and are released from step-edges into the 2D adatom gas. Alternatively, surface atoms can be directly removed from the surface as identified by so-called etch-pits. The crystal structure is also able to act as template for pre-organization by a preferred adsorption-site and therefore influence the dimensionality of the nanostructures. For instance, 4,4'-dibromo-meta-terphenyl molecules form a 2D like structure on Cu(111), while on Cu(110) an organization of 1D chains could be observed.[25] A similar influence of the surface orientation was reported for 1,4-diaminonaphthalene: on Cu(111) / Cu(110) 1D structures were observed, however on Cu(100) a 0D structure was formed.[26] As mentioned above, to form extended networks the tecton mobility is necessary. The on-surface organization could be hindered through diffusion barriers and surface defects as well as the size of the molecule, i.e. larger molecules are more likely to be pinnend at the surface.[23] Another important factor for formation of extended networks is the competition between coupling and diffusion, e.g. on-surface coupling of a hexaiodo-cyclohexa-m-phenylene precursor showed a fractal-like structure on Cu(111) and more regular 2D networks on Ag(111). Additional Monte Carlo simulations confirm the crucial role of the ratio of diffusion and coupling and show a fractal structure for a high coupling affinity and low diffusion on Cu(111) and vice

versa for a more ordered 2D network on Ag(111).[27] The influence of the surface onto organic molecules works also in the opposite direction. For instance, the Au(111) surface reconstruction can be distorted in regions of the adsorbate by relieving stress due to incorporating metal atoms into the nanostructures.[28,29]

2.2 Surface-assisted Ullmann coupling

In chemistry the Ullmann reaction is defined as a covalent aryl-aryl coupling of aryl halide reactants by cleaving the halogens in a copper powder catalyst environment (cf. Fig. 2.1).[30] On metal substrates, a surface-assisted Ullmann type coupling was first presented by Rieder and coworkers, where every reaction step was controlled and monitored by STM. For iodobenzene at low temperature (20 K) on Cu(111), voltage pulses from the STM tip induced a I-C bond scission. The resulting aryl radicals were moved by lateral manipulation close to each other and voltage pulses from the STM tip induced covalent σ_{C-C} bond formation.[31] A further and the most prevalent activation method for on-surface Ullmann reaction is the temperature-induced halogen cleavage as first reported by Hecht and Grill and coworkers, using a bromophenyl functionalized porphyrine on Au(111).[32] The temperature-induced Br-C bond cleavage led to covalently interlinked polymers by aryl-aryl coupling. The dimension was controlled by the number of halogen sites, for instance mono-substituted building blocks formed dimers, whereas two bromines per precursor in para-position, led to 1D chain formation. Finally, four active sites resulted in a 2D covalent network.[32] During the last decade, the on-surface Ullmann polymerization has been established as a widely used polymerization strategy on metal substrates, due to a high reproducibility and less uncontrolled side reactions.[8] Generally, the surface-assisted Ullmann reaction starts with the deposition of a halogenated aromatic monomer on the surface. Mostly, the molecular structures are governed by halogen bonds, if the halogens are not yet split off (vide infra). Halogen bonds, also called X-bonds, arise due to an asymmetric charge distribution at the halogen, leading to a positive center (σ-hole) and an equatorial negatively charged belt.[33–35] The halogens can bond through the σ-hole to the negatively charged belt of another halogen atom of neighboring tectons. By the same token, partially charged hydrogen atoms of the aromatic building block enable a bond formation to the negatively charged belt of the halogen. Halogen bonds are highly directional and have a binding length, shorter then twice the van der Waals radii of the halogen. Experimentally observed binding strength are in the range of 2.4 - 36 kJ/mol.[23]

The second reaction step of surface-assisted Ullmann coupling is the activation by halogen cleavage from the organic backbone: The most common methods are temperature-induced by heating and initial bond scission by the reactivity of the surface. Other activation methods were experimentally demonstrated such as mentioned above by voltage pulses from the STM tip,[31] e-beam irradiation and UV-light (Br-C bond scission with λ_{UV} = 280 nm and 225 nm).[36] Whether an initial halogen-carbon bond scission already occurs after room temperature deposition, depends on the type of halogen and the surface reactivity for a similar molecule. The dissociation energy decreases with increasing atomic number of the halogen (I-C 280 kJ mol^{-1} < Br-C 351 kJ mol^{-1} < Cl-C 406 kJ mol^{-1} < F-C 532 kJ mol^{-1}). In this respect, activation of fluorine bound to carbon is rather unlikely without disintegration of the organic backbone (C-C 494 kJ mol^{-1}).[37–39] As described in Section 2.1, the reactivity of the coinage metal surface follows the order Cu > Ag > Au. This leads to an initial and full cleavage of iodine and a partly debromination on Ag(111) after room temperature deposition. Under equal conditions, the Br-C bond is intact on Au(111) and totally cleaved on Cu(111). This experimental observation is supported by DFT calculations of Björk,[40,41] where the activation energy (energy difference between transition state / intermediate state and reactant) for the dehalogenation reactions is lowest for Cu(111) and highest for Au(111) for bromo- and iodobenzene. For the same precursors the exothermic reaction energy (energy difference of reactant and product) behaves largest for Cu(111) and lowest for Au(111). Energy barriers are generally lower for iodine compared to bromine substituents. Iodine shows both, increased activation and reaction energies on all coinage surfaces. Furthermore, the influence of aromatic backbone on the halogen-carbon bond scission is seen by comparing surface-assisted Ullmann coupling of brominated tetrathienoanthracene[42] and 1,3-bis(p-bromophenyl)-5-(p-iodophenyl)benzene[43] on Ag(111). After room temperature deposition of both compounds, 83% of Br-C are initially cleaved for the anthracene derivate and only 38% for the benzene compound. The full Br-C bond scission is achieved by heating at 125 °C, and 260 °C, respectively. The halogen-carbon bond scission leads to a so-called surface stabilized radical, that can subsequently couple in two ways: (1) A directly covalent σ-bond between two aryl-aryl radicals, or (2) an interlinking with an adatom or surface atom by forming an organometallic structure (C-metal-C) as an intermediate step. Organometallic networks show an error correction process, i.e. "self-healing" of organometallic structures is induced by C-metal-C bond reversibility, resulting in highly ordered molecular arrangements.[43] Normally a

coupling between two tectons via one metal atom is observed, exceptions with coordination numbers up to three or four ligands per metal atom are rarely observed for non-ordered structures.[44]

On Ag(111) and Cu(111) surfaces, organometallic bonds are commonly present, whereas on Au(111) organometallic intermediates are unusual. C-Au bonds could be mainly identified, when direct covalent bond formation is hindered by steric repulsion between the molecular building blocks, as for instance in methylated-terphenyl,[45] pyrene[29] and heptacene derivatives.[46]

For the conversion of the organometallic intermediate into a covalently bonded structure an additional activation is necessary to overcome the energy barrier, for example by heating. For C-Au linkages a transfer into covalent bonds was reported after annealing at 300 °C.[47] For C-Au-C links between molecular building blocks with large steric hindrance further heating can lead to unordered and disintegrated structures. For instance, in a heptacene derivate stable C-Au bonds up to 260 °C were observed and additional annealing did not led to aryl-aryl coupling.[46] Direct covalent coupling on Au(111) is initiated by dehalogenation in a temperature range for bromine functionalized molecules at 175 °C,[48] while chlorine activation requires 300 °C.[49,50] However, on Ag(111) organometallic intermediates are converted at 170 °C into covalent interlinks.[43] Consequently, the transformation from C-Cu intermediate into a covalent C-C bond requires the lowest activation temperature (160 °C) due to the highest surface reactivity of the coinage metals.[50]

In general, on-surface synthesis is a thermodynamically driven process where the reactants and products aspire to reach the free energy minimum.[41] Under some circumstances the reaction product is trapped in less favorable intermediate structures.[41] This metastable case is kinetically trapped. Several effort was put into the external control of reaction steps and influence factors to study their influence on kinetics and thermodynamics. The focus is on steering and improving the formation and order of extended and defect-free covalently bonded nanostructures. By the same token, a large number of aromatic precursors which were functionalized by iodine, bromine and chlorine demonstrated versatile approaches to improve the network quality.[43,48–53] A promising approach was first demonstrated by Laffarentz and Grill, establishing a hierarchical polymerization by using different halogens with different temperature thresholds for C-halogen dissociation to connect the molecules step-by-step instead of single-step connection.[52] They used a porphyrine derivate with two bromine and two iodine functional groups in trans-position. Carefully applied heating steps induced

only I-C bond scission leading to 1D chains, whereas Br-C bonds remained intact. Subsequent heating triggered bromine dissociation, resulting in 2D covalent network formation with a domain size of 8 × 8 tectons. For another molecular building block this step-wise polymerization showed a successful on-surface synthesis of defect-free 2D networks with a size of 5 × 5 nm.[53] Moreover, the organometallic intermediate state and the related high preorder of the tectons on Ag(111), led to structurally perfect 2D covalent networks of 15 × 15 nm.[43] In addition, different reaction parameters such as deposition and annealing rate, as well as a surface temperature (RT, 185 °C, 250 °C and 375 °C) during deposition were studied as a possibility to improve the network quality. It was recognized that a lower surface temperature reduces irregular pore formation.[48] Surface-assisted Ullmann coupling is also used to synthesize atomically precise graphene nanoribbons by covalent coupling of 10, 10'-dibromo-9, 9'-bianthryl monomers into 1D polyanthrylene chains before their cyclodehydrogenation, i.e. surface-assisted intra- and / or intermolecular C-H cleavage and covalent C-C interlinking resulting in a sub-unit of graphene.[12,54] A further example of on-surface Ullmann coupling as basis for a further reaction was reported for porous carbon nanoribbons by dehalogenative and dehydrogenative polymerization of prochiral 1,3,5-tris(3-bromophenyl)benzene.[55] Additionally, graphene films can be grown at low-temperature (∼570 °C) by on-surface Ullmann coupling of a hexabromobenzene monomer on Cu(111).[56] Ullmann-type coupling could also be observed for a dehalogenative homocoupling of alkynyl bromides.[57] First steps to use covalent coupling via dehalogenation for applications, like electronic devices, were carried out on metal supported boron nitride,[58,59] graphene,[59] and bulk insulator (calcite, $CaCO_3$).[60] Likewise, a post-synthetic decoupling of covalent networks by iodine intercalation was reported.[61,62]

2.3 Surface–confined metal–organic coordination

Metal-organic coordination reaction is a well established polymerization strategy in complex chemistry. Metal-organic frameworks are reticular networks consisting of metal-ions bound to organic (ionic) molecules, so-called ligands. The metal-organic structures can be polymerized in solution, where they form 3D frameworks or crystalline 3D structures consisting of stacked 2D layers. By the same token, metal-organic coordination was also demonstrated for monolayer thick polymers on a metal surface under UHV conditions.[18] Contrary to the organometallic bond formation in surface-assisted Ullmann coupling, the functional group of the aromatic molecule is

directly involved in the metal-organic bond formation and interlinks the ligand and the metal-ion by electron donor-acceptor interactions possibly with partial covalent character.[63] Suitable functional groups are based on heteroatoms, and are usually nitrogen-, sulfur-, and oxygen-groups.[9] The reaction pathway is shown in Figure 2.1 and bears similarities to surface-assisted Ullmann coupling. The molecular building block is deposited on a crystalline metal surface and self-assembles by hydrogen bonds into extended and defect-free structures. The polymerization of amino,[64,65] thiol,[66–68] carboxyl[69] and hydroxyl[70] functional groups is thermally and / or catalytically activated by means of deprotonation, as requirement for metal-organic coordination. In contrast, heteroatoms like nitrogen in pyridine[71] or nitrile[72] groups can already bond to the metal-ion via their lone pair electron, even at low temperatures. Consequently, the onset of organometallic network formation could already be observed at 180 K.[73] On crystalline Au and Ag surfaces, the formation of metal-organic networks by intrinsic metal atoms is rarely observed[74] and usually more reactive extrinsic adatoms, like Fe,[70] Co,[15] Ni,[75] and Cu[76] are deposited as additional catalysts and coordination centers.

Contrary to the organometallic intermediate state during Ullmann coupling, where a linear C-metal-C bond formation is commonly observed, surface-confined metal-organic structures show a vast variety of coordination motifs.[9] Even molecular building blocks with two functional groups in para-position, can lead to three- and fourfold coordination networks on surfaces.[15,69,70] The formation of surface-confined metal-organic coordination networks is influenced by following points:

(1) An important factor is the coordination motif of the metal-ion with the ligand as described by the coordination number (number of ligands binding to one metal center). Thus, the oxidation state and thereby the electron configuration of the metal centers have a strong influence on the topology of the metal-organic structures. A general description of the metal-organic bond formation is given by the ligand-field theory.[63] The organic ligands are described as a negative point charge and induce a repulsive interaction with the d-electrons of the metal center. Consequently, the degeneracy of the energy levels is lifted and the energy of the d-orbitals change. Depending on the ligand-field splitting energy and compared to the spin pairing energy, two configurations of the electrons in the d-orbitals (d4 - d7) are possible: A high spin (maximum number of unpaired electrons) or a low spin (minimum number of unpaired electrons) electron configuration. The low spin electron configuration for example is realized, if the ligand-field splitting energy surpasses the spin pairing en-

ergy. As a consequence, in the low spin electron configuration, the d_{z^2} orbital energy is decreased under the niveau of the $d_{xy,xz,yz}$ orbitals, and therefore the complex is stabilized in a square planar form. For instance, for Ni($3d^8$) metal-organic nanostructures in Ni(II) oxidation state, the ligand-field splitting energy is high enough to stabilize a square planar coordination.[63] The situation for Cu ($3d^9$) atoms in a Cu(II) oxidation state is different: the ligand field splitting energy cannot overcome the spin pairing energy, hence the system cannot reach a low-spin electron configuration, and a non-planar tetrahedral coordination is preferred. (2) The size of the coordinating metal-ion is important, for instance a coordination number up to six for rare earth metal like europium was reported in Ref. 77. (3) Steric hindrance can play a role due to the size and the shape of the ligand. A 2D network formation of 1,1':4',1"-terphenyl-4,4"-dicarbonitrile precursors was reported,[15] while 1,4-bis(4-pyridyl)benzene show 1D chain formation.[78] The ligand-field theory bears several limitations for surface-mediated metal-organic coordination, which are additional and important factors for molecular architectures and are described in the following: (4) The postulated charge transfer from the ligand to the coordination center to achieve an overall charge neutrality of the metal-organic structure is controversially discussed through the "infinite" electron reservoir of the surface. For instance, charged metal centers where reported for vanadium and platinum metal-organic structures.[79,80] Furthermore, on-surface synthesis of 2D reticular structures with more then one metal per coordination center are possible, for instance by a Cu_3 coordination.[68,81] (5) The metal substrate is a decisive factor by a direct bond formation with intrinsic adatoms. (6) A further important aspect is the surface mobility and reactivity as described in Chapter 2.1.

The thermodynamical stability of metal-organic compounds can be raised due to a denticity >1 and the molecules can form a so-called chelate complex. The denticity describes the number of donors per binding site of the ligand which bind to the metal center. The highest stability is achieved during five (...-C-heteroatom-Me-heteroatom-C-...) and six-fold (...-C=C-heteroatom-Me-heteroatom-C-...) chelate rings and is further increased by the total number of chelate rings.[63] For a given metal center, coordinated by the same number of donors, the chelate effect leads to increased entropy and decreased enthalpy. As a consequence the free energy minimum is increased by a reduced repulsive ligand-ligand interaction.[63] Accordingly, surface-confined metal-organic structures that show the chelate effect, exhibit a high temperature stability up to 300 °C,[64] whereas for non-chelating 2D networks a disin-

tegration of the metal-organic bond formation was already reported at RT.[68] Table 2.1 compares the bond energies of the described different types of intermolecular bonds discussed in this chapter.

interaction	bond strength (kJ/mol)	bond strength (eV)
H-bond	1-16	0.05-0.7
Halogen-bond	2.4-36	0.1-1.5
metal complexation	11.5-70	0.5-3
covalent	23-100	1-4

Table 2.1: Bond strengths of molecular interactions, adapted from Ref. 23.

3 Surface-sensitive analysis techniques

The theoretical basis, measurement principles, and the experimental setups of the surface-sensitive analysis methods, used in this thesis, are described in the following chapter. Structural characterization of the surface-assisted polymerization of organic adsorbates is achieved by Scanning Tunneling Microscopy (STM) as a standard tool. STM enables a direct imaging of surfaces and adsorbates with (sub)molecular resolution in lateral direction and sub Å in height (Sec. 3.1). Furthermore, two X–ray based spectroscopic methods, X–ray Photoelectron Spectroscopy (XPS, Sec. 3.3) and Near Edge X–ray Absorption Fine Structure (NEXAFS, Sec. 3.4), are used to complement STM experiments and provide additional information about chemical and structural properties. In addition, chemical changes during the surface assisted polymerization can be monitored. The combination of STM and spectroscopic methods is quite powerful and leads to detailed insights into the on-surface polymerization of molecular building blocks on crystalline surfaces. Table 3.1 resumes the advantage and disadvantage of the applied surface sensitive techniques and exemplifies their complementary.

	STM	X–ray spectroscopy
Spatial resolution	sub-Å ●	● beam diameter up to 1 mm
Energy resolution	sub-meV ●	●∼0.02 eV
Elemental sensitivity	unspecific ●	● element specific
Conformation determination	Convoluted in ● electronic structure	● via moiety orientations
Sensitivity of architecture defects	High ●	● Limited
Damage potential	Low ●	● High
Structural diversity	Resolved ●	● Averaged out

Table 3.1: Comparison of STM and X–ray spectroscopy and the excellent complement of these surface-sensitive analysis tools (color scheme: green, advantage; red, disadvantage; black, medium) adapted from Ref. 82.

3.1 Scanning Tunneling Microscopy

The development of the STM by Binnig and Rohrer and coworkers in 1982 enables the first real space imaging of a (semi-)conducting surface with atomic resolution.[83]

In contrast to diffraction methods, as Low Energy Electron Diffraction (LEED), the magnificent advantage of STM is the local real space imaging, instead of an averaging over a "large" area of the surface by an incident beam ($\varnothing_{e-beam} \sim$1 mm).[84] STM yields information on adsorption-sites, unit cells, distribution of atoms / molecules within the unit cell, as well as phase boundaries of adsorbate structures.[85] The physical basis of STM is the quantum mechanical tunneling effect. If a conducting tip is close enough to a (semi-)conducting surface ($<$ 1 nm) and a voltage (U_T) is applied between tip and surface, electrons can tunnel through the potential barrier and a net current (I_T) can be measured. Derived and simplified from 1D tunneling theory[86] for an electron tunneling through a 1D vacuum barrier, from an occupied into an unoccupied state, the relation between I_T and changes of the tip–surface distance (barrier width) Δz ($\Delta z = z - z_0$), is given by:[85]

$$I_T(\Delta z) \sim I_T(z_0) e^{(-2\alpha\Delta z)} \tag{3.1}$$

where the decay constant α is given by m_e, the mass of the free electron and the height of the barrier Φ (averaged tip- and surface work functions Φ_{work}):

$$\alpha = \sqrt{2m_e\Phi}/\hbar \tag{3.2}$$

It becomes apparent that a small change in Δz of 0.1 nm towards the surface increases I_T by an order of magnitude.[85,87] Consequently, this explains the high surface sensitivity, and the reason why atomic resolution in vertical direction is achieved. In a STM image differences in apparent height do not exclusively originate in geometric heights. Even more, Tersoff and Hamann describe the theory of the tunneling current in STM by the transition probability of an electron from an occupied into an unoccupied electronic state. Hence, I_T is determined by the overlap of wave functions of tip and substrate and this can lead to an altered measured height due to electronic effects.[88] Figure 3.1 illustrates the tunneling effect with a negative bias applied to the sample, resulting in a tunneling of electrons through a 1D vacuum barrier from the tip to the sample or vice versa for a positive bias.

The main part of a STM is the so-called scan-unit, where the tip is mounted on a piezoelectric tube. The movement of the piezoelectric tube is proportional to the applied voltage and is in a range of ($\sim$1 - 10) nm V^{-1}.[85,89] The electrodes (x-, y-, z-direction) of the scan-unit are actuated by computer control, whereby the control voltage is amplified into a range up to 200 V. All STM images in the present thesis

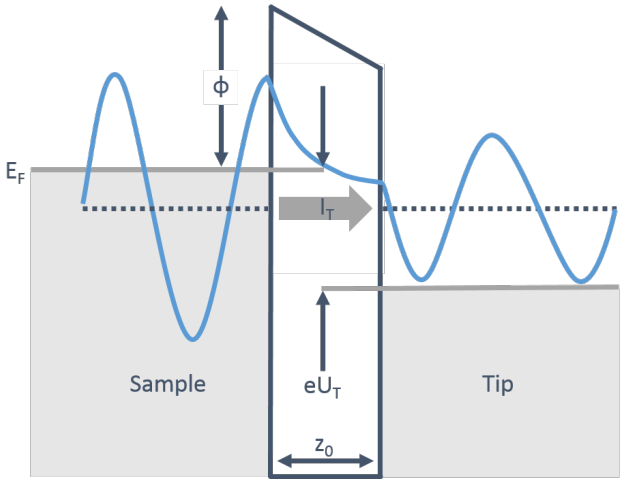

Figure 3.1: Basic principle of the tunneling effect through a potential barrier (width z_0 and height Φ) between two electrodes with applied tunneling voltage U_T (sample negative), adapted from Ref. 87.

are recorded in the so-called constant current mode, where I_T is held constant by a feedback loop, while the resulting changes in height by altering of $U(\Delta z)$ are recorded. An image consists of 512 × 512 pixels and is acquired by a meandering like x- and y- scan of the surface. The schematic working principle and components of a STM are depicted in Figure 3.2.

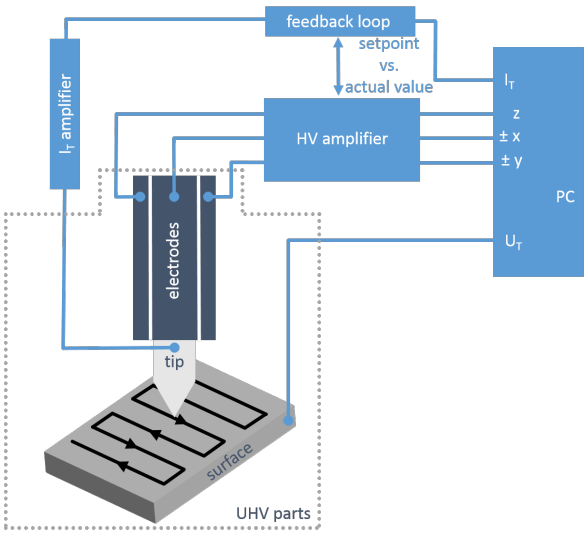

Figure 3.2: Schematic principle of a STM setup, adapted from Ref. 85.

The (sub)molecular resolution in lateral direction, as well as the sub Å sensitivity in height of a STM, makes it to an ideal tool for the structural characterization of molecular and atomic adsorbates. Especially, for monitoring of the surface-assisted polymerization: Less ordered structures and networks can be clearly imaged by STM, while diffractive methods only resolve highly ordered phases. In favorable cases, the use of STM enables a clear distinction between intact and reacted molecular building blocks. For instance, bright iodine atoms bound to fainter appearing organic backbones (cf. Sec. 4), and partly reacted molecules can be depicted by STM. It is also possible to distinguish further reaction products by STM, like organometallic / metal-organic and covalent polymers due to their different bond lengths of ∼0.3 nm (cf. Sec. 5 and Sec. 6).[43]

Experimental setup

All STM experiments described in this thesis were carried out in the same UHV setup working at a base pressure of 3×10^{-10} mbar after bake out. Tips and samples can be exchanged via a load lock, respectively. Additionally, the load lock is equipped with a resistive heater and an Argon leakage valve, for preparation in noble gas atmospheres. The main chamber is equipped with a home-built STM[89] and a spot profile analysis LEED. Single crystals were prepared by 0.5 - 1 keV Ar^+-ion sputtering and annealing at 500 °C. Tungsten tips were electrochemically etched in 2 M KOH solution. Furthermore, thin oxide layers on the tips can be removed by tip sputtering directly in the STM. Used tips are sharpened by applying a self-protecting voltage of +150 V on the tip while the tip is bombarded by Ar^+-ions with an energy of 1.5 keV .[90] For organic molecular beam epitaxy a home-built Knudsen cell with a high reliability and reproducibility for deposition rates was used.[91] The UHV chamber features various possibilities to mount molecular or metal evaporators, respectively. The UHV system is pumped by a Pfeiffer turbomolecular pump (magnetic bearing) with Pfeiffer HiCube 80 as forepump together with an ion getter pump and titanium sublimation pump. The STM is embedded into a vibration isolation, which acts as high-pass to avoid a mechanical coupling of low frequency (e.g. rotational speed of the turbomolecular pump or noise as building vibrations).

3.2 Surface-sensitive X-ray Spectroscopy

The surface sensitivity of X-ray spectroscopy that rely on the detection of electrons is given by the information depth λ (i.e. the inelastic mean free path of the electron) of the photoelectron, secondary electron, or Auger electron response.[92] Figure 3.3 shows the "universal" curve of λ depending on the kinetic electron energy after Seah et al..[92] The minimum of λ (= 0.1 - 3 nm) is located at an kinetic energy range of 10 - 200 eV.

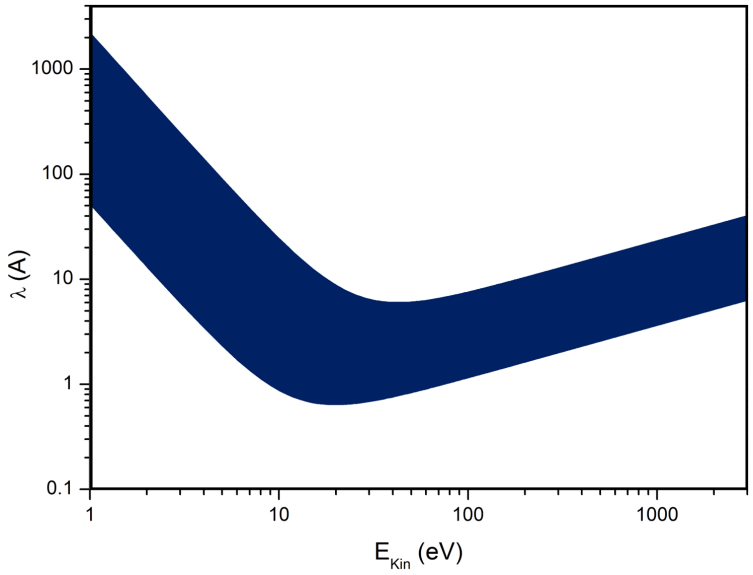

Figure 3.3: Inelastic mean free path, corresponding to the information depth λ of excited electrons as a function of the kinetic energy, after Ref. 92.

XP and NEXAFS spectroscopy are based on the absorption processes of an incident photon with an energy hv by a core electron with an initial energy E_i and an excitation of the core electron to a final energy E_f.

For XPS, excitation leads to an ejection of the excited core electron above the vacuum level. The kinetic energy of emitted electrons provides information of the core-level binding energy. In NEXAFS spectroscopy the excitation energy is varied, beginning a few eV before and around 50 eV after the absorption edge to gain information about unoccupied molecular orbitals by detection of electrons originated by secondary relaxation processes. The schematic adsorption and excitation processes to E_f for XPS and NEXAFS are shown in Figure 3.4.

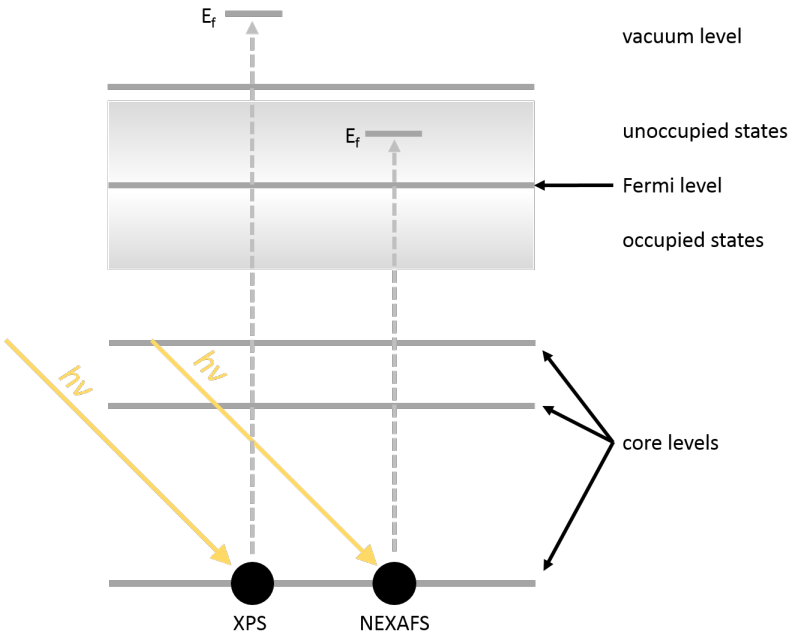

Figure 3.4: Scheme of the absorption processes of X-ray photons by a core electron. XP spectroscopy provides the binding energy E_B of the probed core-level through excitation of the electron above the vacuum level. However, NEXAFS uses a resonant excitation of core electrons to yield information about unoccupied molecular orbitals by secondary relaxation processes. Image is adapted from Ref. 93.

3.3 X-Ray Photoelectron Spectroscopy

XPS is based on the external photoelectric effect, where incident light with an energy hv higher then the sum of binding energy E_B of electrons and the work function ϕ_{work} of the solid, leads to an emission of electrons from the solid state.[94,95] Historically, the fundamental work of Manne and Kai Siegbahn was essential for the development of high resolution electron spectrometers for XPS experiments.[96] XP spectroscopy focuses on core level electrons yielding information about the binding energy. Figure 3.5 shows the excitation process of a core level electron from an initial state E_i by an incident X-ray photon with the energy hv. The photon is absorbed and the core electron is excited to its final energy E_f. The energy of the incident X-ray photon leads to an excitation of a core electron above the vacuum level ($E_f > E_{vacuum}$). The remaining energy corresponds to the kinetic energy E_{Kin} of the electron, which is measured in the experiment.

Equation 3.3 shows the relation between hv and E_B, depending on the surface work function ϕ_S and is only valid if relaxation processes are neglected (Koopman's theorem):

$$E_B = hv - E_{Kin} - \phi_S \tag{3.3}$$

Including the analyzer work function ϕ_A, the surface work function ϕ_S is canceled by equalizing the Fermi energies of the surface and the analyzer via an electrical connection. After energy calibration with a reference sample (clean metal substrate), the kinetic energy offset caused by ϕ_A is to set as zero. Consequently, the binding energy E_B of the core electron can be calculated with known excitation energy hv and measured E_{Kin}.[97]

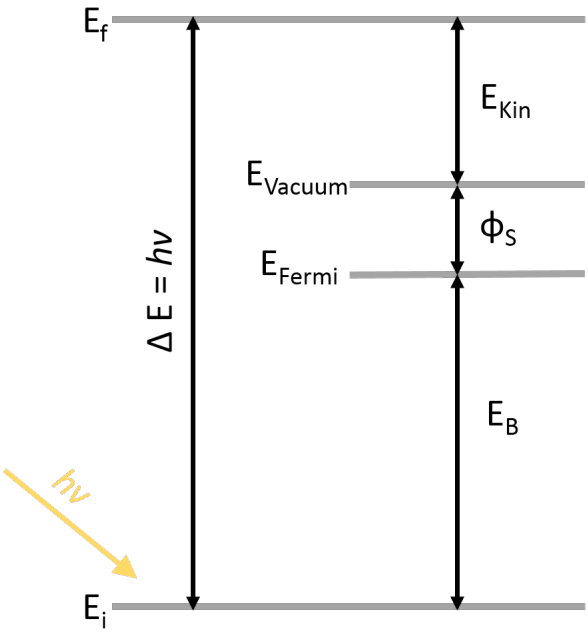

Figure 3.5: Scheme of the photoionization in a XP spectroscopy experiment: The diagram shows the excitation of a core level electron by a X-ray photon above the vacuum level with a resulting kinetic energy E_{Kin} of the electron. The binding energy E_B is determined by measuring E_{Kin} of the probed electron, as probe for the chemical environment of the core level, adapted from Ref. 93.

The resulting core hole is refilled by electrons of higher energy levels, whereby Auger electrons (multi-particle process) or X–ray fluorescence is emitted. The determination of the kinetic energy of the photoelectrons is commonly carried out by a concentric hemispherical analyzer (CHA). Initially, photoelectrons are focused in

a tube assembly and decelerated by a retarding electrical field to the pass energy, i.e. only electrons with a pass energy (typical range 20 - 100 eV) can pass into the CHA. Furthermore, only electrons with the chosen E_{Kin} can reach the detector along a predetermined path. A spectrum is recorded at a constant pass energy by incrementally increasing the retarding electrical field from low to high E_{Kin}. Figure 3.6 shows an exemplary XP spectrum of a clean Ag(111) surface. The spectrum shows sharp photoelectron lines, corresponding to Ag 3p, 3d, 4s and 4p core electron levels. Furthermore, Auger electrons (MNN) and valence band (VB) electrons are present. The FWHM of the peaks is proportional to the reciprocal lifetime of the core hole state according to the uncertainty principle. Commonly, a line width in the range of (0.4 - 1.2) eV can be achieved, corresponding to core hole lifetimes between (10^{-15} - 10^{-14}) s.[97]

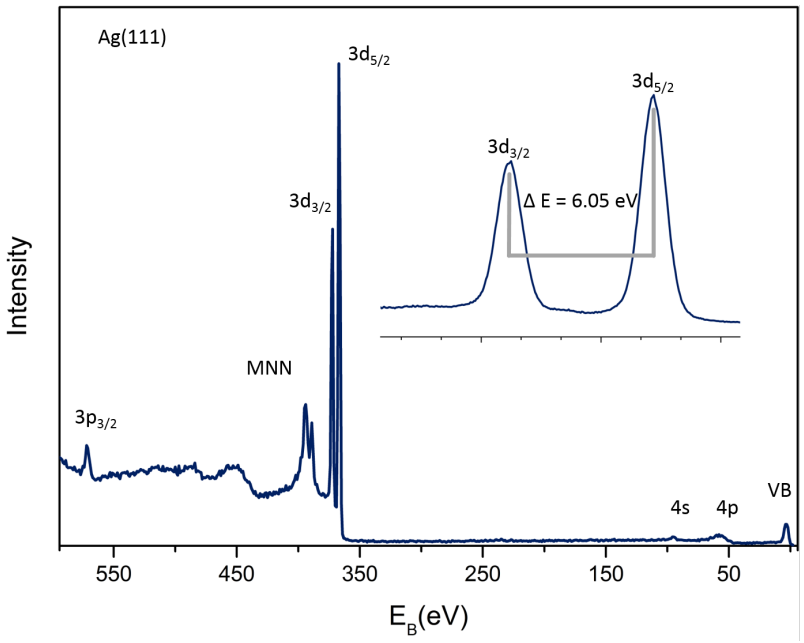

Figure 3.6: Survey XP spectrum of a clean Ag(111) surface. The inset shows the characteristic spin-orbit doublet of Ag $3d_{3/2}$ and $3d_{5/2}$ with an energy separation of 6.05 eV. The spectrum was recorded at HE-SGM beamline at BESSY II, with an excitation energy of 700 eV and a pass energy of 100 eV.

The inset in Fig. 3.6 shows the characteristic spin-orbit splitting into two components with a total angular momentum of $j = l \pm \frac{1}{2}$, as observed for orbital angular momentums $l > 0$. Consequently, the total angular momentum leads to different energy levels, and results in a characteristic doublet. Table 3.2 summarizes orbital quantum numbers, the resulting angular momentum, and the characteristic intensity

Orbital	Orbital quantum number	$j = l \pm \frac{1}{2}$	Intensity ratio $= \frac{2j_- + 1}{2j_+ + 1}$
s	0	$\frac{1}{2}$	-
p	1	$\frac{1}{2}, \frac{3}{2}$	1:2
d	2	$\frac{3}{2}, \frac{5}{2}$	2:3
f	3	$\frac{5}{2}, \frac{7}{2}$	3:4

Table 3.2: Spin-orbit splitting and characteristic intensity ratios of the resulting doublet.

ratio of the spin-orbit doublets as given by the multiplicity.[85,97]

The E_B of core electrons is primarily determined by the element, but further influenced by the local chemical environment.[85,93,97] The type of bond (hydrogen bonding, organometallic or covalent), bonding order (single vs. double bonds) and the binding partners itself (e.g. carbon bound to functional groups vs. carbon in the aromatic backbone), lead to alterations in E_B which is referred to as chemical shift. To estimate the strength of chemical shifts the difference of electronegativity of the binding partners is a helpful indicator. For example, the C-F bond leads to a higher E_B for C 1s (∼2.5 eV cf. Sec. 5.3). Fluorine, as the most electronegative element, attracts the shared electron pair towards itself and the effective charge of carbon becomes positive and consequently E_B of C 1s increases.[97] Following the Pauling scale, halogens bound to organic molecular building blocks lead to a strong chemical shift of the corresponding C 1s core level to higher E_B, while organometallic compounds are shifted to lower E_B ($E_B : C-F > C-Br > C-I > C-C < C-Ag$). The experimental limit for the detection of chemical shifts, is the energy resolution of the CHA with 0.1 eV.[98] For instance, a comparatively low chemical shift between C-C and C-H, as well as C-C and C-Au can not be resolved.[40,98] Chemical shifts to lower E_B are also induced by a reduced coverage from multi- to (sub)monolayer coverage due to core-hole screening by the surface.[99,100] Moreover, co-adsorbed reaction products, e.g. cleaved and chemisorbed halogens can induce an increased work function, resulting in a lowered E_B.[29,101] In addition to a qualitative measurement of the composition of the surface and the adsorbates, XP spectroscopy enables a quantitative analysis, hence a monitoring of the progression of a surface reaction. The simplest

way to extract absolute changes in the composition by a surface-assisted polymerization from a known functionalized aromatic precursor, is the comparison of intensities of a specific XP line per element after deposition and activation steps. For instance, a partly dehalogenative coupling reaction of a molecular building block is reflected by a chemical shift of the cleaved and chemisorbed halogen and in a reduced intensity of the pristine halogen-bound carbon. Consequently, in the C 1s spectrum the absolute halogen cleavage from the tecton is equally shown by the reduced carbon-halogen intensity. However, the intensity in C 1s of C-C by covalent coupling or newly formed self-assembled organometallic intermediates (C-metal) becomes increased by the "lost" carbon-halogen intensity. Thereby, it is possible to quantitatively monitor the polymerization progress of an intact or partially reacted organic building block to organometallic / metal-organic intermediates and finally to covalent polymers.[97] It has to be noted, that this comparative approach is only useful, if the experimental conditions are identical (photon flux, excitation energy, excitation and emission angle and analyzer settings).

Experimental setup and data analysis

All XP spectra shown in this thesis were carried out in two different facilities with two different experimental approaches, either synchrotron based, at the high-energy-spherical-grating-monochromator (HE-SGM) beamline at BESSY II Berlin, or at a SPECS UHV system equipped with a laboratory X-ray source. For photoelectron spectroscopy, the HE-SGM endstation is equipped with a Scienta R3000 CHA analyzer, for further details of the experimental setup of the HE-SGM beamline the reader is referred to Sec. 3.4. The SPECS UHV system is provided by the cluster of excellence Nanosystems Initiative Munich, and consists of a load lock, a preparation- and an analysis chamber. Preparation- and analysis chamber work at a base pressure of 3×10^{-10} mbar. The preparation chamber is equipped for single crystal preparation as described in Sec. 3.1. The analysis chamber is equipped with a monochromated Kα Mg/Al X-ray source (XR50M) with excitation energies of 1253.5 / 1486.3 eV and a filament heat power of 350 W. A CHA (Phoibus 150) is used for E_{Kin} selective photoelectron detection, where passed photoelectrons are amplified by a multi-channel plate and detected. Raw data was normalized by the number of sweeps and a linear background was subtracted. The peaks were fitted by a combination (Voigt function) of Lorentzian function of the intrinsic line shape of the photoemission process and Gaussian function to account for instrumental broadening.[97]

3.4 Near Edge X-ray Absorption Fine Structure

Complementary to STM and XPS, NEXAFS delivers additional structural and chemical insights of adsorbates and polymers on surfaces. Foremost, quantitative information of the adsorbate structure, i.e. the adsorption angle of functional units of molecules and the organic backbone itself with respect to the surface can be extracted. In addition, qualitative details of the chemical structure can be obtained. For instance, the presence of specific (single vs. multiple) bonds of inter- and intramolecular interlinks can be determined to proof the intactness of molecular building blocks during the on-surface synthesis.[102] NEXAFS probes core level electrons (mainly 1s) of a specific atom (low Z elements like C, N, O and F) by incident X-ray light and excites the electrons in unoccupied molecular orbitals (contrary to the ionization during XPS experiments).[102] Figure 3.7 shows the schematic excitation process lifting, a core electron into an unoccupied molecular orbital by an incident X-ray photon with an energy $h\nu$. The remaining core hole is refilled by electrons of higher energy levels resulting in an emission of Auger electrons or radiative by fluorescence. It has to be emphasized that the ejected electrons are proportional to the amount of created core holes and therefore to the absorption cross section (cf. vide infra), i.e. a strong absorption for incident X-ray photons leads to an increased number of ejected electrons.[98] A spectrum is recorded by incrementally increasing the incident photon energy and the simultaneous detection of the emitted secondary electrons. Currently, a synchrotron radiation source, where electrons are boosted and stored by moving on a circular path, is necessary for NEXAFS. Electrons in the storage ring are accelerated to an oscillatory path in an insertion device (wiggler or undulator) and emit X-ray radiation along a tangential path into the beamline.[93] This radiation is focused and the photon energy is selected by a monochromator of the beamline ((200 - 700) eV for the HE-SGM Beamline at BESSY II, cf. 3.4). The photon energy is varied between ∼10 eV before and ∼50 eV after the absorption edge. For instance, the C K-edge is located at 285 eV and NEXAFS spectra are recorded in a photon energy range between 275 - 330 eV.[103] For incident photon energies $<$290 eV for carbon spectra of aromatic molecules, the excitation of core electrons in usually π^* orbitals implies the presence of double or triple bonds, while the σ^* resonance ($>$290 eV) corresponds to single bonds. NEXAFS of polycyclic aromatic molecules lead to at least two C 1s $\longrightarrow \pi^*$ and C 1s $\longrightarrow \sigma^*$ transitions due to initial state effects. The reason are chemically shifted carbon atoms due to inequivalent position in the hydrocarbon molecule (e.g. Sec. 4.3).[102,104–106] Also final state effects, by

localization of the core hole at different positions within the molecule, can lead to additional resonances.[104–106] Even more, the composition of the adsorbate is mirrored in NEXAFS spectra. This allows to monitor the reaction pathway from intact organic molecules with functional groups (cf. Sec. 5), to surface-assisted polymerization into organometallic (cf. Sec. 4.4) or covalent structures.[64] The high chemical sensitivity of NEXAFS due to transition into unoccupied molecular orbitals even facilitates a distinction between C-C (C 1s $\longrightarrow \pi^*$) and C-H (C 1s$\longrightarrow \sigma^*$), which cannot be resolved by XPS.[98]

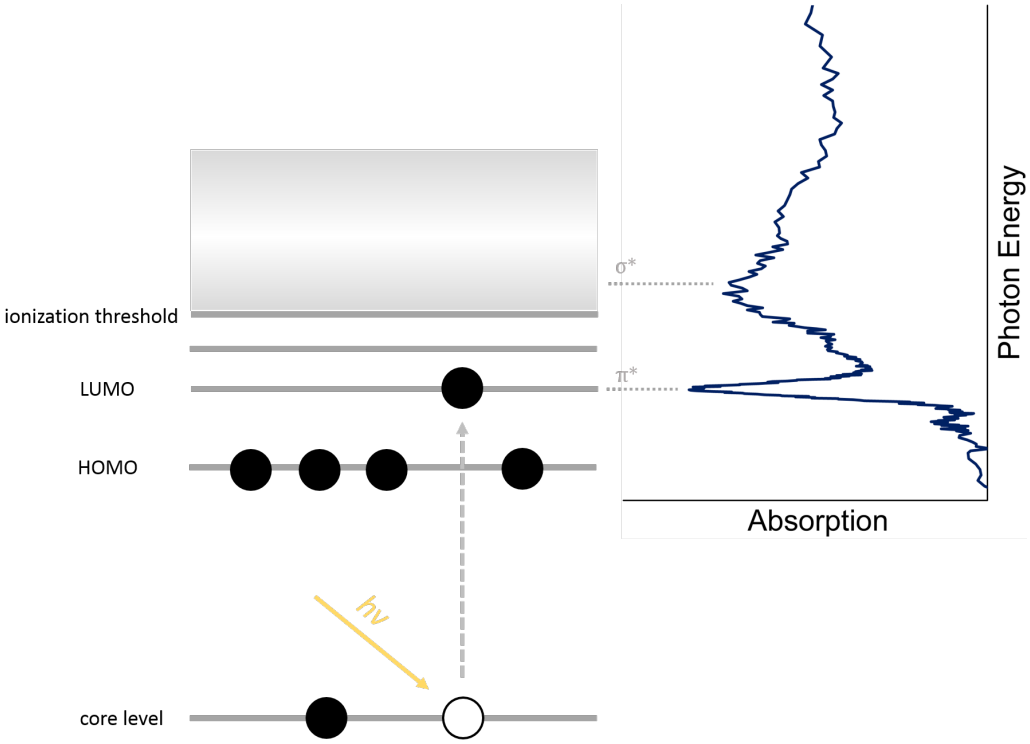

Figure 3.7: Scheme of the excitation of a core level electron into unoccupied molecular orbitals and an exemplary NEXAFS spectrum of benzenetrithiol molecules after heating to 270 °C on Cu(111) at an incident X-ray beam of 55°, unpublished data corresponding to Ref. 68, adapted from Ref. 93.

Extraction of the adsorption geometry

In addition to information about the chemical structure of the adsorbates, NEXAFS facilitates quantitative determination of the derived tilt angle α of adsorbates with respect to the surface, to complement STM gained structural data. In favorable cases, for the carbon K-edge it is even possible to determine specific bond angles of different

functional group with respect to the surface by chemically inequivalent carbon. For instance, bond angles of halogen-bound carbon (cf. Sec. 5.5) or C-metal-C intermediates (cf. Sec. 4.6) can be determined by an electronic transition into unoccupied orbitals of X-C or metal atoms, respectively. The foundation is:[98,102] (1) The spatial distribution of molecular orbitals depends on the chemical structure of the molecules and has a strong directional character. (2) The absorption cross section σ_x depends on the relative orientation between the X-ray electric field vector and the direction $\vec{T}$ of the transition dipole moment, for a dipole transition.[82] For linear polarized light, and a 1s initial state $|\Psi_{1s}\rangle$ and a final state $\langle\Psi_f|$, the transition intensity I is given by:

$$I \propto |e\langle\Psi_f|\vec{p}|\Psi_{1s}\rangle|^2 \propto |\vec{eT}|^2 \propto cos^2\delta \tag{3.4}$$

with $\vec{p}$ the dipole transition operator. δ is defined as the angle between the direction $\vec{e}$ of the electric field vector $\vec{E}$ of the X-ray and the direction of the transition dipole moment $\vec{T}$. Consequently, the intensity of a resonance reaches its maximum, when the electrical field vector is parallel to the axis of the direction of the final state orbital, and becomes zero when $\vec{E}$ is perpendicular to it.[98,102] According to Stöhr,[102] for a diatomic and triple bonded molecule, as a simplified model, where the σ^* orbital lies along the internuclear axis (z-axis) and the π^* orbitals are oriented along the x- and y- axis, for the intramolecular bonds it follows that intensities of σ^* and π^* resonances are proportional to $cos^2\theta$ and $sin^2\theta$, respectively of the angle θ between the incident X-ray beam and the surface. As a consequence, intensities of a σ^* and a π^* resonances behave in opposite ways, because $\vec{T}_{\sigma^*}$ of σ^* is perpendicular to $\vec{T}_{\pi^*}$ of π^*. This means that σ^* resonance becomes minimal when π^* resonance is maximal and vice versa. For detailed derivation the reader is referred to literature.[98,102] Figure 3.8 shows an exemplary angular dependence of NEXAFS intensities for σ^* and π^* resonances for covalently interlinked and flat benzene molecules. For adsorption parallel to the surface, out-of-plane C 1s $\longrightarrow \pi^*$ transition (Fig. 3.8, red) reaches an intensity maximum at a small incidence angle of 30°, whereas the resonance of the in-plane σ^* orbital shows a minimal intensity and vice versa for a normal X-ray incidence (Fig. 3.8, blue).

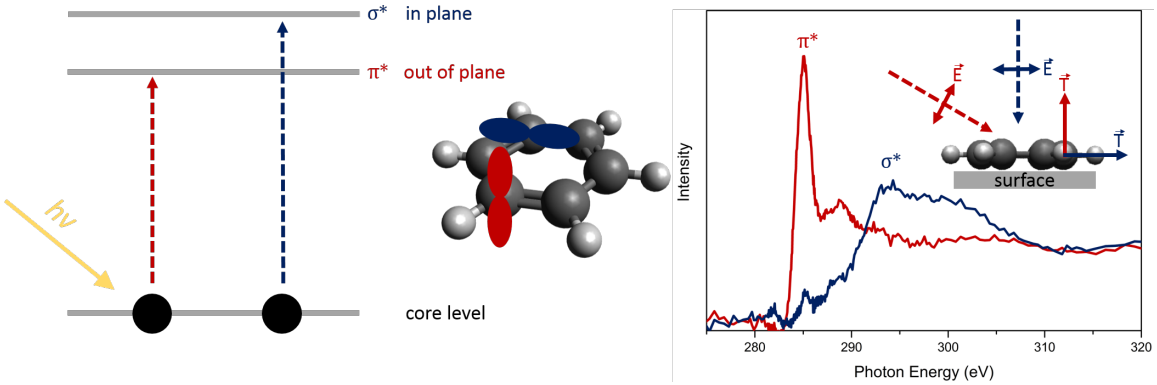

Figure 3.8: Scheme of the angular dependence of intensities of NEXAFS resonances between the directions of the transition dipole moment $\vec{T}$ and the electric field $\vec{E}$ of the incident X-ray beam: An excitation of a core level electron in an unoccupied π^* molecular orbital (out-of-plane of the bond axis), leads to maximum intensity (red) for an incidence X-ray beam angle of 30° to the surface orientation and vice versa for a normal X-ray beam for the in-plane σ^* molecular orbital (blue). Unpublished data, corresponding to Ref. 68.

The experimental basis for the extraction of the tilt angle between adsorbate and surface, is a highly ordered single crystal with low mosaicity. Furthermore, molecular building blocks at unusual adsorption-sites as step edges (even upright standing) can lead to experimental uncertainties (cf. Sec. 4.3). Also, upward or downward bent pendant groups (C-H, C-F) bound to carbon of the molecule can disturb the sp^2-carbon hybridization of the organic backbone by inter- and intramolecular steric repulsion and the arenes become partly sp^3 hybridized. This makes the interpretation of NEXAFS data more challenging and the simple model fails (cf. Sec. 5.3).

Experimental setup and data analysis

The NEXAFS spectra presented in this work were acquired at the HE-SGM beamline at BESSY II Berlin. The HE-SGM is a bending magnet beam line and features a photon energy range of 200 - 700 eV with linear polarization (degree of polarization 92%). The synchrotron itself is operated in top-up mode, i.e. a continuous refilling of electrons into the storage ring, and a ring current of 300 mA. Sample preparation by Ar^+ sputtering with energies of 0.5 - 1 keV and annealing, as well as the deposition of molecular building blocks were carried out in the preparation chamber. The NEXAFS spectra were acquired in the analysis chamber, equipped with a rotational manipulator. The secondary electrons are collected and amplified by a home-built

detector as described in literature.[102] A retarding voltage of -150 V was applied, to measure the partial electron yield (PEY) for a better signal-to-noise ratio.[98] The experiments were carried out on surfaces with (111) orientation where the azimuthal dependence is averaged out. For data analysis, the acquired raw data was photon energy corrected by using a clean highly oriented pyrolytic graphite as reference and averaged by the number of recorded spectra for all X-ray incident angles θ (30°, 45°, 55°, 70° and 90°). The next step was the normalization at a photon energy of 275 eV and subtraction of the likewise energy corrected spectrum of the clean substrate, to extract the adsorbate signal. An additional photon flux correction is necessary and was achieved by division with the spectrum of a clean Au(111) surface. Finally, the spectrum is normalized such that the intensity difference between the pre-edge at 275 eV and past-edge at 325 eV becomes one.[103,104,106]

4 On-surface polymerization of 1,6-dibromo-3,8-diiodopyrene – a comparative study on Au(111) vs. Ag(111) by STM, XPS, and NEXAFS

The present section shows the results of the dehalogenative on-surface reaction of 1,6-dibromo-3,8-diiodopyrene Au(111) vs. Ag(111), respectively. This section was published and reprinted with permission from: M. Lischka, M. Fritton, J. Eichhorn, V. S. Vyas, T. Strunskus, B. V. Lotsch, J. Björk, W. M. Heckl, and M. Lackinger: On-Surface Polymerization of 1,6-Dibromo-3,8-diiodopyrene – a Comparative Study on Au(111) vs. Ag(111) by STM, XPS, and NEXAFS, *J. Chem. Phys. C*, **2018**, 122, 5967–5977. Copyright 2018 American Chemical Society.

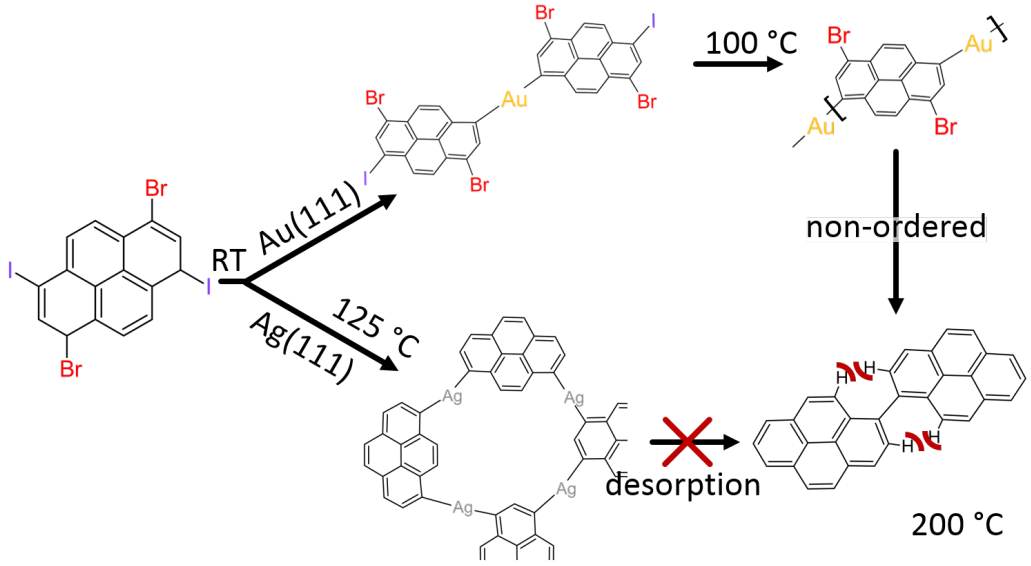

I performed all the experiments and the corresponding data analysis and interpretation, and prepared the manuscript under supervision of Prof. Lackinger. The co-authors M. Fritton, J. Eichhorn and Dr. T. Strunskus gave support during synchrotron measurements, while Dr. V. Vyas and Prof. Lotsch synthesized the precursor. Prof. Björk provided the DFT calculations.

4.1 Abstract

The surface chemistry of 1,6-dibromo-3,8-diiodopyrene (Br_2I_2Py) is comparatively studied on Au(111) vs. Ag(111) surfaces under ultra-high vacuum conditions by a combination of high resolution Scanning Tunneling Microscopy and X-ray spectroscopy. The chemical state of the molecular networks, i.e. the dehalogenation and the possible formation of organometallic intermediates, is assessed by X-ray photoelectron spectroscopy. In addition, pyrene tilt angles are quantified by carbon K-edge Near Edge X-ray Absorption Fine Structure experiments. Upon room temperature deposition of Br_2I_2Py onto Au(111) only partial deiodination was found, and Scanning Tunneling Microscopy revealed the coexistence of ordered arrangements of both intact Br_2I_2Py molecules and organometallic dimers as well as few larger aggregates. Further annealing to 100 °C triggered full deiodination followed by formation of organometallic chains of otherwise still brominated molecules. In contrast, on Ag(111) iodine is fully and bromine partly dissociated upon room temperature deposition of Br_2I_2Py. The initially disordered organometallic aggregates can be reorganized into more ordered structures by mild annealing at 125 °C. Yet, the conversion of the organometallic intermediates into well-defined cross-linked quasi 2D covalent networks was neither possible on Au(111) nor on Ag(111). This is attributed to the large steric hindrance in the covalently linked adsorbed state.

4.2 Introduction

During the last decade 2D covalent organic networks gained significant interest since the seminal works by the groups of Grill and Hecht as well as Porte.[32,107] These covalent nanostructures are relevant for a wide range of possible applications, in particular through their unmatched robustness and their unique and widely adjustable (opto-)electronic properties.[16,108,109] A common fabrication approach is on-surface synthesis: appropriately functionalized precursors or monomers are deposited onto solid surfaces, where their cross-linking is subsequently or simultaneously activated, in most cases by supply of thermal energy. Here the surfaces not only act as 2D templates, but can also have important chemical contributions for the activation of the reaction or for the stabilization of reaction intermediates, by-products, and products. Among the various utilized coupling reactions, surface-assisted Ullmann coupling is most abundant, because it is relatively reliable and less prone to uncontrolled side-reactions.[8] The underlying reaction scheme is straightforward: halogen-substituted

precursors are deposited onto in most cases metal surfaces. After adsorption the halogens are dissociated by virtue of the surface's reactivity in a thermally activated process. The respective dehalogenation barriers and temperatures primarily depend on the type of halogen and on the metal surface (material and crystallographic orientation).[110] For instance, on Cu surfaces bromine-substituents are readily dissociated at room temperature (RT), whereas further annealing up to 100 °C – 200 °C is required on Au surfaces. A further decisive influence of the precursor's chemical structure appears likely, but has not been systematically studied so far. Conveniently large differences in dehalogenation temperatures for different types of halogens facilitate temperature-controlled orthogonal Ullmann coupling. Sequential or hierarchical Ullmann coupling was demonstrated for bromine (Br) + iodine (I) functionalized precursors on Au(111), where the I-sites become activated directly after RT deposition or mild annealing (well below the debromination threshold), whereas the Br-sites were activated only after further annealing at higher temperatures.[48,52,53] An analogous temperature-programmed selective dissociation was reported for chlorine (Cl) + Br functionalized precursors on Au(111), yet with even higher activation temperatures for Cl dissociation.[49,50]

Dehalogenation generates so-called "surface-stabilized radicals" that can either couple directly to form covalent carbon-carbon (C-C) interlinks or form metastable organometallic aggregates based on C-metal-C interlinks.[111,112] These are routinely observed on Ag and Cu surfaces, but less common on Au surfaces. For aryl-aryl coupling further thermal annealing converts the organometallic into covalent linkages, presumably in a non-dissociative process.[43,113]

The on-surface synthesis of electronically conjugated, hence conductive 2D polymers is a long standing and rewarding goal,[109] also as the evolution of the electronic band structure with aggregate size is expected to be distinctly different from their 1D counterparts.[16] Therefore especially pyrene and its derivatives are promising candidates, also due to various possibilities for band gap engineering as previously demonstrated in solution.[114–116] Functionalized pyrene buildings blocks are also popular tectons in surface-supported supramolecular self-assembly.[117] Furthermore, a brominated pyrene precursor was proven suitable for the on-surface synthesis of armchair graphene nanoribbons with zig-zag facets.[118]

In this respect, halogenated pyrenes appear highly appropriate for the on-surface synthesis of fully reticulated 2D polymers. Yet the steric hindrance of 1-1' coupled pyrenes is significantly larger than for aryl-aryl coupling as already reported by Stöhr

et al. for 1,3,6,8-tetrabromopyrene (Br_4Py) on Au(111) and Cu(111).[29,119] Here, we propose sequential polymerization by taking advantage of the vast differences in deiodination vs. debromination temperatures as a viable strategy to overcome this steric hindrance. The Br_2I_2Py (cf. inset in Figure 4.1(a) for structure) precursor was designed to first interlink into extended 1D chains upon activation of the iodine sites. These chains could then in principle fuse into cross-linked 2D polymers upon subsequent activation of the bromine sites.[52] To further study the influence of organometallic intermediates that are routinely observed on more reactive surfaces,[42,43] additionally the polymerization of Br_2I_2Py was compared on Ag(111) vs. Au(111). Even though organometallic and covalent linkages can be safely distinguished in Scanning Tunneling Microscopy by the ∼0.25 nm difference in intermolecular bond lengths, chemical sensitivity is gained by complementary X-ray Photoelectron Spectroscopy experiments. Quantitative structural information is obtained from carbon K-edge Near Edge X-ray Absorption Fine Structure experiments that not only allow measuring average pyrene tilt angles, but also to further study unoccupied electronic states of the molecular networks.

4.3 Results on Au(111)

STM results on Au(111)

First, the results obtained on less reactive Au(111) surfaces are presented, where hierarchical polymerization was anticipated. After RT deposition two different types of ordered structures were observed by STM, an overview image is shown in Fig. 4.1(a). Both structures are comprised of fainter X-shaped features and clearly discernible pairs of bright protrusions, whose packing density varies between upper and lower structure. The lower structure appeared as intermingled stripe with well-defined boundaries. It consists of a dense packing of X-shaped entities with four terminal protrusions, whereby two diagonal protrusions appear significantly brighter. Owing to the perfect size match, the structural unit can unambiguously be assigned to intact (i.e. not dehalogenated) Br_2I_2Py precursors as also illustrated by the scaled overlay. The brighter contrast is characteristic for iodine-substituents,[52,120] hence by virtue of these chemical markers, STM not only verifies the molecular structure of Br_2I_2Py, but also reveals a similar orientation of all individual molecules in this densely packed structure. The close contact of the halogens indicates stabilization by halogen-halogen bonds as similarly found for Br_4Py onto Au(111),[29] but with an

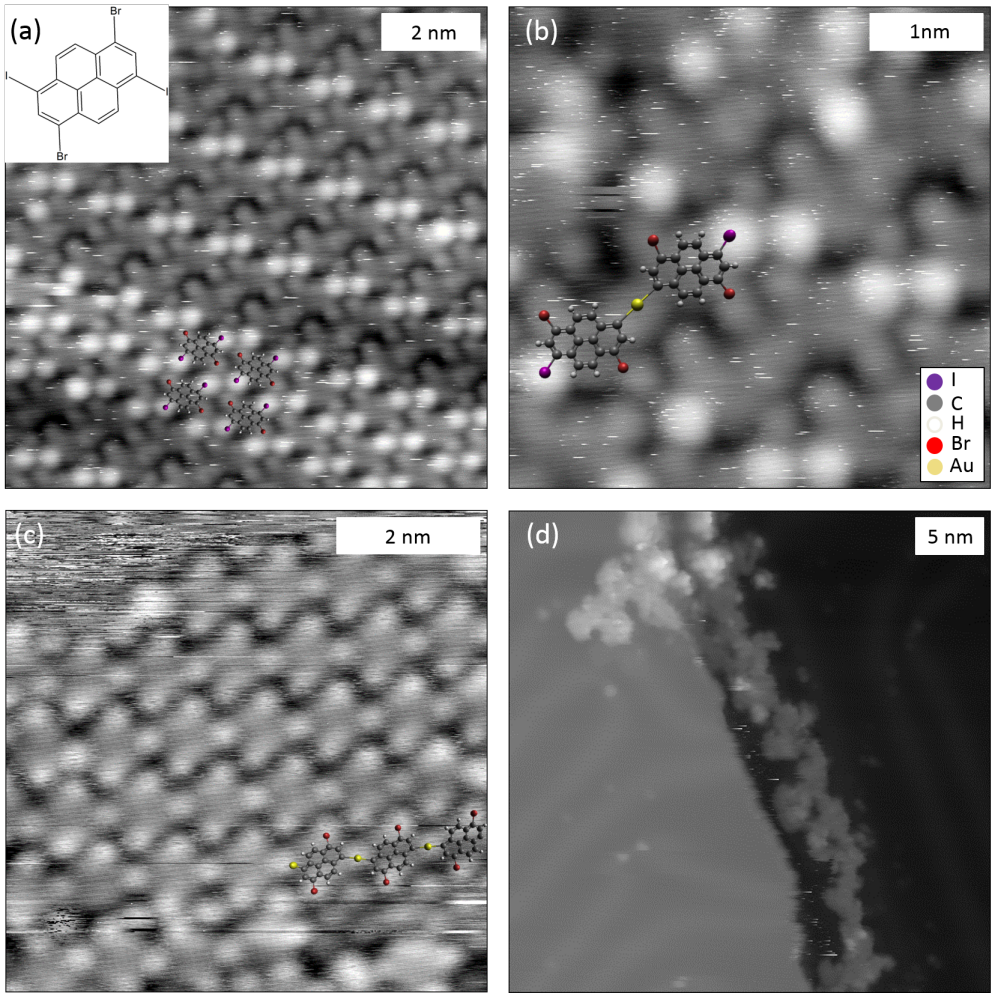

Figure 4.1: STM images of Br_2I_2Py on Au(111): (a) overview and (b) close-up acquired directly after RT deposition, and after annealing to (c) 100 °C and (d) 250 °C. The overlays show (a) intact molecules, (b) organometallic dimers with one C-Au-C linkage, and (c) organometallic chains formed after partial and full deiodination, respectively. (tunneling parameters: (a) 54 mV, 32 pA; (b) 54 mV, 31 pA; (c) 580 mV, 49 pA; (d) 940 mV, 48 pA)

unprecedented cyclic Br-I-Br-I arrangement that optimizes the electrostatic interactions of the iodine σ-holes with the equatorial belts of negative electrostatic potential of the bromine-substituents and vice versa.[33]

The structural unit of the upper ordered structure in Fig. 4.1(a) is a double X-motif again with two brighter protrusions along one diagonal. Evidently, this motif corresponds to two linked pyrenes. From previous studies of a singly iodinated triphenylbenzene derivative one could anticipate the direct formation of covalent linkages on Au(111) after deiodination.[48] According to structure simulations done with DFT, the center-to-center distance of 1-1'linked pyrene dimers in the gas phase amounts to 0.80 nm, whereby the steric hindrance results in a relatively large dihedral angle of $\sim$55° between the otherwise flat pyrene moieties (cf. Fig. A.6). Yet, the experimentally found center-to-center distance of (1.10 $\pm$ 0.10) nm is significantly larger, hinting towards organometallic C-Au-C linkages. This hypothesis is further supported by the perfect match of scaled overlays of DFT-optimized organometallic dimers with a simulated center-to-center distance of 1.02 nm (Figure 4.1(b)). The organometallic linkages were formed on previously iodinated sites. On the one hand this is expected from the absence of debromination on Au(111) at RT, on the other hand this is also consistent with the positions of the two remaining iodine-substituents. Organometallic intermediates on Au surfaces are less common, but are not unprecedented for comparably planar molecules.[47] Since the herringbone reconstruction is not observed anymore, the required Au atoms could originate from lifting the reconstruction, but might as well be supplied by the free adatom gas. In this respect, the fact that intact or only partly deiodinated monomers are observed upon RT deposition onto Au(111) appears more surprising. Even though in the literature full deiodination is described,[48] other groups report full deiodination only after mild annealing to 120 - 150 °C.[52,53] This partial deiodination as already inferred from STM data is further corroborated by XPS, also confirming that Br is not dissociated at all (vide infra). Interestingly, the cyclic Br-I-Br-I halogen-halogen bonding scheme as observed for the intact Br_2I_2Py precursors, was similarly expressed in the densely packed dimer structure. However, the partial deiodination changes the stoichiometry, and the excess Br-substituents that do not find I-substituents as counterparts anymore can additionally contribute to the stabilization by halogen bonds formed with hydrogen-substituents. It is noteworthy that trimers were similarly observed by STM after RT deposition (cf. Fig. A.1).

Mild annealing of the Au(111) samples at 100 °C resulted in the formation of

1D chains, a representative STM image is presented in Figure 4.1(c). A similar center-to-center distance of (1.10 ± 0.10) nm between adjacent units as in the dimers indicates the formation of extended 1D organometallic chains based on C-Au-C linkages. Formation of the interlinks at the 1,6 positions also clearly demonstrates that chain formation is driven by full deiodination without any indication for debromination in agreement with XPS measurements. Owing to the absence of the bright iodine-substituents, the Au atoms in the organometallic links can now be directly recognized in STM as faint spherical feature with an apparent height comparable to the remaining Br-substituents. Based on the mutual arrangement, the packing of the organometallic chains is likewise driven by inter-chain halogen-hydrogen bonds formed between Br-substituents of one chain and the hydrogen atoms of the adjacent chain.

After annealing to 250 °C more disordered structures emerged, but internal resolution was not achieved (Figure 4.1(d)). This finding is in accord with a study by Stöhr et al. of Br_4Py on Au(111) and Cu(111), where higher annealing temperatures also resulted in more disordered and not further resolvable structures.[29] Even though the expected spacing of 0.74 nm for covalently linked pyrenes could be confirmed in these structures.

Further experiments on Au(111) addressed the influence of the preparation protocol. Therefore Br_2I_2Py was deposited onto Au(111) preheated to 100 °C or 250 °C either with a standard deposition rate (deposition time of 3 minutes) or with a 6-fold decreased deposition rate (deposition time of 18 min). The results were essentially similar to RT deposition and subsequent annealing as well as independent of deposition rate: deposition at 100 °C resulted in 1D organometallic chains; deposition at 250 °C afforded not further resolvable disordered agglomerations (cf. Fig. A.2). Moreover, slow heating experiments after RT deposition with a more than 20-fold reduced heating rate (i.e. 0.28 °C min^{-1} instead of 6.6 °C min^{-1}) to 100 °C similarly leads to unaltered 1D organometallic chains (cf. Fig. A.3).

XPS results on Au(111)

Even though for Br_2I_2Py on Au(111) a consistent picture of the surface chemistry is already obtained from STM, further chemical information was acquired by XPS measurements. Since XPS is an ensemble averaging technique, statistically significant information on the progression of the dehalogenation is gained directly. XP spectra of Br 3d, I 3d, and C 1s acquired after RT deposition and after successive

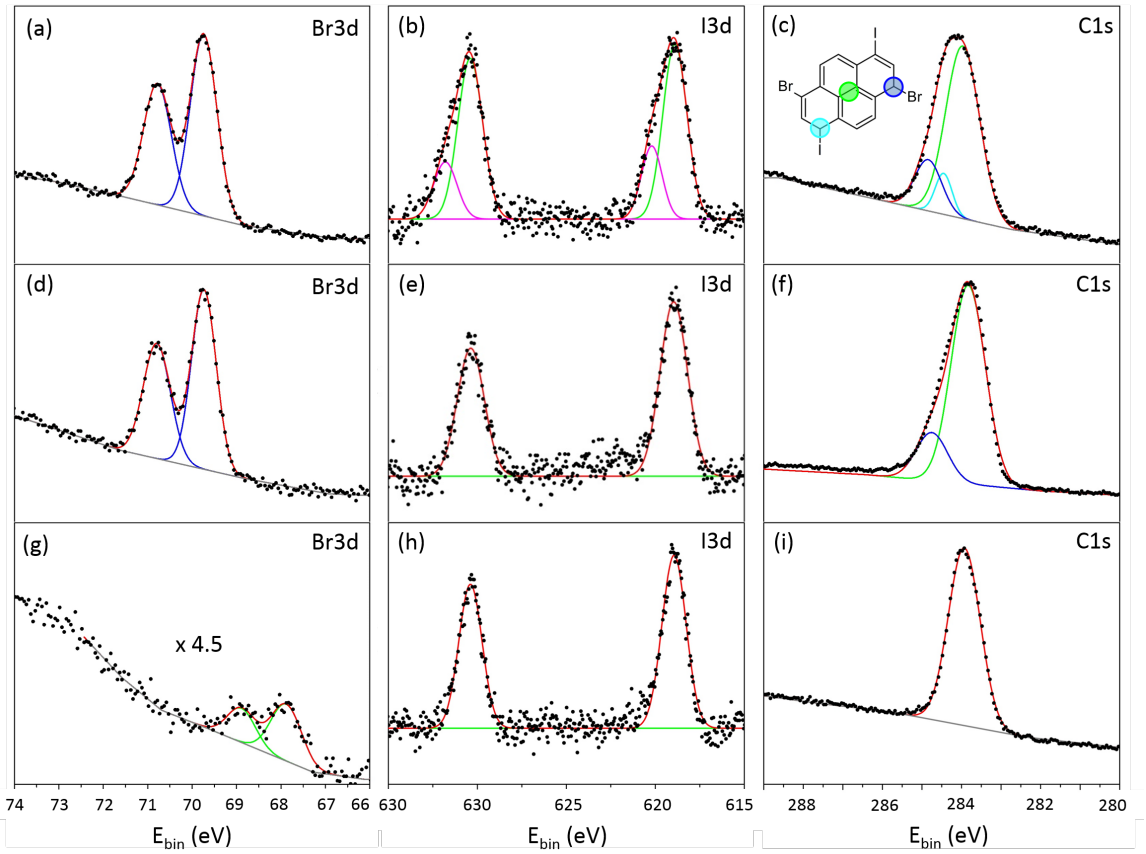

Figure 4.2: XP spectra of Br 3d, I 3d and C 1s of Br_2I_2Py on Au(111) acquired after (a)-(c) (upper row) RT deposition and subsequent annealing to (d)-(f) (middle row) 100 °C, and (g)-(i) (lower row) 250 °C. Raw data are represented by dots; solid lines show fits with a Gaussian line shape and linear background; red lines correspond to the sum of all components. See text body for deduced values of binding energies, chemical shifts, and ratio of components.

annealing to 100 °C and 250 °C, respectively, are summarized in Figure 4.2. After RT deposition Br 3d spectra show the anticipated spin-orbit doublet corresponding to a single chemical species. The measured Br $3d_{5/2}$ binding energy (E_B) of 69.7 eV is in accord with carbon-bound Br (69.7 eV) indicating fully brominated molecules (Figure 4.2(a)).[121] In contrast, I 3d spectra cannot be fitted with a single component, but require two chemically distinct species. According to literature, the species with lower I $3d_{5/2}$ E_B of 618.9 eV corresponds to chemisorbed I on Au(111) and accounts for 73% (peak area) of the total amount (Figure 4.2(b), green). The species with higher I $3d_{5/2}$ binding energy at 620.2 eV corresponds to still carbon-bound I (Figure 4.2(b), magenta).[62,122] Hence, XPS confirms the partial deiodination that was already deduced from STM. Yet, significantly more than 50% deiodination inevitably requires a substantial amount of fully deiodinated precursors as also observed by STM (cf. Fig. A.1). It is worth to note that a comparison between STM and XPS results here also necessarily compares two different samples independently prepared in two different UHV systems. This could be crucial as the degree of deiodination may sensitively depend on the exact surface temperature during deposition and possibly also on the densities of surface defects as step-edges. The C 1s XP spectrum acquired after RT deposition shows the expected main peak from the pyrene backbone at 284.0 eV E_B (Figure 4.2(c), green).[29] The two shoulders at higher E_B originate from the still halogen-substituted carbons with respective binding energies of 284.9 eV for C-Br (Figure 4.2(c), blue) and 284.4 eV for C-I (Figure 4.2(c), light blue). Alternatively, the relative ratio of C-Br and C-I can also be inferred from Br 3d and I 3d. Full bromination and ∼25% remaining iodination means on average 2 C-Br and ∼0.5 C-I per pyrene. These directly determined intensity ratios are consistent with those obtained from fitting the respective C 1s shoulders, suggesting that the relative amounts of carbon and halogens on the surface are still stoichiometric.

After mild annealing the Au(111) samples at 100 °C, the I 3d XP spectrum clearly shows full deiodination (Figure 4.2(e)) without any changes in Br 3d (Figure 4.2(d)). C 1s still features a high E_B shoulder due to the remaining Br-substituents (Figure 4.2(f)). The intensity ratio between shoulder and main peak corresponds to two C-Br per pyrene, also indicating full bromination. On Ag(111) the routinely observed organometallic intermediates are also detectable in C 1s as a low E_B shoulder.[42,43] However, a similar signature is not observed on Au(111), even though STM clearly confirms the organometallic intermediates and in the 1D chains a relatively large fraction of 2 out of 16 carbons are bound to Au atoms. Yet, DFT simulations propose a

smaller C 1s core level shift for C-Au as compared to C-Ag.[40] Hence, the Au-bound carbons are presumably hidden in the C 1s main peak and are not separately resolvable by XPS. However, mild annealing to 100 °C also causes an integral peak shift of C 1s by 0.3 eV to lower E_B as typically observed for organometallic intermediates.[29,42] The origin of this core level shift is not fully understood, but it could be related to alterations of the charge transfer from the surface in the organometallic networks. Since a similar shift was not observed for Br 3d or I 3d, a major effect of a changed surface work function due to chemisorption of dissociated halogens can be ruled out.[29]

Further annealing to 250 °C also activates Br dissociation. This is clearly observed in Br 3d XPS by a pronounced chemical shift for Br $3d_{5/2}$ from 69.7 eV to lower E_B of 67.9 eV (Figure 4.2(g)).[121] The original Br doublet at higher binding energy completely disappeared, indicating complete debromination in this heating step. Moreover, the Br 3d intensity decreased substantially to ∼7.5% of the original value. On the contrary, annealing to 250 °C did not result in observable changes for I 3d, suggesting that iodine remains stably adsorbed while bromine already desorbs (Figure 4.2(h)). This hypothesis is supported by DFT simulations proposing a higher adsorption energy of I on Au(111) as compared to Br.[123] As anticipated the C-Br shoulder at higher E_B disappeared completely, resulting in a comparatively sharp C 1s peak corresponding to the fully dehalogenated pyrene (Figure 4.2(i)). An integral peak shift of 0.1 eV back to higher E_B could be related to the disappearance of the organometallic intermediates. C 1s only shows a ∼14% loss in intensity, so XPS also demonstrates that a large fraction of pyrenes still remained stably adsorbed, even though structural details were not resolved by STM.

NEXAFS results on Au(111)

Additional characterization was carried out by carbon K-edge NEXAFS, also with the aim to obtain more information on the structure obtained after annealing to 250 °C, where STM could not provide useful information anymore. Normalized carbon K-edge NEXAFS spectra acquired for various incidence angles directly after RT deposition and after annealing at 250 °C are summarized in Figure 4.3. Both measurement series show pronounced and relatively sharp resonances at photon energies < 290 eV owing to C 1s $\rightarrow \pi^*$ transitions. The broader resonances observed for photon energies above 290 eV are assigned to C 1s $\rightarrow \sigma^*$ transitions.

The π^*-resonance consists of two separately resolved peaks at photon energies

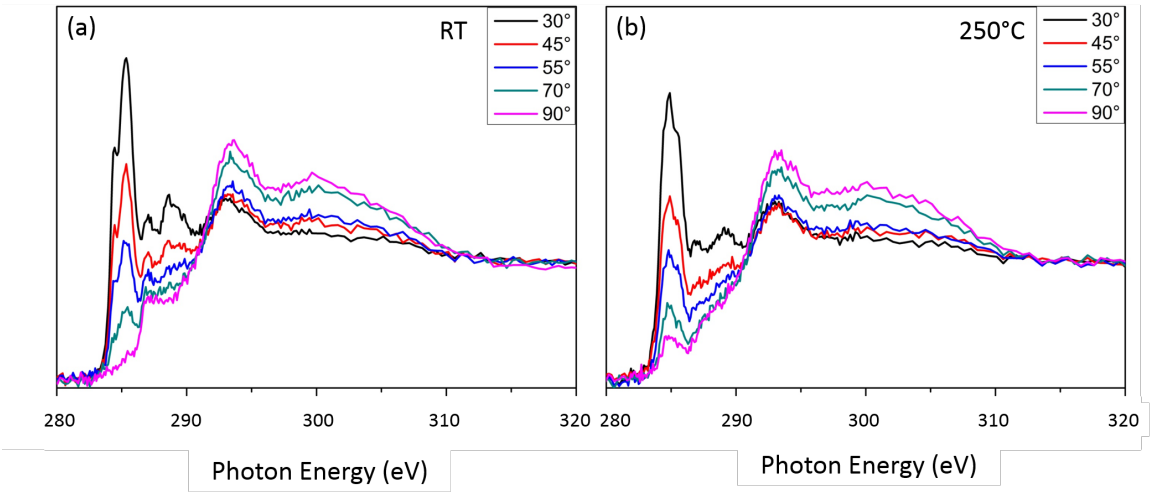

Figure 4.3: Carbon K-edge NEXAFS of Br_2I_2Py on Au(111) after (a) RT deposition and (b) annealing to 250 °C. Normalized and background corrected spectra are shown acquired for five different incidence angles (with respect to the surface, i.e. 90° corresponds to normal incidence).

of 284.5 eV and 285.4 eV. This double peak resonance is typical for polycyclic hydrocarbons and commonly attributed to initial state effects, i.e. chemical shifts in the inequivalent carbon atoms of the pyrene backbones with further contributions from the atomic site where the core hole is localized.[104–106,124] This interpretation is supported by ab initio calculations of Ågren and coworkers.[125] The NEXAFS results are comparable to other pyrenes,[126–130] and there are no distinct features of the Br-substitution or the organometallic bonds. After annealing to 250 °C the pronounced π^*-resonances prevail, but the peak shape changes slightly, possibly related to peripheral chemical reactions. In any case, these NEXAFS results clearly indicate intactness of the pyrene backbones even after annealing to 250 °C.

Both π^* and σ^* resonances exhibit distinct dichroism before and after annealing, indicating a defined and uniform orientation of the pyrenes with respect to the surface.[131] A decrease in intensity of the π^*-resonances with increasing X-ray incidence angle points towards more flat adsorption with a deduced average pyrene tilt angle of $(20° \pm 5°)$ (and $(10° \pm 5°)$ for a second series of measurements). This deviation from the anticipated flat adsorption could be related to adsorption-induced intramolecular distortions as e.g. out-of-plane bending of C-H bonds or preferred adsorption at step-edges at low coverages. Moreover, the exact tilt angle value sensitively depends on the background correction. Visual inspection, in particular of the normal incidence spectrum, shows an increasing slope from lower to higher photon energy in the

region of the π^*-resonances. The origin is not clear, perhaps a broad edge-jump due to chemically different carbon environments. Still, any remaining intensity at the π^*-region from a not appropriately subtracted background results in an apparent tilt. After annealing to 250 °C the pyrene tilt angle increases slightly to (25° ± 5°). So even in the seemingly disordered structure the pyrenes adsorb still relatively flat.

4.4 Results on Ag(111)

STM results on Ag(111)

Although organometallics are not unprecedented on Au(111),[29,47] they are still rarely observed. On the other hand, formation of metastable organometallic intermediates is always observed on Ag(111) surfaces.[43] In order to also study the polymerization of Br_2I_2Py under conditions where organometallic intermediates are expected, further studies were carried out on more reactive Ag(111) surfaces. Figure 4.4(a) shows a typical STM image acquired directly after RT deposition of Br_2I_2Py onto Ag(111). Individual molecules can be recognized as arrangement of four brighter protrusions around a fainter scaffold. The spatial arrangement, i.e. the distances of (0.80 ± 0.08) nm for the long edge and (0.54 ± 0.04) nm for the short edge, of these protrusions facilitates the unambiguous assignment of pyrene molecules. In most cases, protrusions are shared by two adjacent molecules. This is in accord with the anticipated dehalogenation and subsequent formation of organometallic C-Ag-C interlinks.[43] Full deiodination and partial debromination is again confirmed by XPS (vide infra), whereas the size-match of an overlaid organometallic dimer with a center-to-center distance of (1.10 ± 0.10) nm also suggests organometallic linkages. The required Ag atoms were most likely supplied by the free adatom gas, since etch pits that would result from the extraction of surface atoms were never observed.

Although partial debromination prohibits formation of fully reticulated networks, a tetramer of four equally oriented molecules can be already identified (marked by a red circle in Fig. 4.4(a)). In order to initiate the full debromination and to promote structural equilibration by organometallic self-assembly into ordered networks, samples were mildly annealed to 125 °C. The STM image in Figure 4.4(b) confirms porous network formation. Again, the organometallic linkages can be clearly discerned in STM by the bright dots – a signature of the Ag atoms – and also by the increased intermolecular bond length. The organometallic networks still do not exhibit long range order and topologically distinct pores comprised of 3, 4 or 5 molecules

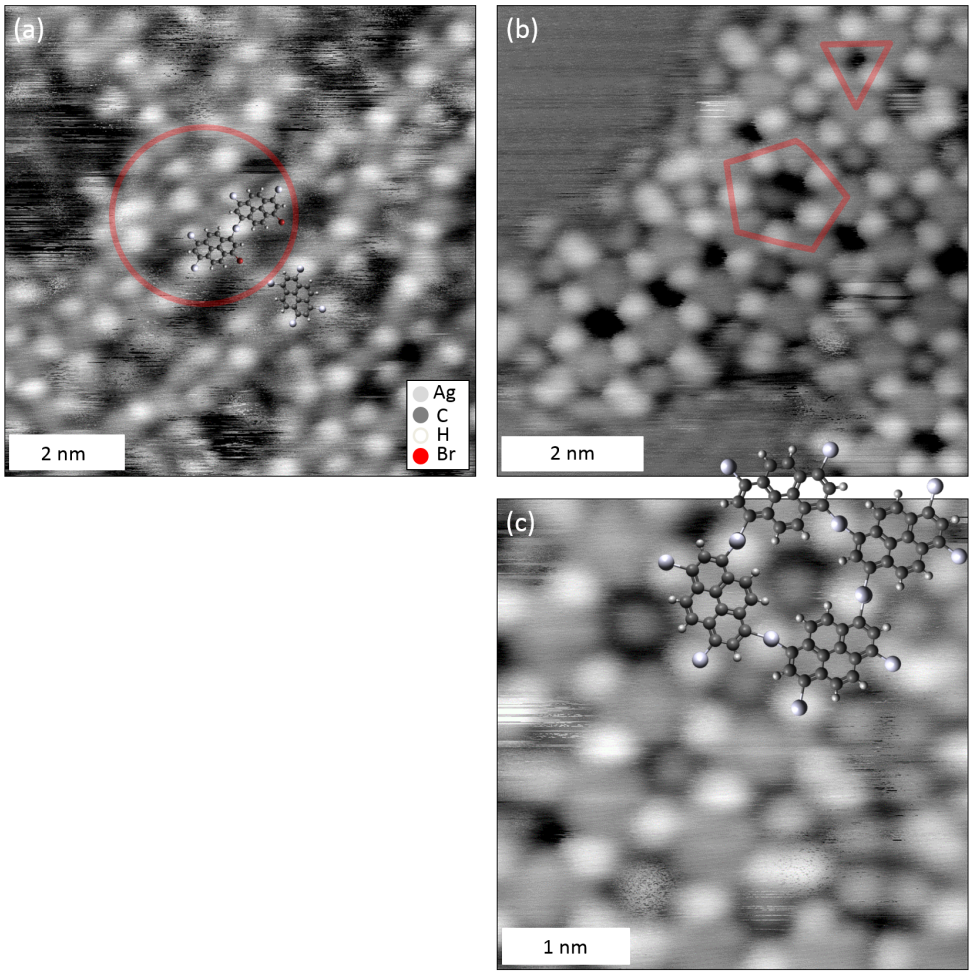

Figure 4.4: STM images of Br_2I_2Py on Ag(111) after (a) RT deposition and (b) / (c) after mild annealing to 125 °C. The overlays show various organometallic structures based on C-Ag-C linkages, the red lines in (b) outline examples for a triangular and a pentagonal pore, the arrow in (c) highlights a dissociated Br or I atom trapped inside a closed pore. (tunneling parameters: (a) 1.08 V, 67 pA; (b) 105 mV, 98 pA; (c) 88 mV, 57 pA)).

can be discerned, examples for a trimeric and a pentameric pore are outlined in Figure 4.4(b). Trimeric pores are formed by three molecules with respective 120° rotation, whereas tetrameric pores can be formed by four molecules with similar orientation, or alternatively with one or two molecules that are rotated by approximately 90°. Pentameric pores also require appropriately oriented molecules, and for any type of pore molecules can be incorporated either with their short or long edge. The various geometries observed here clearly demonstrate a high bond angle flexibility of C-Ag-C linkages. The most likely reason for the absence of long-range order are kinetic effects, but a further influence can also arise from space limitations imposed by chemisorbed halogens.[29] In the close up in Figure 4.4(c) some of the pores are filled with spherical features. These correspond to entrapped dissociated halogens, yet a clear distinction between I and Br solely based on STM imaging is not possible.

Additional experiments with significantly reduced heating and cooling rates (0.28 °C min^{-1} vs. 6.6 °C min^{-1}) aimed at the equilibration of these organometallic networks by exploiting the reversibility of the organometallic linkages.[43] Even though the amount of tetrameric pores could be increased, long-range order was still not attained (cf. Fig. A.4).

In order to study the conversion of the organometallic networks into 2D cross-linked covalent networks, samples were further annealed to 200 °C. Yet, this thermal activation merely resulted in desorption of the molecules from Ag(111), as also corroborated by the C 1s XPS intensity (cf. Fig. A.5). This implies that the activation barrier for covalent coupling is larger than for removing the molecules from the surface (vide infra). Mechanistic details of this desorption process are not known, but it appears most plausible that the organometallic networks first dissociate and the monomers subsequently desorb as individuals. In order to promote the conversion from organometallic to covalent, further experiments were carried out with simultaneous UV light irradiation during sample heating. However, UV illumination could not prevent desorption, but even lowered the desorption temperature to < 190 °C, presumably by weakening the organometallic bonds.

XPS results on Ag(111)

On Ag(111) the chemical state was similarly assessed by XPS measurements of Br 3d, I 3d and C 1s regions. Directly after RT deposition, the coexistence of two chemically distinct species in the Br 3d region indicates partial debromination (Figure 4.5(a)). The Br $3d_{5/2}$ binding energies of 70.2 eV[132] (blue curve) and 68.2 eV (green curve)[42,43]

agree well with literature values of carbon-bound and chemisorbed Br on Ag(111), respectively. According to the peak area ratios, ∼27% of Br is spontaneously dissociated at RT. In contrast, I 3d in Figure 4.5(b) shows a narrow doublet corresponding to a single species and the I $3d_{5/2}$ binding energy of 618.8 eV is in accord with literature values of chemisorbed I,[61] confirming full deiodination on Ag(111). The C 1s line shown in Figure 4.5(c), is relatively broad and peak fitting requires three different components: carbon atoms of the pyrene backbone (Cpy) at 284.6 eV[118] (green) and shoulders at higher and lower E_B, respectively. Those can be assigned to still brominated carbon atoms (C-Br) at 285.2 eV[42] (blue) and carbon atoms directly linked to Ag atoms (C-Ag) at 284.0 eV (light blue). Since all dehalogenated carbon atoms form organometallic bonds, expected intensity ratios for the different carbon species can alternatively be derived from the known degrees of deiodination (full) and debromination (∼25%). The anticipated ratio of Cpy : C-Ag : C-Br = 12 : 2.5 : 1.5 = 75% : 15.6% : 9.4% is in perfect agreement with the experimentally found values: Cpy : C-Ag : C-Br = 77% : 14% : 9.0%, again suggesting stoichiometric adsorption.

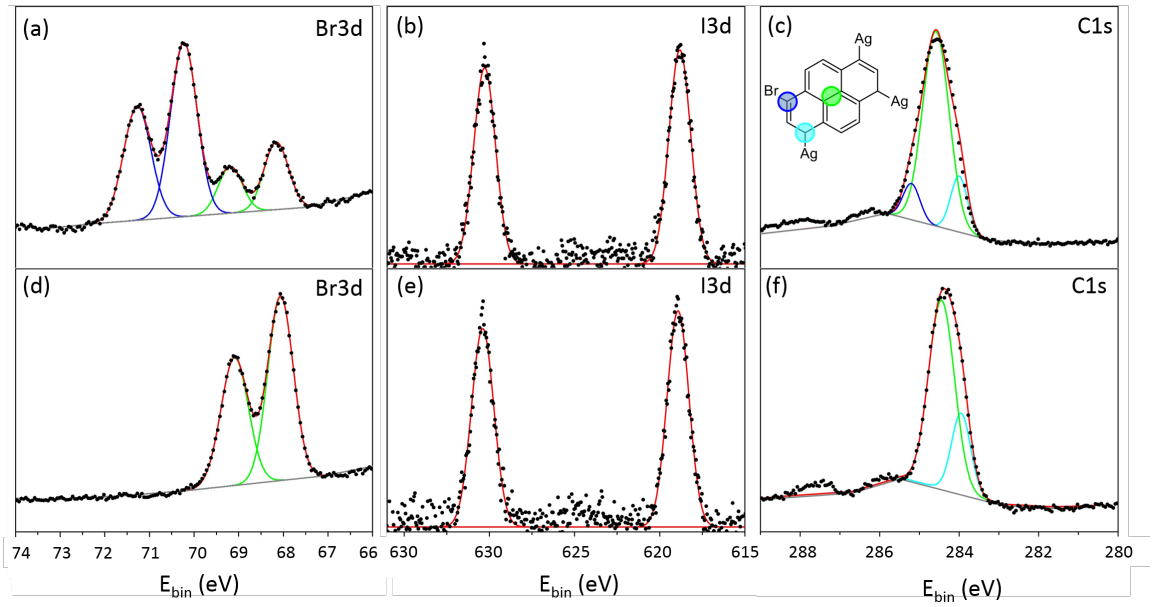

Figure 4.5: XP spectra of Br 3d, I 3d and C 1s of Br_2I_2Py on Ag(111) acquired after (a)-(c) (upper row) RT deposition and subsequent annealing to (d)-(f) (lower row) 125 °C. Raw data are represented by dots; solid lines show fits with a Gaussian line shape and linear background; red lines correspond to the sum of all components. See text body for deduced values of binding energies, chemical shifts, and ratio of components.

A further series of XPS measurements was carried out on Ag(111) after mild annealing to 125 °C. Br 3d XP spectra exclusively show the chemisorbed species at lower E_B, confirming full debromination (Figure 4.5(d)). No changes in binding energy and intensity were observed for I 3d (Figure 4.5(e)). Moreover, the full debromination can also be recognized in the C 1s spectrum, where the high E_B shoulder associated with C-Br fully disappeared. By the same token the relative intensity of the low E_B shoulder associated with C-Ag increases up to a relative amount of 28% of the total intensity (Figure 4.5(f), light blue), in accord with the expected value of 25% (4 out of 16 carbons) for full dehalogenation and formation of organometallic linkages at all sites. Since STM indicates relatively small domains with a notable amount of boundaries, these results suggest that the reactive sites at the periphery are also terminated by C-Ag bonds. Interestingly, the increased amount of organometallic linkages results in a further integral peak shift of C 1s by 0.17 eV to lower E_B as similarly observed on Au(111).

After annealing to 250 °C no intensity of C 1s was detected anymore, indicating complete desorption of the molecules. For Br 3d a ∼30% intensity loss indicates the onset of Br desorption, whereas the I 3d intensity still remained unaffected.

NEXAFS results on Ag(111)

NEXAFS experiments were also carried out on Ag(111), normalized carbon K-edge spectra are depicted in Figure 4.6. NEXAFS spectra acquired on Ag(111) both after RT deposition (Fig. 4.6(a)) and after annealing to 125 °C (Fig. 4.6(b)) show two main regions: strong and sharp π^*- and broader σ^*-resonances for photon energies below and above 290 eV, respectively. Analogous to the results on Au(111), owing to the presence of two chemically distinct carbon atoms in the pyrene backbone, the π^*-resonances exhibit a similar double peak structure with individually resolved peak maxima at photon energies of 284.4 eV and 285.3 eV. The resonances at 287.1 eV and 289.6 eV presumably have a mixed character (σ^*(C-H) and σ^*(C=C)).[127,128]

In contrast to Au(111), the NEXAFS spectra on Ag(111) exhibit an additional relatively sharp resonance at 288.5 eV. Since this feature is entirely absent on Au(111), it is tentatively attributed to the Ag atoms in the organometallic C-Ag-C linkages as further discussed below. Annealing to 125 °C does not lead to significant changes, confirming the intactness of the pyrene backbones. Yet, slight changes in the substructure of the π^*-resonances are observed toward almost equal intensity of the two individual contributions. On Ag(111), the X-ray absorption also showed a pronounced

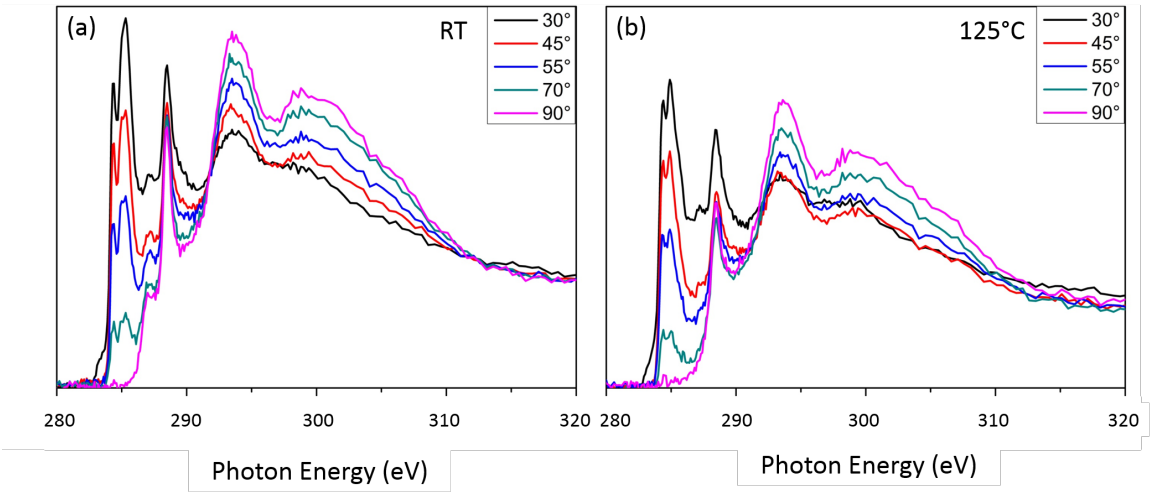

Figure 4.6: Carbon K-edge NEXAFS of Br_2I_2Py on Ag(111) after (a) RT deposition and (b) annealing to 125 °C. Normalized and background corrected spectra are shown acquired for five different incidence angles (with respect to the surface, i.e., 90° corresponds to normal incidence).

dichroism. Yet, in contrast to Au(111) the intensity at normal incidence (90°, electric field vector parallel to the surface) became zero, indicating perfectly flat adsorption of the pyrene backbone on the surface both directly after RT deposition and after annealing to 125 °C.

4.5 Discussion

For Br_2I_2Py on Au(111) sequential dehalogenation with a clear separation between deiodination and debromination was consistently observed by STM and XPS, in line with previous studies on other aromatic compounds.[48,52,53] The only partial deiodination at RT appears more surprising. In STM the partial deiodination is expressed in the observation of long-range ordered self-assembled structures of either intact Br_2I_2Py molecules or organometallic dimers linked via Au atoms. Yet, XPS indicates ~75% deiodination that is inconsistent with STM results. However, self-assembly can selectively stabilize smaller and uniform aggregates as monomers and dimers, hence leading to their overrepresentation in STM data. Interestingly, the formation of first covalent interlinks as reported for Br_4Py on Au(111) was not observed here,[29] even though the two pyrene derivatives should be fairly comparable. Two factors might account for the incomplete deiodination at RT: dissociation of one iodine-substituent and subsequent formation of an organometallic bond to Au atoms with lower ad-

sorption height could result in a slightly tilted adsorption geometry of the pyrene. Thereby the adsorption height of the second iodine-substituent on the same molecule is increased, resulting in a diminished activity of the Au(111) surface for halogen dissociation and an increased dehalogenation temperature, respectively. The proposed effect should be more pronounced for molecules with a relatively rigid backbone as pyrenes. A possible experimental indication are the surprisingly high pyrene tilt angles on Au(111) as found by NEXAFS even though alternative explanations cannot be ruled out. The observation of metastable organometallic intermediates for Br_2I_2Py also on Au(111) is interesting, but not without precedence.[29,47] Even though safely identified in STM, XPS of C 1s did not show the low E_B shoulder typically observed for organometallics on more reactive surfaces as Ag(111). This is presumably related to the comparatively small core level shifts associated with C-Au bonds,[40] as intuitively understandable from the comparable electronegativities of C and Au. On the other hand, for a singly iodinated triphenylbenzene derivative, we observed direct covalent coupling into dimers on Au(111) already at RT,[48] clearly indicating additional influences of molecular structure and / or reaction conditions. On the other hand, it is not a priori clear whether in these cases the organometallic intermediates do not exist at all or whether the conversion to covalent occurs too fast to be experimentally observed. For pyrenes, however, the steric hindrance in the 1-1' covalently coupled adsorbed state is substantial, giving rise to a larger barrier for the conversion to covalent linkages, hence stabilizing the organometallic intermediates. In this respect, the observation of extended 1D organometallic chains on Au(111) after mild annealing to 100 °C is less surprising, as this only drives full deiodination, but does not change the general surface chemistry.

Based on this, the formation of 2D cross-linked organometallic networks could be expected after dissociation of the remaining bromine-substituents. However, debromination and conversion of the organometallic into covalent linkages takes place at comparable temperatures and could not be separately accomplished. Full debromination after annealing to 250 °C was confirmed by XPS. Instead of organometallic networks, however, STM revealed more disordered structures, where single pyrene entities could not be resolved anymore in accord with the previous work of Stöhr.[29] On the other hand, NEXAFS indicates intactness of the pyrene backbones, where a shape change of the π^*-resonance might be related to peripheral chemical changes. Quantitative analysis results in an average pyrene tilt angle of ($25° \pm 5°$), possibly related to the large dihedral angle between covalently linked pyrenes.

On Ag(111) full deiodination as well as partial debromination followed by formation of organometallic networks was observed after RT deposition of Br_2I_2Py. These results are in line with previous studies of related compounds on Ag(111).[43,113] Similar to Au(111), the organometallic intermediates can be safely identified by STM through the extended bond length, but also in most cases by the prominent contrast signature of the interlinking Ag atom. Moreover, the organometallic intermediates feature pronounced spectroscopic signatures: a low E_B shoulder in C 1s XPS and an additional resonance in carbon K-edge NEXAFS as further discussed below; Mild annealing to 125 °C induced a structural reorganization of the organometallic networks on Ag(111) that is only possible if the C-Ag-C bonds become reversible. In contrast to Au(111), NEXAFS indicates entirely planar adsorption of the pyrene backbone on Ag(111) both after RT deposition and after mild annealing to 125 °C. This is expected, since the C-Ag-C linkages are significantly longer than the direct C-C bonds, and hence alleviate the steric hindrance that accounts for a tilted geometry. At this point, the origin of the difference to Au(111) where a slightly tilted adsorption geometry was found remains unclear. Yet, a possible further explanation could be offered by the remaining halogen substituents on Au(111), whereas on Ag(111) the higher degree of dehalogenation pins down the molecules more symmetrically.

NEXAFS spectra exhibit an unexpected additional relatively sharp resonance at a photon energy of 288.5 eV, i.e. between the π^*- and σ^*-resonances of the pyrene backbone. Interestingly, this additional resonance is exclusively observed on Ag(111), but not Au(111). If assigned to a C 1s $\rightarrow \pi^*$ transition, the incidence angle dependency of the intensity would result in a pyrene tilt angle of 50°. Such an unrealistically large value is clearly contradicting flat adsorption of the pyrene as deduced from the actual π^*-resonance and as intuitively expected. This apparent discrepancy can by resolved by proposing an electronic transition from the pyrene C 1s core levels into unoccupied electronic states of the Ag atoms in the organometallic linkages as origin of this resonance. In this respect, the additional NEXAFS resonance represents a new spectroscopic signature of the organometallic intermediates related to the unoccupied electronic states of the C-Ag-C linkage. This explanation inevitably raises the question as to why a comparable feature is not observed for the organometallic structures on Au(111). The most plausible explanation is related to differences of unoccupied electronic states of Au vs. Ag atoms in the organometallic linkages. A first hint lies in the different STM contrast of Au vs. Ag atoms in C-metal-C linkages, but only electronic structure calculations could provide more insights.

	TS energy (eV)	FS energy (eV)
Au-bonded / planar	+2.60	+1.20
Au-bonded / non-planar	+2.04	-0.34
Ag-bonded / planar	+1.88	-0.05
Ag-bonded / non-planar	+1.09	-1.37

Table 4.1: Transition state (TS) and final state (FS) energies for the conversion of organometallic into covalent pyrene dimers. In all cases, the initial state energy corresponds to 0.00 eV, i.e. the reaction barrier is given by the TS energy.

Even though 2D cross-linked covalent networks could neither be obtained on Au(111) nor on Ag(111), there are still important differences between both surfaces: on Au(111) the organometallic intermediates are converted into disordered, presumably covalent aggregates with still intact, but possibly chemically altered pyrenes; on Ag(111) the organometallic intermediates disappear completely and the pyrenes just desorb. This finding appears counterintuitive, as the notoriously stronger adsorbate-surface interactions on Ag(111) should prevent the desorption more effectively. However, for pyrenes the stronger interactions with Ag(111) could indeed disfavor covalent coupling: The conversion from organometallic to covalent linkages results in a substantial increase of steric hindrance that is alleviated by a relatively large tilt angle between the involved pyrenes. In order to shed more light on the energetics of the conversion of organometallic into covalent linkages, reaction barriers were calculated by gas phase DFT simulations for both Ag- vs. Au-bonded and constrained to planar vs. non-planar dimers. The results are summarized in Table 4.1 (cf. Fig. A.7 for structures).

Irrespective whether or not the structures were constrained to planar, reaction barriers for Au-bonded are always higher than for Ag-bonded dimers. The differences in planar vs. non-planar final state energies largely correspond to the DFT-derived energy cost of +1.35 eV for planarization of a covalent dimer in the gas phase (cf. Fig. A.6). The higher values obtained with Au may appear surprising, but merely reflect the higher bond strength of C-Au as compared to C-Ag. Along these lines, higher binding energies for phenyl or smaller hydrocarbon radicals were also proposed for Au as compared to Ag surfaces based on DFT simulations.[40,133] For the non-planar organometallic pyrene dimers, DFT yields bond dissociation energies of 4.79 eV and 3.48 eV for the Au- and Ag-bonded dimer, respectively, implying that each C-Au bond is ∼0.66 eV stronger than the C-Ag bond. This substantial difference in bond dissociation energies – being even larger than the difference in reaction barriers be-

tween Au and Ag – also provides the base for explaining the deviating experimental results on both surfaces: The high C-Au bond strength stabilizes the organometallic structures up to the higher surface temperatures that are required to thermally surmount the conversion barrier, whereas the relative weakness of the C-Ag bonds cannot prevent dissociation of the organometallic networks during annealing, which is also entropically favored. Once the organometallic structures disintegrate at higher temperatures, the relatively small individual pyrene molecules then desorb from the Ag(111) surface.

4.6 Summary and conclusion

In summary, we studied and compared the on-surface polymerization of Br_2I_2Py on Au(111) vs. Ag(111). To overcome the expected and previously reported large steric hindrance of 1-1' coupled pyrenes, we propose a sequential polymerization into first 1D chains followed by their fusion into 2D cross-linked polymers. This reaction sequence was already encoded in the structure of the Br_2I_2Py precursor through the bromine- and iodine-functionalization that employs the well-known conveniently large differences in activation temperatures for deiodination and debromination on coinage metal surfaces. RT deposition of Br_2I_2Py on Au(111) just resulted in partial deiodination, and STM revealed ordered arrangements of both intact Br_2I_2Py molecules and organometallic dimers based on C-Au-C linkages. Mild annealing at 100 °C on Au(111) results in full deiodination and the formation of extended 1D organometallic chains as intended by the halogen substitution pattern of Br_2I_2Py. On Ag(111) the surface chemistry of Br_2I_2Py is comparable to other halogenated aromatic molecules: full deiodination and partial debromination after RT deposition with subsequent formation of organometallic interlinks. The C-Ag-C linkages become reversible upon mild annealing at 125 °C, facilitating structural equilibration to some extent through "organometallic self-assembly". Interestingly, the organometallic networks were unambiguously detected in XPS as low E_B shoulder of the C 1s line only on Ag(111), but not on Au(111). Furthermore, in carbon K-edge NEXAFS an additional resonance appeared between the π^*- and σ^*-resonances of the pyrene backbone, again only on Ag(111), but not on Au(111). Owing to the odd incidence angle dependence of its intensity this additional resonance is attributed to electronic transitions from pyrene C 1s core levels into unoccupied electronic states of Ag atoms in the C-Ag-C linkages. Hence this resonance represents a further spectroscopic signature of the organometallic intermediates.

Conversion of the organometallic into structurally well-defined covalent networks was not possible on both surfaces: on Au(111) covalent pyrene networks may have formed, as XPS confirms full debromination, NEXAFS proves the intactness of the pyrene entities, and molecular structures remained stable on the surface at higher annealing temperatures. However, these might be highly non-planar and structurally not very well-defined, rendering further structural characterization by STM impossible. On Ag(111) higher annealing of the organometallic networks just resulted in desorption. The differences can be rationalized and traced back to the higher binding energy of C-Au as compared to C-Ag organometallic bonds as suggested by a comparison of DFT-derived reaction barriers for the conversion and bond dissociation energies of organometallic dimers.

In summary, covalent interlinking of pyrenes into well-defined quasi 2D networks on surfaces remains intricate, not only due to the large steric hindrance, but also due to the interference of metal adatoms. This results in the formation of relatively stable organometallic networks, where comparatively high temperatures are needed for the conversion to covalent networks. In general, higher annealing temperatures are undesirable in on-surface synthesis, since this always imposes a certain risk of unwanted side reactions or (partial) detachment from the surface. Yet, appropriately substituted pyrenes still remain highly interesting for the on-surface synthesis of conjugated 2D polymers.

4.7 Materials and methods

STM, XPS, and NEXAFS experiments were carried out under ultrahigh vacuum (UHV) conditions with a base pressure below 3×10^{-10} mbar. Ag(111) and Au(111) single crystals surfaces as well as epitaxial Au(111) films on mica were prepared by cycles of 0.5 keV Ar^+-ion sputtering and annealing at 500 °C. Br_2I_2Py was deposited by thermal sublimation from a home-built Knudsen-cell[91] with crucible temperatures ranging from 165 °C to 180 °C. In order to exclude an additional influence of surface coverage, the deposition times were adjusted to yield comparable coverage of ∼0.3 monolayer. STM data were acquired in-situ at RT with a home-built instrument controlled by a commercial SPM100 controller (RHK Technology Inc.). NEXAFS and XPS experiments were carried out in a Prevac endstation at the HE-SGM beamline at Helmholtz-Zentrum Berlin. Carbon K-edge NEXAFS spectra were acquired in the analysis chamber using a home-built double channel plate detector in partial electron yield mode (V = -150 V). XP spectra of C 1s, Br 3d, and I 3d were acquired

with a Scienta R3000 electron analyzer at normal electron emission with photon energies of 450 eV for C 1s / Br 3d and 750 eV for I 3d. A pass energy of 50 eV was used in all cases, and Au $4f_{7/2}$ and Ag $3d_{5/2}$ binding energies of 84.0 eV[134] and 368.2 eV,[135] respectively were used for energy calibration. Density functional theory (DFT) calculations were performed with the VASP code,[136] projector augmented wave potentials[137] and plane waves expanded to a kinetic energy cutoff of 400 eV. Exchange-correlation effects were treated by the PBE functional and all structures were optimized until the residual forces on all atoms were smaller than 0.01 eV $Å^{-1}$.[138] Reaction barriers were calculated using the Climbing Image Nudge Elastic Band[139] and the dimer methods.[140] Bond dissociation energies were calculated by comparing the energies of organometallic structures with those of the individual subsystems (i.e. Au / Ag atom and pyrene radical). All calculations included spin-polarization.

5 Remote functionalization in surface-assisted dehalogenation guided by conformational mechanics: organometallic self-assembly of 3,3',5,5'-tetrabromo-2,2',4,4',6,6'-hexafluorobiphenyl on Ag(111)

The following section shows the results and interpretation of the second exemplary surface-assisted Ullmann reaction of this thesis. A perfluorinated and brominated biphenyl precursor is studied on Ag(111). The section is published and reproduced from: M. Lischka, G. S. Michelitsch, N. Martsinovich, J. Eichhorn, A. Rastgoo-Lahrood, T. Strunskus, R. Breuer, K. Reuter, M. Schmittel, W. M. Heckl, and M. Lackinger: Remote functionalization in surface-assisted dehalogenation guided by conformational mechanics: organometallic self-assembly of 3,3',5,5'-tetrabromo-2,2',4,4',6,6'-hexafluorobiphenyl on Ag(111), *Nanoscale*, **2018**, 10, 12035–12044 with permission from The Royal Society of Chemistry.

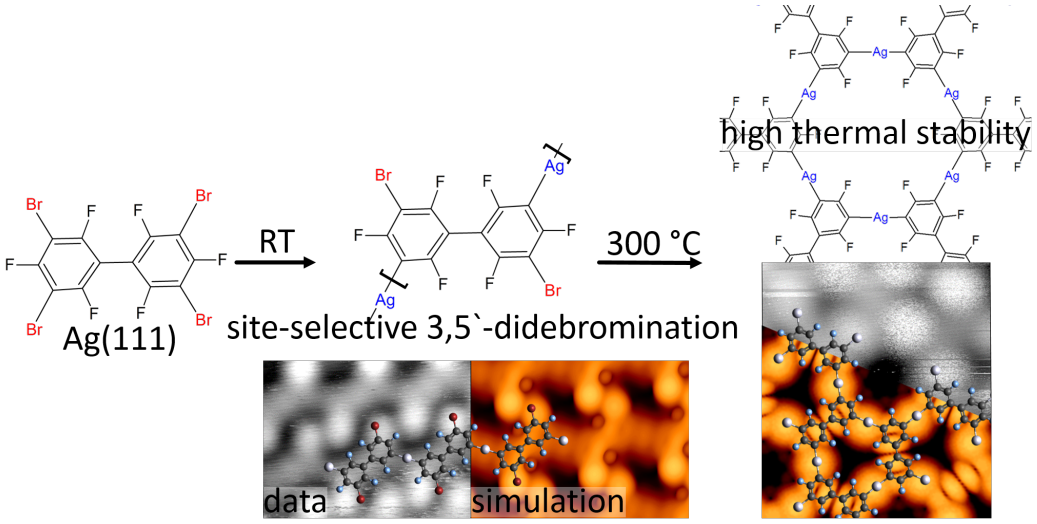

I performed all the experiments and the corresponding data analysis and interpretation, and prepared the manuscript under supervision of Prof. Lackinger. The co-authors J. Eichhorn, A. Rastgoo-Lahrood and Dr. T. Strunskus gave support during synchrotron measurements, while R. Breuer synthesized the precursor under supervision of Prof. Schmittel. G. Michelitsch provided the DFT calculations, STM image and XPS core level simulations under supervision of Prof. Reuter.

5.1 Abstract

Even though the surface-assisted dehalogenative coupling constitutes the most abundant protocol in on-surface synthesis, its full potential will only become visible if selectivity issues with polybrominated precursors are comprehensively understood, opening new venues for both organometallic self-assembly and on-surface polymerization. Using the 3,3',5,5'-tetrabromo-2,2',4,4',6,6'-hexafluorobiphenyl (Br_4F_6BP) at Ag(111), we demonstrate a remote site-selective functionalization at room temperature and a marked temperature difference in double- vs. quadruple activation, both phenomena caused by conformational mechanical effects of the precursor-surface ensemble. The submolecularly resolved structural characterization was achieved by Scanning Tunneling Microscopy, the chemical state was quantitatively assessed by X-ray Photoelectron Spectroscopy, and the analysis of the experimental signatures was supported through first-principles Density-Functional Theory calculations. The non-planarity of the various structures at the surface was specifically probed by additional Near Edge X-ray Absorption Fine Structure experiments. Upon progressive heating, Br_4F_6BP on Ag(111) shows the following unprecedented phenomena: (1) formation of regular organometallic 1D chains via remote site-selective 3,5'-didebromination; (2) a marked temperature difference in double- vs. quadruple activation; (3) an organometallic self-assembly based on reversibility of C-Ag-C linkages with a thus far unknown polymorphism affording both hexagonal and rectangular 2D networks; (4) extraordinary thermal stability of the organometallic networks. Controlled covalent coupling at the previously Br-functionalized sites was not achieved for the Br_4F_6BP precursor, in contrast to the comparatively studied non-fluorinated analogue.

5.2 Introduction

Over the last decade, the bottom-up fabrication of metal-organic and covalent nanostructures on solid surfaces has gained significant interest and momentum.[9,109,141,142] The main idea and benefit of such on-surface synthesis are to combine the stability gained by strong interlinks with the versatility of molecular systems. This approach afforded an intriguing variety of atom-precise structures, comprising covalent 1D wires, chains, and ribbons, as well as 2D networks including first steps towards electronic conjugation.[48,143] For metal-organic networks the chemical structure of the ligands and choice of coordination centers both facilitate tuning and tailoring

of network topologies and properties. In this respect, the introduction of iron or cobalt as the coordination center promises unsurpassed catalytic or magnetic properties.[144,145] Moreover, recently unique 5-fold coordination motifs were realized in a 2D environment using rare-earth metals, even resulting in networks with quasicrystalline characteristics.[77] An intriguing variant are the organometallic structures based on carbon-metal-carbon linkages that are routinely observed as metastable intermediates on silver and copper surfaces upon dissociation of halogen substituents that act as leaving groups. Both metal-coordination and organometallic linkages can become reversible, as important premise for self-assembly of highly ordered networks.[146] Moreover, structural equilibration in organometallic networks represents a viable route to improve the structural quality of the corresponding covalent networks that are obtained through a thermally activated isostructural conversion.[43,55,57,147] Yet, inducing reversibility in organometallic bonds typically requires higher temperatures as compared to their metal-organic counterparts. In general, the surface-templated bottom-up synthesis of 2D materials with unprecedented chemical, structural, and electronic properties is highly inspiring for nanotechnological applications in a broad variety of fields such as electronics, sensors, separation, and catalysis.[22,148]

In principle, on-surface synthesis facilitates reticular design of novel 2D materials, predetermining arbitrary ordered structures through the judicious choice of the assembling molecular units. However, limited regioselectivity, side reactions, surface influence, and the absence of error correction due to the irreversibility of newly established covalent links render this conceptually straightforward approach challenging in practice. In this respect, well-behaved and controllable coupling reactions for fusing the molecular units are of crucial importance. To date, surface-assisted Ullmann coupling is the most reliable and predictable workhorse to achieve linking via C-C bonds,[8] which furthermore benefits from the abundant availability of the employed halogenated precursors. Ullmann coupling is based on aryl halides that can easily be dissociated on metal surfaces, in most cases Cu, Ag, or Au. The generated surface-stabilized radicals may subsequently recombine to form new C-C linkages, either directly or via metastable organometallic intermediates.[42,43] Consequently, research on organometallic self-assembly was initially fueled by the large interest in on-surface synthesis of covalent nanostructures, but has now become a topic of its own.

Despite this relevance and significant research efforts into the dehalogenation as the preceding step for both organometallic self-assembly and Ullmann coupling, many central issues of reactivity, chemo- and regioselectivity are still poorly un-

derstood. For instance, 1,3-bis(p-bromophenyl)-5-(p-iodophenyl) benzene showed full deiodination and ∼38% debromination after room temperature deposition onto Ag(111), but debromination was only completed at ∼260 °C.[43] In stark contrast, 1,3,5-tris(p-bromophenyl)benzene was not debrominated at all after room temperature deposition onto Ag(111), but already fully debrominated upon annealing to ∼120 °C.[149] Such examples of differential reactivity highlight the current lack of understanding, which prevents a higher level of control in on-surface synthesis that is an absolute necessity for improving the notoriously low structural qualities, currently the most crucial hindrance for applications.

Here we address the reactivity as well as chemo- and regioselectivity of surface-assisted debromination in 3,3',5,5'-tetrabromo-2,2',4,4',6,6'-hexafluorobiphenyl (Br_4F_6BP, cf. Fig. 5.1(a) for its structure) as a prototypical representative of a perfluorinated oligobromoarene. Fluorine substitution constitutes an important strategy to chemically alter relevant properties of neighbouring groups and is additionally expected to influence formation, reversibility, and stability of organometallic networks. In general, fluorination enhances the electron acceptor properties, and attractive electronic properties were predicted for edge-fluorinated graphene nanoribbons.[132,150]

We explore the thermally activated surface chemistry of Br_4F_6BP by a multi-technique approach, comprising a deep structural, chemical, and first-principles computational characterization. The bond dissociation energy of F-C in the gas phase of 5.4 eV even exceeds the value of 5.1 eV for C-C bonds, suggesting that activation of the fluorinated sites is rather unlikely, even if the proximity of a surface can promote defluorination.[39,151] Given the high volatility of Br_4F_6BP, the more reactive Ag(111) surface was chosen, as thermally activated surface chemistry is not feasible on more noble Au(111) surfaces due to preferential desorption of the precursors upon heating (cf. Sec. B.4). The key findings for Br_4F_6BP and its comparatively studied non-fluorinated analogue 3,3',5,5'-tetrabromobiphenyl (Br_4BP) on Ag(111) are summarized in Fig. 5.1.

A priori, various effects of the perfluorination are conceivable: (1) the C-Br bond strength ought to be modified by inductive effects, resulting in altered debromination barriers / temperatures and reaction kinetics, respectively. By the same token, the strength of the C-Ag-C linkages in the organometallic intermediate could be altered. (2) The gas phase structure of Br_4F_6BP is highly non-planar with a large dihedral angle and rotational barrier at the biphenyl unit due to the ortho-fluorine substituents, which could have consequences for the surface chemistry and the regios-

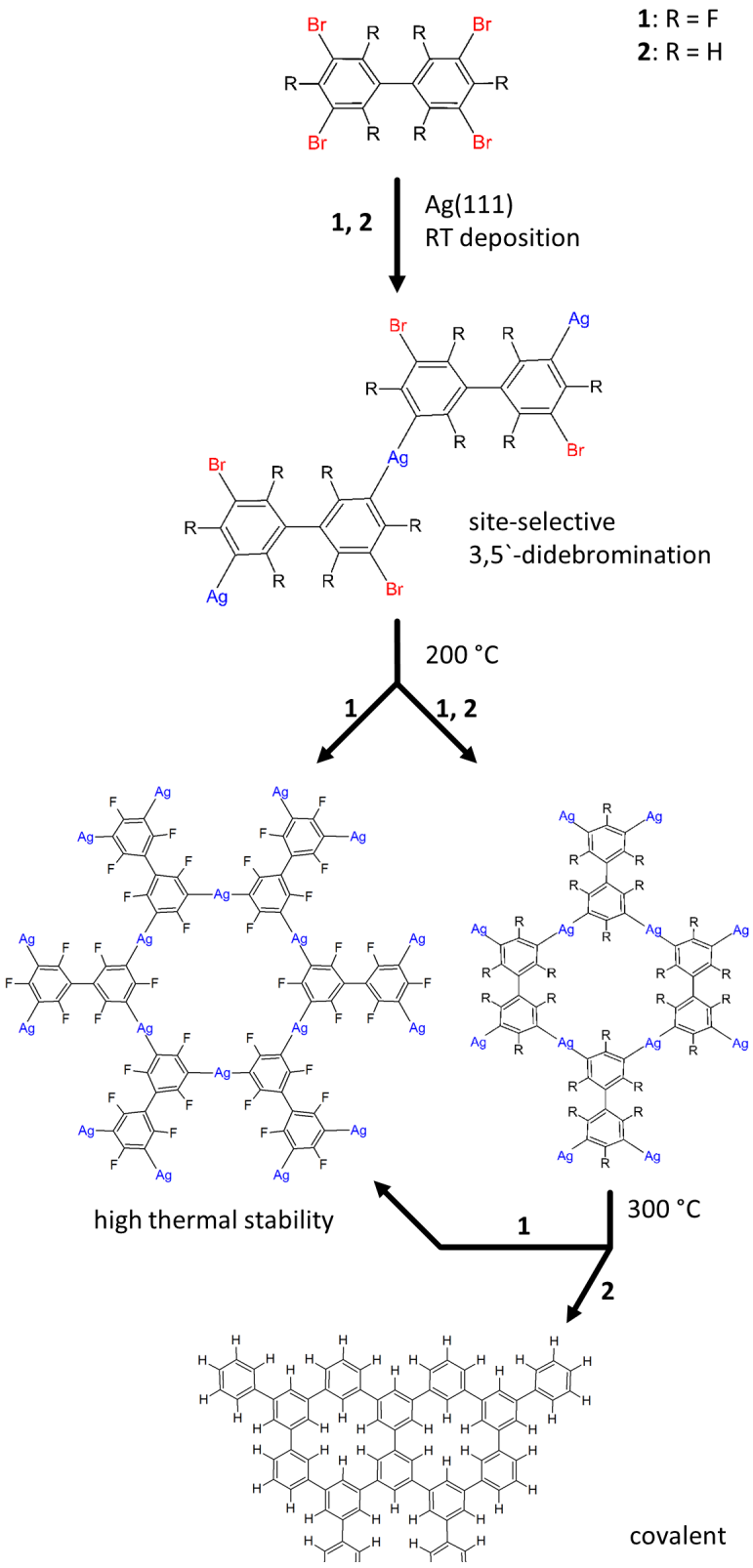

Figure 5.1: Overview over the thermally induced structural and chemical changes of Br_4F_6BP and Br_4BP on Ag(111).

electivity of the second debromination step. (3) The ortho-fluorine atoms next to the reactive C-Br gives rise to an additional barrier for the covalent aryl-aryl coupling. (4) The high electronegativity of fluorine influences non-covalent intermolecular bonds that steer the organization of precursors as well as reaction intermediates and products. Direct effects are expected due to the negative partial charge, but fluorine substituents can also enhance the halogen bond strength of neighbouring bromine or iodine substituents,[152] or even directly form halogen bonds.[153]

5.3 Results

After room-temperature deposition (RT) of Br_4F_6BP onto Ag(111) two different structures were observed by STM, representative images are depicted in Fig. 5.2(a) and (b) (cf. Fig. B.1(a) / (b) for overview images). Evidently, the structure shown in Fig. 5.2(a) consists of interdigitated 1D chains. A perfect geometrical match is achieved with organometallic chains based on C-Ag-C linkages that result from exclusive didebromination of the precursors across the diagonal, i.e. at the 3- and 5'-positions. The bright protrusions on alternating sides of the chains are attributed to remaining bromine substituents at the 5- and 3'-positions. The experimentally determined repeat distance of (1.06 ± 0.10) nm is consistent with the DFT-derived value of 1.02 nm found for a periodic planar chain, excluding direct covalent bond formation that would result in a ∼0.25 nm smaller value.[43]

Chain interdigitation is likely driven by weak halogen bonding between the remaining Br- and the F-substituents. The more regular and densely packed structure in Fig. 5.2(b) features an oblique unit cell with a = (1.06 ± 0.06) nm, b = (0.78 ± 0.08) nm, $\gamma = 85°$. Also this structure matches perfectly with organometallic chains, yet with a higher packing density. This assignment is corroborated by the equal repeat distance in chain direction (corresponding to lattice parameter a) and the pronounced STM contrast at the positions of the remaining bromine substituents. The average chain length in the less densely packed structure corresponds to (12.7 ± 11) nm and increases only slightly to (14.7 ± 13.6) nm for the more densely packed structure. These lengths were evaluated for domains with packed chains, ignoring the relatively short chain segments in more defective areas (cf. Fig. B.1).

The observed formation of organometallic structures agrees with previous studies of various brominated precursors on Ag, consistently reporting organometallic intermediates upon partial debromination at room temperature.[42,43,118,154] Yet, an intriguing aspect here is the remote site-selective didebromination exclusively at the

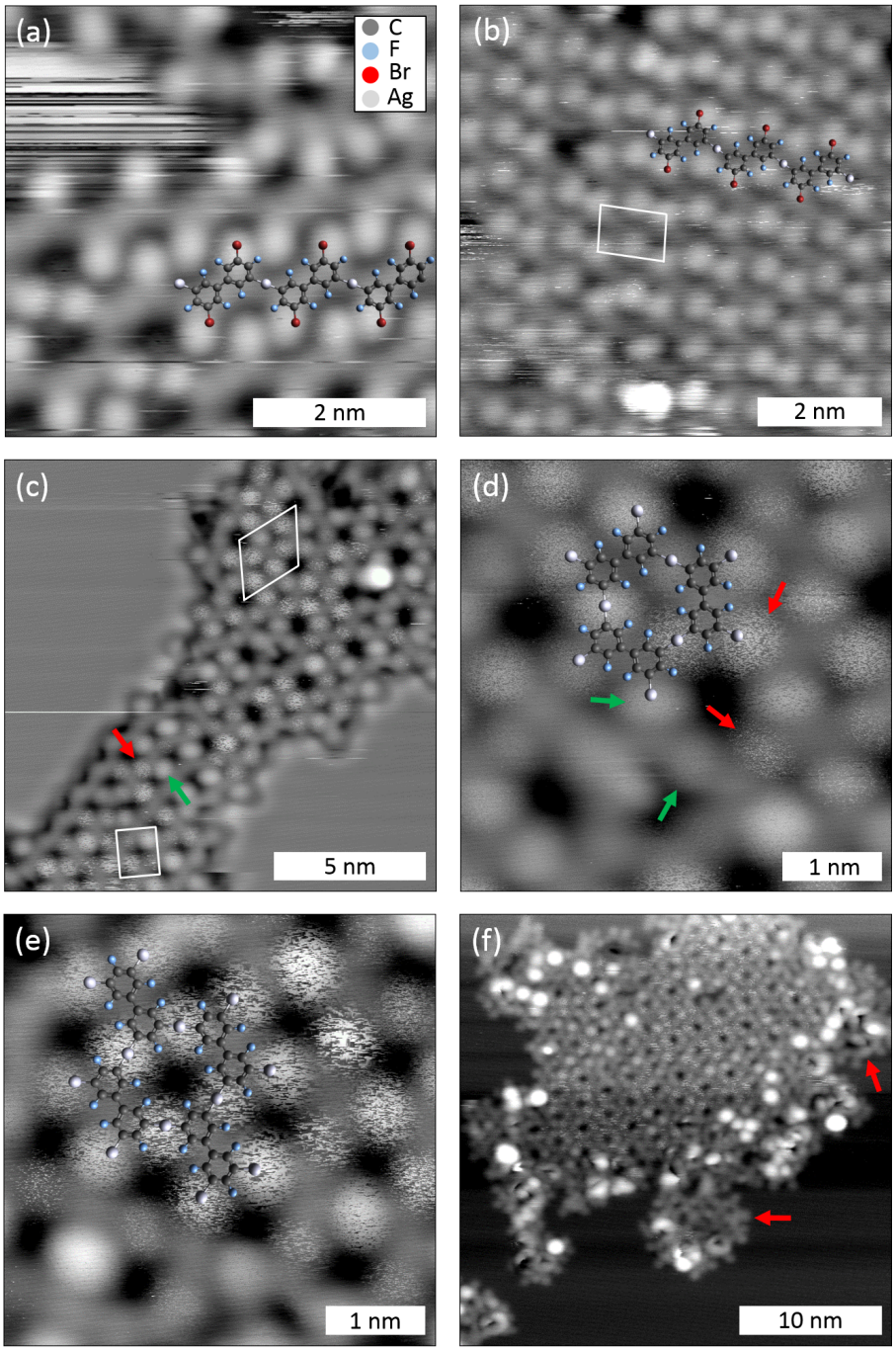

Figure 5.2: STM images acquired (a) / (b) after RT deposition of Br_4F_6BP on Ag(111), and subsequent annealing to (c)-(e) 200 °C and (f) 300 °C. After RT deposition (a) more loosely and (b) densely packed ordered arrangements of organometallic chains were observed. Annealing to 200 °C resulted in coexisting organometallic flower ((c) overview, (d) close-up) and (e) checkerboard structures; (f) the flower structure persisted even after annealing to 300 °C. Unit cells are indicated by white lines ((a), (c)). Tunneling parameters: (a) 44 pA, -0.69 V; (b) 22 pA, 1.26 V; (c) 45 pA, 0.58 V; (d) 45 pA, 0.58 V; (e) 42 pA, 0.60 V; (f) 92 pA, 0.53 V. Voltage polarities refer to the tip.

3- and 5'-positions, as required for chain formation. To unveil structural details of the chains and also to explain the STM contrast, isolated chains were simulated either with enforced planar geometry or alternatively by constraining all Ag atoms to similar height. The latter conditions result in significant tilting of the phenyl rings in the biphenyl unit with a dihedral angle of ∼49° and a slightly reduced repeat distance of 0.986 nm. Based on a comparison of the experimental STM images with the relatively pronounced contrast at the remaining bromine substituents and respective STM image simulations, better agreement with the STM images in Fig. 5.2(a) and (b) is achieved for tilted than for planar chains (cf. Fig. B.9). Yet, the structure of adsorbed chains might become decisively modified through interactions with the surface. Therefore, additional DFT simulations were carried out including the Ag(111) surface (cf. Fig. B.10). Among the stable structures two perfectly matching candidates were identified. Both structures feature a repeat distance of 1.05 nm along the chain, and interchain spacings of 0.77 nm and 1.05 nm, in accord with the experimental values of (0.78 ± 0.08) nm and (1.03 ± 0.10) nm for the more loosely and densely packed structures, respectively. Even in the presence of the surface, the biphenyl units remain significantly tilted, with large dihedral angles of ∼58° and ∼43° for the more densely and loosely packed structures. Consequently, the remaining bromine substituents also appear with a pronounced contrast in the corresponding STM image simulations (cf. Fig B.10).

The proposed 3,5'-didebromination after room temperature deposition is also corroborated by the corresponding Br 3d X-ray Photoelectron (XP) spectrum in Fig. 5.3(b) showing two chemically shifted Br species, each appearing as a spin-orbit doublet. The species with a higher Br $3d_{5/2}$ binding energy (E_B) of 70.2 eV corresponds to carbon-bound Br on the molecule,[118] whereas the species at a lower E_B of 68.1 eV indicates surface-bound, i.e. dissociated bromine.[42,43] Fitting the spectra results in a peak area ratio of ∼65% molecule-bound and ∼35% dissociated bromine. For perfect infinite chains, a debromination ratio of 50% is expected. Hence, the lower experimental value may indicate relatively short chains or other type of defects.

The strong evidence for organometallic linkages from STM is further corroborated by the C 1s XP spectrum in Fig. 5.3(a). As a guideline for the fitting of this rather complex C 1s spectrum with contributions from carbon atoms in various different chemical environments, core-level shifts were calculated for isolated species by DFT. The simulations were carried out on each symmetry-inequivalent carbon atom one at a time. All structures considered are depicted in Fig. 5.4, and the calculated

core-level shifts are summarized in Table 5.1, where intact precursors are also included for comparison. Irrespective of the exact configuration, the following common features of the core-level shifts are identified: as anticipated, the fluorine-substituted carbons (C-F) exhibit the highest C 1s E_Bs in accord with literature.[155,156] Additional small relative shifts can occur at the non-equivalent positions. In contrast, the organometallic carbon atoms directly bound to Ag (C-Ag) always appear at the lowest E_B. Interestingly, the relative order of C 1s E_Bs of the 1/1' carbons (C-C) at the linkage of the two phenyl units and bromine-substituted (C-Br) carbons depends on the degree of debromination and the geometric structure.

For a fully brominated and planar Br_4F_6BP monomer the C-Br E_B is slightly higher than that of C-C as intuitively expected, whereas for a non-planar geometry the order is reversed with a significantly enhanced E_B for C-C. In the half brominated and half organometallic compound, the E_Bs of C-C and C-Br are essentially similar for both planar structures, whereas for the non-planar structure C- features a lower E_B.

These simulation results in combination with additional information from Br 3d aided in fitting the C 1s peak: 35% debromination implies on average 2.4 remaining bromine substituents per molecule. Accordingly, the C-Br (with 2.4 such carbons per molecule) intensity is higher than that for the C-C species (with two such carbons per molecule). For the computationally somewhat undecided E_B order of the not separately resolved C-C and C-Br species, NEXAFS provided additional information: the chemically distinct carbon species are also reflected as fine structure in the π^*-resonance, normally even with higher sensitivity for the chemical environment of an atom than in XP Spectroscopy.[98] The strongest resonance at the highest photon energy is related to C-F with the highest C 1s E_B, whereas the adjacent resonance at lower photon energies has the second strongest intensity. Hence, the C-Br E_B is higher than that of C-C in agreement with the DFT results, in particular for the non-planar structure in Fig. 5.4(e). For fitting the XP spectra, two C-F species with slightly different E_Bs were considered as also suggested by the simulations. This additional information results in a good fit for C 1s as shown in Fig. 5.3(a) with relative amounts of 43% (50%) C-F, 25% (21.5%) C-Br, 20% (16.7%) C-C, 12.5% (12.5%) C-Ag. The values in parenthesis correspond to the percentages expected for 65% brominated sites and full conversion of 35% into organometallic sites after debromination.

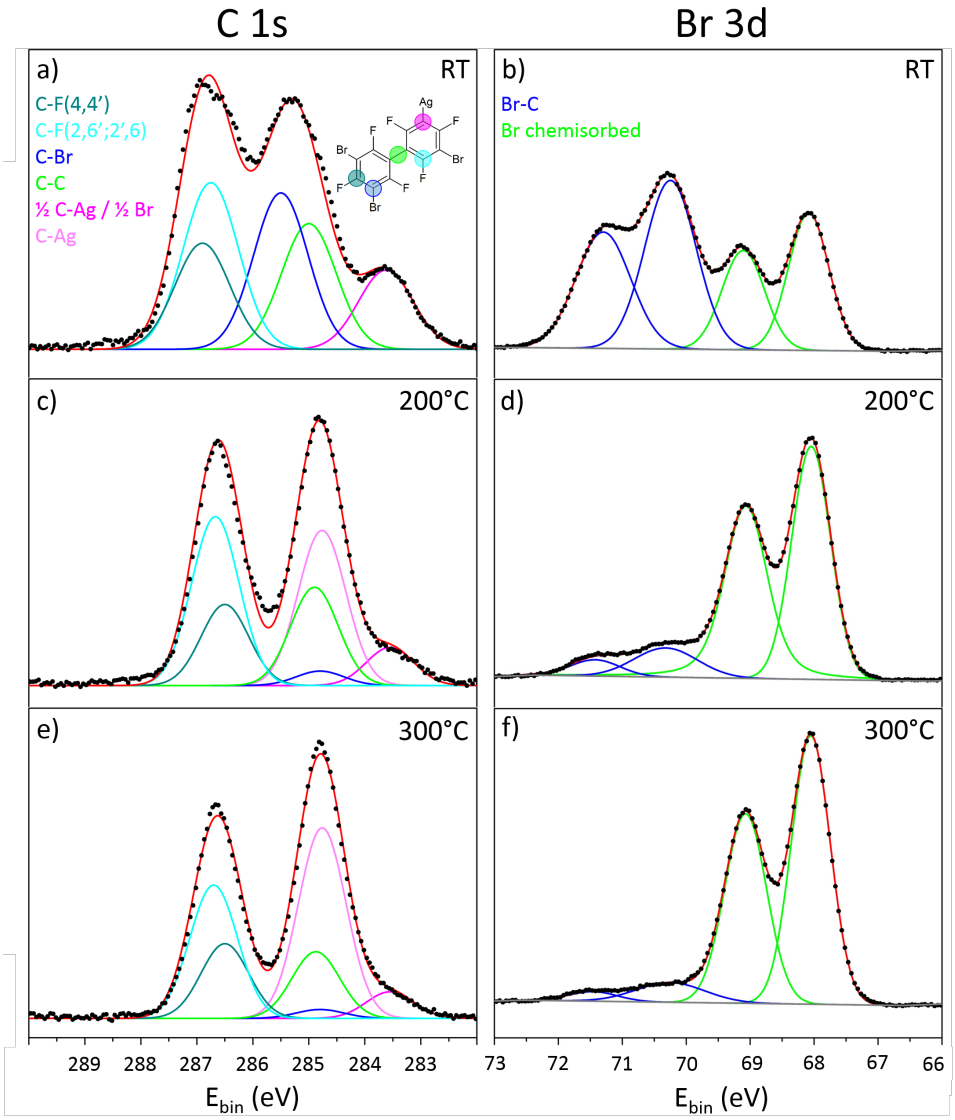

Figure 5.3: XP spectra of C 1s (left column) and Br 3d (right column) acquired after RT deposition of Br_4F_6BP (upper row) and subsequent annealing at 200 °C (middle row) and 300 °C (lower row). Raw data are represented by dots; solid lines show fits with Gaussian line shape and linear background. C 1s fits are assigned to following colour scheme: C-F(4,4'), dark cyan; C-F(2,6';2',6), light blue; C-Br, blue; C-C, green; C-Ag in half brominated and half organometallic phenyl rings, magenta; C-Ag in fully organometallic phenyl rings, light pink; Br 3d fits are presented for Br-C in blue and chemisorbed Br in green; red lines correspond to the sum of all components.

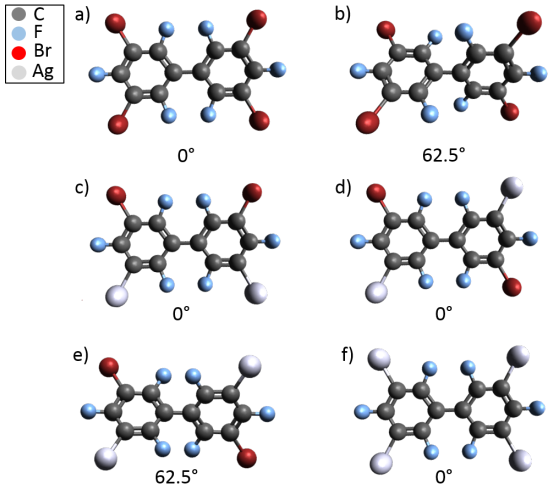

Figure 5.4: Chemically distinct structures considered in the C 1s core-level shift simulations (the dihedral angles are indicated below): (a) fully brominated, planar; (b) fully brominated, non-planar with a dihedral angle of 62.5°; (c) 50% debrominated, 50% organometallic, cis, planar; (d) 50% debrominated, 50% organometallic, trans, planar; (e) 50% debrominated, 50% organometallic, trans, non-planar with a dihedral angle of 62.5°; (f) fully debrominated and organometallic, planar.

	(a)	(b)	(c)	(d)	(e)	(f)
C-F (4,4')	-0.07	0.00	-0.29	-0.30	-0.08	-0.26
C-F (2,2')	0.00*	-0.14*	-0.23	-0.24	-0.25	0.00*
C-F (6,6')	0.00*	-0.14*	0.00	0.00	0.00	0.00*
C-Br	-1.25	-1.22	-1.31	-1.31	-1.15	-
C-C	-1.18	-1.91	-1.29	-1.30	-1.90	-1.15
C-Ag	-	-	-2.77	-2.79	-2.59	-2.54

Table 5.1: Calculated relative core-level shifts of C 1s in eV for the structures shown in Fig. 5.4. The carbon atom with the highest binding energy was used as reference. Core-level shifts are only given for one phenyl ring, the core-level shifts in the other phenyl ring are symmetry related.

To acquire quantitative information on the phenyl tilt angles, carbon K-edge NEXAFS experiments were performed. The spectra acquired after room temperature deposition of Br_4F_6BP onto Ag(111) for five different incidence angles are depicted in Fig. 5.5(a). All spectra show strong C 1s $\longrightarrow$ π^*-resonances for photon energies below 290 eV as expected for aromatic compounds.[104–106,124] The fine structure consists of four resolved peaks, nicely reflecting the chemical shifts of carbon. The strongest peak at the highest photon energy of 287.7 eV corresponds to C-F with the highest C 1s E_B. These results are in accord with NEXAFS spectra of a perfluorinated oligo(p-phenylene).[157] The π^*-resonances exhibit a pronounced dichroism, indicating a highly uniform orientation of all molecules on the surface. A detailed analysis of the dependence of the intensity of the resonance corresponding to the phenyl-phenyl carbons on the incidence angle results in an average orientation of the transition dipole moment of (45° ± 5°) with respect to the surface (cf. Fig. 5.5(b)). Direct interpretation as phenyl tilt angle is not indicated, as this value appears unrealistically high. DFT simulations of the organometallic chains adsorbed on Ag(111) suggest notably smaller tilt angles, i.e. half of the dihedral angle in the biphenyl unit for a symmetric adsorption geometry, of 29° (densely packed) and 22° (loosely packed) with respect to the surface. This discrepancy could be related to more subtle effects that result in apparent tilt angles, for instance hybridization of molecular with surface electronic states or upward bending of the fluorine substituents.[158] Additionally, complications for the direct interpretation of NEXAFS data can arise from core-hole localization and π^* delocalization effects in the biphenyl.[159] Perspectively, it is important to explore whether higher level NEXAFS simulations with explicit evaluation of transition dipole moments and consideration of the underlying surface result in quantitative agreement.

After sample annealing to 200 °C subsequent STM imaging revealed the coexistence of two different regular 2D networks: a flower (Fig. 5.2(d)) and a checkerboard structure (Fig. 5.2(e)) with hexagonal (a = b = (1.84 ± 0.18) nm) and centered rectangular unit cell (a = (1.57 ± 0.08) nm, b = (1.30 ± 0.10) nm), respectively. In particular the flower structure exhibits a high defect density and more disordered areas or vacancies were also discerned, mainly at phase boundaries. Both ordered structures are identified as organometallic networks with C-Ag-C interlinks between fully debrominated molecules. Accordingly, the checkerboard structure features two molecules per unit cell, whereas in the flower structure each unit cell accommodates three 120° rotated molecules resulting in a structure with p6mm symmetry. Scaled

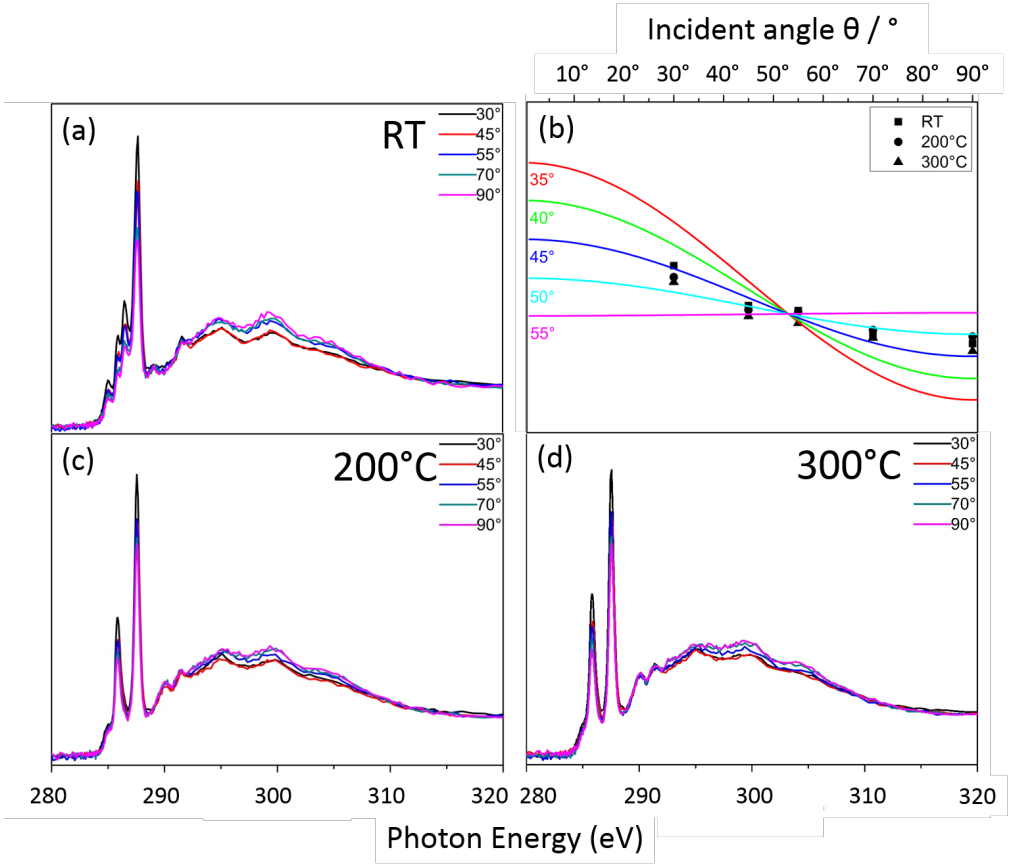

Figure 5.5: Carbon K-edge NEXAFS spectra of Br_4F_6BP on Ag(111) acquired for five different incidence angles after (a) RT deposition and subsequent annealing to (c) 200 °C and (d) 300 °C. All spectra were energy- and flux-corrected, background-subtracted, and normalized. Incidence angles θ refer to the surface, i.e. 90° corresponds to normal incidence. (b) Shows intensity vs. incidence angle θ plots for the resonance corresponding at a photon energy at 285.9 eV; the coloured solid lines are theoretical curves for the stated tilt of the transition dipole moment with respect to the surface normal, evaluated for the known X-ray polarization of P = 0.92.

overlays with DFT-optimized geometries perfectly match with the STM data. Accordingly, the experimental lattice parameters are consistent with optimized unit cell parameters from periodic DFT simulations with enforced planar geometry, yielding a = b = 1.86 nm for the flower, and a = 1.61 nm, b = 1.22 nm for the checkerboard structure, respectively. Moreover, the pronounced STM contrast of the Ag atoms in the organometallic linkages as similarly observed in comparable networks on Ag(111),[42,43] is well reproduced in STM image simulations based on the corresponding structures (cf. Fig. B.11). Complementary experiments with 4-fold decreased heating and cooling rates (1.5 °C min^{-1} instead of 5.8 °C min^{-1}) yielded similar results (cf. Fig. B.3). Interestingly, comparable long-range ordered organometallic structures were not observed for the topologically similar 3,5,3",5"-tetrabromo-para-terphenyl precursor on Cu(111).[160] A conceivable reason could be a diminished bond reversibility of the C-Cu-C linkages due to the higher organometallic bond strength.

Formation of fully cross-linked organometallic networks is triggered by progressive debromination, as also corroborated by Br 3d XP spectra indicating 86% debromination after annealing to 200 °C. Although the chemical state of the adsorbed molecules did not change markedly, the corresponding C 1s XP spectrum in Fig. 5.3(c) shows drastic alterations. It consists of two clearly separated main peaks, where the lowest E_B peak features an additional low E_B shoulder. Based on the STM results, the following assignment is proposed: the highest E_B peak still corresponds to C-F. The small shoulder at the lowest E_B could still be assigned to C-Ag, however, this leaves the question about the origin of the second main peak at a E_B of 284.8 eV (Fig. 5.3(c)). STM unambiguously shows the formation of organometallic networks, which should also be reflected in XPS as increasing C-Ag intensity. To resolve this discrepancy, we propose that the second main component in C 1s can be assigned to C-Ag in fully debrominated phenyl rings within the organometallic networks (Fig. 5.3(c), ∼284.8 eV, light pink). This implies that the chemical shift of C-Ag in the networks is ∼1.24 eV smaller than that in the organometallic chains observed after room temperature deposition. This hypothesis is corroborated in the core-level shift simulations: in the half-brominated half-organometallic phenyl rings that mimic the chains, C-Ag is shifted by -2.79 eV with respect to the highest E_B C-F, whereas the C-Ag shift decreases to -2.54 eV in the fully organometallic phenyl rings as in the 2D networks. Accordingly, we propose that the C-Ag shift depends on the number of organometallic bonds in the phenyl rings, with a significantly smaller E_B for phenyl rings with two organometallic bonds (chains) than with four organometallic

bonds (flower and checkerboard). Even though absolute values cannot be accurately reproduced by the model calculations, the trend is fully confirmed. Nevertheless, the strongest justification of our interpretation originates from the STM data, unambiguously showing organometallic networks. This interpretation is further supported by Br 3d XPS: 14% Br remained molecule-bound even after annealing to 200 °C. Assuming that all remaining Br are situated at the slightly tilted phenyl rings in the chains with one organometallic bond, this should result in 3% of the corresponding C 1s intensity, in reasonable agreement with a value of 7% from the fit. We note that this interpretation of the XPS data would not have been possible without STM data and C 1s core level shift simulations: the chemical shift of the C-Ag species observed after annealing to 200 °C in the fully organometallically linked phenyl rings towards typical values for carbon-bound carbon could easily have been misinterpreted as formation of fully covalent networks.

Further annealing to 300 °C resulted in disappearance of the checkerboard and prevalence of the flower structure as shown by the STM image in Fig. 5.2(f). This suggests that the flower structure is thermodynamically more stable, whereas the polymorphism observed for lower annealing temperatures of 200 °C can be attributed to kinetic effects. Even though the domain sizes increased considerably, the flower structure still exhibits a relatively high defect density. In addition, STM showed the emergence of more disordered not further resolved structures, mostly at the boundary of the remaining flower structure (Fig. 5.2(f) examples marked by red arrow). In XPS C 1s (Fig. 5.3(e)) appeared largely similar to the spectrum seen after annealing to 200 °C, only with a slight change of the intensity ratio at the expense of the C-F component. Moreover, the degree of debromination increases slightly to 91%, i.e. a safely detectable proportion of Br still remained molecule-bound (Fig. 5.3(f)), whereas the total amount of Br on the surface did not change.

Further NEXAFS experiments were also carried out after annealing to 200 °C and 300 °C, respectively. The spectra depicted in Fig. 5.5(c) and (d) appear largely similar for both annealing temperatures. In contrast to the room temperature spectra, the shape of the π^*-resonances changed from one main peak with fine structure to two peaks with comparable intensity, mirroring the changes also observed in C 1s XPS. Again an unrealistically large apparent phenyl tilt angle of ($50° \pm 5°$) is deduced from the intensity dependence. This is at odds with the STM results, since in the 2D networks, the biphenyl units are constrained to a planar geometry by the four intermolecular organometallic bonds. As already discussed above, a straightforward

interpretation of NEXAFS data assuming the transition dipole moment perpendicular to the phenyl ring is not indicated here.

Ordered organometallic networks could not be observed anymore after annealing at 400 °C. STM showed only disordered structures, where molecular units could not be discerned anymore (cf. Fig. B.2(c) / (d)). In XPS the C 1s intensity remained constant, whereas F 1s decreased to about 75%, indicating the onset of defluorination (cf. Fig. B.6). A possible X-ray radiation damage of the fluorine functional groups appears unlikely, as an additional experiment with a 60% reduced dose showed similar results. Moreover, the total intensity of Br 3d on the surface decreased to 34% of the initial amount due to thermal desorption. The constant amount of carbon on the surface excludes sizable desorption of monomers. For such a relatively small molecule, stabilization on the surface at these high temperatures can only be achieved by forming larger aggregates, suggesting formation of covalent intermolecular bonds. However, the lack of molecular resolution in STM may indicate more disordered structures without defined interlinks.

5.4 Discussion

Partial debromination followed by the formation of organometallic bonds is commonly observed for comparable brominated precursors on Ag(111) around room temperature.[42,43] In this respect, the perfluorination as in Br_4F_6BP does not lead to significant changes. This is fully consistent with the expectations from our DFT-derived homolytic bond dissociation energies of C-Br bonds in the gas phase, resulting in a similar value of 4.4 eV for both Br_4F_6BP and its non-fluorinated analogue. A spectacular observation is the formation of regular 1D chains through remote site-selective didebromination at the 3- and 5'-positions. Yet, this unprecedented phenomenon can be rationalized by the interplay of bond formation between radicals and adatoms and electrostatically mediated intramolecular conformational mechanics: the first debromination occurs at a random site (referred to as 3), directly followed by formation of an organometallic bond with an Ag adatom. The relatively large difference of adsorption heights between Ag adatoms (0.236 nm in three-fold hollow sites according to the (111) lattice plane spacing or 0.244 nm according to our DFT simulations of organometallic chains) and aromatic backbones (0.316 nm for perfluoropentacene on Ag(111)[161] or 0.323 nm according to our DFT simulations of organometallic chains) tilts the first phenyl ring toward this organometallic bond. Accordingly, the adsorption height and consequently the debromination barrier of the Br at the 5-position

increase, resulting in kinetic stabilization. The remote site-selective debromination at the second phenyl ring in 5'-position is mediated by the steric repulsion through the ortho-fluorine atoms, leading to a large dihedral angle between the two phenyl rings. This conformational tilt of the second phenyl ring in the opposite direction gives rise to a low adsorption height and debromination barrier at the 5'-position and kinetic stabilization of the Br at the 3'-position. In essence, the steric repulsion conveys the remote site-selective debromination across two phenyl rings. However, substantial differences in efficiency of this process were observed between different experimental runs: for the results shown in Fig. 5.2(b) overview images indicate a very high yield with almost no defects; this high regularity also enables the more dense packing of the chains; in contrast, for the results shown in Fig. 5.2(a) a markedly reduced selectivity of ∼60% was deduced from statistical analysis of STM data (cf. Fig. B.4). Accordingly, a more subtle influence from additional preparation parameters such as deposition rate and surface temperature during deposition appears likely. To shed more light on the conformational mechanics, comparative STM experiments were carried out with the nonfluorinated analogue Br_4BP. In analogy to Br_4F_6BP, room temperature deposition of Br_4BP onto Ag(111) likewise results in the formation of 1D organometallic chains (cf. Fig. B.7(a) / (b)). These results unambiguously demonstrate that even the weaker steric repulsion of the ortho-hydrogens is sufficient to mediate a site-selective 3,5'-didebromination through conformational mechanics. Interestingly, deposition of Br_4BP onto Ag(111) held at 50 °C induces high defect densities, also related to progressive dissociation of the remaining bromine substituents (cf. B.7(c) / (d)). These additional experiments demonstrate that for Br_4BP the conformational mechanics is not very robust against higher thermal energy, hence only works in a relatively small temperature window.

The formation of organometallic networks from multiply brominated precursors on Ag(111) driven by the thermally activated progression of debromination is well documented.[42,43,162] In this sense, Br_4F_6BP-derived networks are a further example for "organometallic self-assembly", confirming the mandatory bond reversibility of C-Ag-C linkages. Yet, the observed polymorphism is quite uncommon for organometallic self-assembly. For Br_4F_6BP as precursor, the two experimentally observed regular structures correspond to the two least complex structures conceivable for these two-fold symmetric tectons and straight C-Ag-C linkages. Interestingly, all Ag atoms in the organometallic networks exhibit comparable apparent heights in STM, prohibiting any tilt within the biphenyl backbone. Given the large steric

repulsion due to the ortho-fluorine atoms, co-planar adsorption appears surprising. On the other hand, DFT indicates a relatively modest energy cost of 1.32 eV for planarization of the Br_4F_6BP in the gas phase in accord with literature values.[163] The planarization is accompanied by a lengthening of the phenyl-phenyl bond from 0.1481 nm to 0.1544 nm to alleviate the electrostatic repulsion.

Even though STM indicates a largely similar adsorption height of all organometallic Ag atoms, closer inspection reveals more subtle differences: some Ag atoms appear rather noisy, whereas others could be stably imaged (examples are marked by red and green arrows, respectively, in Fig. 5.2(c) / (d)), ruling out tip instabilities. The distribution is not random: stable Ag atoms appear predominantly at domain boundaries and defects, whereas within the domains the majority of Ag atoms appear noisy (cf. Fig. B.5). This peculiar difference is attributed to a weakening of the surface contacts for noisy Ag atoms as a consequence of constraining the intrinsically twisted biphenyl molecules to planarity by their integration within the networks. Again, it is instructive to compare the 2D organometallic self-assembly of Br_4F_6BP and Br_4BP triggered by full debromination. In contrast to the fluorinated precursor, the non-fluorinated precursor exclusively forms the checkerboard pattern without any indications of polymorphism or the flower structure that was even the thermodynamically more stable polymorph for Br_4F_6BP (cf. Fig. B.8(a) / (b)). Moreover, the corresponding domain sizes remain comparatively small for Br_4BP. Even though apparently related to the perfluorination, the origin of these differences is not yet clear. A possible explanation is offered by differences in surface mobility, where the inherently non-planar structure of the Br_4F_6BP precursor should give rise to a higher diffusivity. In addition, for Br_4BP large areas of the surface were covered with densely packed domains of dissociated Br (cf. Fig. B.8), imposing serious constraints on the formation of organic networks.[51] Yet, it remains unclear as to why this halogen poisoning is more pronounced for the nonfluorinated precursor.

A further very remarkable feature of the organometallic networks derived from Br_4F_6BP is their exceptional and unprecedented thermal stability up to 300 °C. In contrast, the Br_4BP derived organometallic intermediates are converted into covalent networks upon annealing to ∼200 °C (cf. Fig. B.8(c) / (d)), in accord with hexagonal polyphenylene networks.[27,43,113] The extraordinary thermal stability of the Br_4F_6BP derived organometallic flower structure indicates high binding energies that could in principle arise either from strong molecule-molecule or strong molecule-surface interactions. However, a comparative X-ray standing wave study finds a significant

enlargement of the adsorption height for perfluorinated pentacene on Ag(111), indicating a weakening of the molecule-surface interactions.[164] This suggests that the high stability of the organometallic networks here originates from strong molecule-molecule interactions as indeed rationalized by gas phase DFT simulations: planar organometallic dimers with one linear C-Ag-C linkage and three remaining Br substituents per biphenyl result in bond dissociation energies of 1.93 eV for the perfluorinated vs. 1.34 eV for the hydrogen-terminated dimer. Even though actual values may differ for the adsorbed system, perfluorination accounts for the extraordinary stability of the organometallic networks by increasing the C-Ag-C bond strength. By the same token, the higher bond strength restricts the reversibility, hence increases the temperatures required for structural equilibration. This may also account for both the relatively high defect densities in the organometallic networks and the relatively high temperatures required for conversion of the metastable checkerboard into the more stable flower structure.

In contrast to other organometallic networks,[42,43,165] and in particular to the comparable 3,5,3",5"-tetrabromo-para-terphenyl precursor[160] and the non-fluorinated Br_4BP analogue, a thermally activated conversion into defined covalent networks was not observed here, not even for the highest annealing temperature of 300 °C. This is tentatively attributed to the combination of extraordinary stability of the organometallic networks, an additional barrier for covalent coupling due to the ortho-fluorine atoms, but also the onset of molecule degradation by defluorination at higher annealing temperatures (cf. Fig. B.2(c) / (d)).

5.5 Conclusion

In summary, Br_4F_6BP showed a rich combination of known and unprecedented surface chemistry on Ag(111) as summarized in Fig. 5.1: while formation and equilibration of organometallic structures is meanwhile well established, the formation of defined 1D organometallic chains for both the fourfold brominated perfluorinated Br_4F_6BP and non-fluorinated Br_4BP precursor is unique. This chain formation involves the regioselective activation of only two out of the precursor's four active sites. This is explained by a remote site-selective 3,5'-didebromination, mediated across the biphenyl unit by its conformational non-planarity due to the intramolecular repulsion of either the ortho-fluorine or ortho-hydrogen substituents. This constitutes an instructive and highly useful example of conformational mechanics in on-surface synthesis: formation of chemical bonds with the surface upon activation of specific

sites of a molecular entity is accompanied by an increase of adsorption height, and hence deactivation at the opposing sites. The proposed symmetry breaking mechanism has broader implications for on-surface synthesis as it provides a rationale for the observed stepwise or uncommonly gradual and selective activation in apparently symmetric monomers.[42,43] In this respect, it is intriguing that already the significantly weaker steric hindrance in the non-fluorinated Br_4BP precursor is sufficient to drive this conformational mechanics.

In contrast, both the polymorphism and the exceptional stability of organometallic networks are unique observations for the Br_4F_6BP precursor. As indicated by our DFT simulations, the perfluorination can be held responsible for the high stability of the organometallic networks. Even though it decreases the adsorption energy of aromatic molecules on metals, by the same token the strength of intermolecular C-Ag-C linkages is markedly enhanced. The exceptional strength of the intermolecular organometallic bonds is even sufficient to overcome the large electrostatic repulsion within the molecules and incorporate them in into extended 2D networks. Yet, the role of the perfluorination for the polymorphism remains unclear. Tentatively, either the enhanced surface mobility of Br_4F_6BP due to the non-planar structure or the large amounts of adsorbed bromine for Br_4BP could be held responsible and would also be consistent with the larger domain sizes observed for Br_4F_6BP as compared to Br_4BP.

Interestingly, as already indicated by DFT-derived C-Br bond dissociation energies, there is no pronounced effect of the perfluorination on the debromination barrier, as debromination temperatures are within the typical range reported for non-fluorinated precursors.[42,43] Accordingly, in terms of activation, perfluorinated monomers are equally suitable for debrominative coupling on surfaces. Yet, covalent coupling into defined structures as templated by the organometallic flower structure remains elusive for Br_4F_6BP on Ag(111). This is an important finding as it provides valuable guidelines for the design of fluorinated monomers suitable for covalent aryl-aryl coupling, for instance by combining ortho-fluorine with orthohydrogen substitution. Alternatively, the substantially increased intermolecular bond strength in the organometallic networks derived from perfluorinated precursors provides a perspective for directly using the highly stable organometallic 2D polymers for improved structural quality.

5.6 Materials and methods

All STM, NEXAFS, and XPS experiments were carried out under ultrahigh vacuum (UHV) conditions with base pressures below 3×10^{-10} mbar (STM) and 8×10^{-10} mbar (XPS, NEXAFS). Ag(111) single crystals surfaces were prepared by cycles of 0.5 keV-Ar^+ sputtering and annealing at 500 °C. 3,3',5,5'-tetrabromo-2,2',4,4',6,6'-hexafluorobiphenyl (Br_4F_6BP) was synthesized according to literature procedures[166,167] and deposited by sublimation from a home-built Knudsen-cell with crucible temperatures between 55 °C and 80 °C at a pressure of 3×10^{-9} mbar.[91] The non-fluorinated analogue 3,3',5,5'-tetrabromo-1,1'-biphenyl (Br_4BP) was purchased from Sigma Aldrich ($\leq$100% purity). Its vapour pressure at room temperature is high enough to facilitate deposition from a Knudsen-cell without additionally heating the crucible. STM data were recorded at room temperature with a home-built microscope controlled by an SPM100 controller (RHK Technology Inc.). NEXAFS and XPS measurements were carried out in a Prevac endstation at the HE-SGM beamline at Helmholtz-Zentrum Berlin. NEXAFS carbon K-edge spectra were acquired in the analysis chamber using a home-built double channel plaste detector in partial electron yield mode (U = -150 V). XP spectra of C 1s, Br 3d, and F 1s were measured with a Scienta R3000 electron analyzer at normal electron emission with a pass energy of 50 eV. Photon energies of 450 eV for C 1s and Br 3d and 750 eV for F 1s were used, respectively. For energy calibration a Ag $3d_{5/2}$ binding energy of 368.2 eV was used as internal standard.[135] Dispersion-corrected DFT simulations were performed either with periodic boundary conditions (organometallic chains, flower and checkerboard structure) or for isolated molecules (C 1s core-level shifts) with the FHI-aims computing package.[168] Geometry optimizations for the unit cells containing one (organometallic chains and checkerboard structure) or three (flower structure) molecules with two (organometallic chains) and four (checkerboard and flower structure) Br atoms exchanged for Ag were performed with FHI-aims at "tight" computational settings, $4 \times 4 \times 1$ k-point sampling, and using a 30 Å vacuum region. In these calculations electronic exchange and correlation (xc) was treated on the generalized-gradient approximation level with the PBE functional,[138] augmented by dispersive interactions through the Tkatchenko-Scheffler TSsurf method.[169] All structures were fully relaxed until residual forces were below 10 meV $Å^{-1}$. The adsorbed organometallic chains were optimized on Ag(111) slabs with 11 and 15 atoms per layer. A lattice parameter of a_{Ag} = 4.152 Å was used and the first of two layers were allowed to relax. The influence of the weakly interacting Ag(111) surface was neglected in the simulations

of the 2D flower and checkerboard structures, but the unit cell size was optimized together with the geometry. STM image simulations were performed based on the DFT-optimized structures according to the Tersoff-Hamann approach.[88] Therefore, all electronic states in an energy window defined by the bias voltage and the Fermi energy were summed to produce the final image. C 1s core level energies were calculated with a 1s core-hole on each symmetry-inequivalent carbon atom one at a time. The maximum overlap method was used to prevent variational collapse to the ground state.[170,171]

6 Competitive metal-coordination of hexaaminotriphenylene on Cu(111) by intrinsic copper versus extrinsic nickel adatoms

The final experimental section presents the exemplary results for a surface-mediated metal-organic polymerization reaction of hexaaminotriphenylene with intrinsic Cu and extrinsic Ni adatoms on Cu(111). The study is submitted to Chem. Eur. J., WILEY-VCH Verlag GmbH & Co. KGaA, Weinheim, as: M. Lischka, R. Dong, M. Wang, N. Martsinovich, M. Fritton, L. Grossmann, W. M. Heckl, X. Feng and M. Lackinger: Competitive metal-coordination of hexaaminotriphenylene on Cu(111) by intrinsic copper versus extrinsic nickel adatoms.

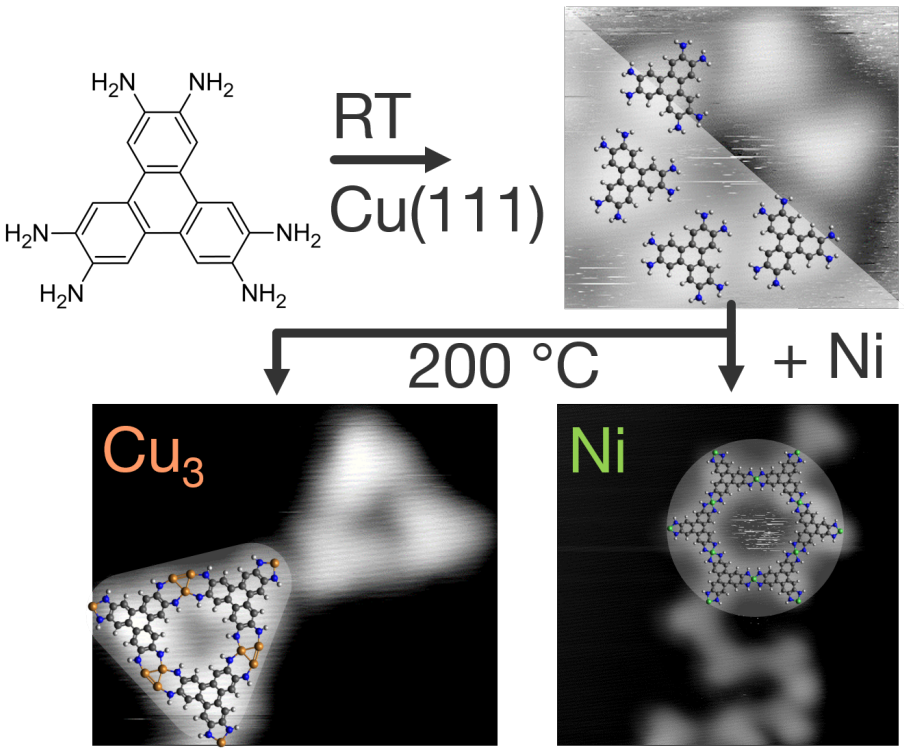

I performed all the experiments and the corresponding data analysis and interpretation, and prepared the manuscript under supervision of Prof. Lackinger. The co-authors M. Fritton and L. Grossmann gave support during STM and XPS measurements, respectively. The precursor was synthesized by M. Wang under the supervision of Dr. R. Dong and Prof. X. Feng. DFT calculations were performed by Dr. N. Martsinovich.

6.1 Abstract

The interplay between self-assembly and surface chemistry of 2,3,6,7,10,11-hexaaminotriphenylene (HATP) on Cu(111) was complementarily studied by high-resolution Scanning Tunneling Microscopy and X-ray Photoelectron Spectroscopy under ultra-high vacuum conditions. To shed light on competitive metal-coordination, comparative experiments were carried out on pristine and nickel-covered Cu(111). Directly after room temperature deposition of HATP onto pristine Cu(111) self-assembled aggregates were observed by STM, while XPS indicated non-deprotonated amino groups. Annealing up to 200 °C activated the progressive single deprotonation of all amino groups as indicated by chemical shifts of both N 1s and C 1s core levels in the XP spectra. This enabled the formation of topologically diverse π-d conjugated coordination networks with intrinsic copper adatoms. The basic motif of these networks was a metal-organic trimer, where three HATP molecules were coordinated by Cu_3 clusters, as corroborated by accompanying Density Functional Theory simulations. Additional deposition of more reactive nickel atoms resulted in both chemical and structural changes with deprotonation and formation of bis(diimino)-Ni bonded networks already at room temperature. Even though fused hexagonal pores were observed, extended honeycomb networks remained elusive, as tentatively explained by a restricted reversibility of these metal-organic bonds.

6.2 Introduction

The bottom-up synthesis of two-dimensional (2D) materials with regular structures and tailored properties is a long-standing goal in chemistry and material science.[19,109,142] A pivotal milestone was the materialization of 2D coordination nanosheets (CONASH), where multitopic organic ligands are cross-linked into regular networks by metal-coordination bonds. The synthesis of square-centimeter large self-supporting sheets was pioneered at the air-water interface, and has subsequently also been demonstrated at the interface between two immiscible liquids.[18,172–174] For the latter, typically multilayers are achieved. For these interface-assisted synthetic approaches triphenylene-based organic ligands with six-fold hydroxyl, thiol, or amino functionalization at the 2,3,6,7,10,11 positions evolved as important model system.[175–180] The targeted binding motif is a planar four-fold coordination complex, and incorporation of Cu, Ni, and Co coordination centers yielded isostructural π-d conjugated CONASHs with honeycomb structure and widely tunable properties.[181] Superior electrical conductiv-

ities up to 103 S cm^{-1} were demonstrated, facilitating a variety of applications as electrode materials for organic field-effect transistor, chemiresistive sensing,[17] electrocatalytic hydrogen evolution reaction as well as oxygen reduction,[175,182] and supercapacitors.[177,178,183]

Despite the tremendous progress in the interface-assisted synthesis of large area CONASH, a molecular level structural characterization by high-resolution microscopy remains challenging. Even though recent advances were achieved for single-layer CONASH with high-resolution transmission electron microscopy,[184] the high electron beam sensitivity of these materials imposes severe limitations. On the contrary, submolecular features are routinely resolved by Scanning Tunneling Microscopy both on metal-coordination and covalent networks with minimal risk of sample damage. Yet, for networks grown at liquid interfaces, STM characterization requires a post-synthetic transfer to suitable solid surfaces, with only a few reported cases of successful imaging.[185] The reasons for the difficulties in ex-situ imaging of these networks are not entirely clear, but might be related to an unavoidable waviness after their transfer to solid surfaces, crucially impairing high resolution STM imaging. In contrast, both metal-coordination and covalent networks that were directly grown on solid surfaces under ultra-high vacuum or even under ambient conditions are routinely imaged with high resolution.[107,186,187] Albeit requiring UHV is not desirable in terms of a low-cost fabrication, fundamental studies can benefit greatly from these utmost defined conditions. For instance, a thorough chemical characterization by X-ray Photoelectron Spectroscopy of in-situ prepared samples is not affected by contaminations that are unavoidable under ambient conditions.

In the present study we focus on 2,3,6,7,10,11-hexaaminotriphenylene (HATP, cf. Fig. 6.1). Despite the large body of work on nitrogen-containing metal-coordination networks with amines,[26] nitriles,[70,72,188,189] pyridines,[71] or amino-quinone-imines,[64,65] HATP or other ligands with ortho-disubstituted amino groups have not been investigated on solid surfaces so far. The only example of a related compound intended the on-surface synthesis of pyrene-fused pyrazaacenes via Schiff-base reaction.[190] To shed more light on the metal-coordination of this important molecular building block on solid surfaces, we present a detailed study of competitive HATP metal-coordination on Cu(111) between intrinsic Cu adatoms of the surface[26,64] and co-deposited extrinsic Ni adatoms. This choice is motivated by a strong interest in comparing coordination centers with different binding strength and ground state electron configurations. The utilized combination of STM, XPS, and DFT provides the base for drawing solid

and important conclusions on the interplay between surface chemistry and structure formation.

6.3 Results and discussion

HATP on pristine Cu(111)

First experiments were conducted on pristine Cu(111). The STM images in Figure 6.1(a) and (b) acquired directly after room temperate deposition of HATP reveal self-assembled molecular aggregates. Cyclic hexamers are most abundant, but incomplete and fused hexamers as well as more densely packed structures were similarly observed. Individual HATP molecules and their respective orientation can be discerned by means of the triangular footprints of the planar adsorbed triphenylene cores. In the hexamers all HATP molecules point toward the center and share edges that are not fully aligned, but slightly offset. To unveil the stabilizing intermolecular bonds in these hexamers, acquiring complementary information on the chemical state of HATP is indispensable. In this respect, it is important to address the question of a possible deprotonation of the amino groups already after room temperature deposition onto Cu(111).[9,26] Therefore, XP spectra were acquired from N 1s and C 1s core levels, whereby the spectra of 3 - 4 layer thick films shown in Figures 6.2(a) and (b) served as references for chemically unaltered HATP molecules. The sharp N 1s peak indicates a single chemical species, corroborating the anticipated chemical equivalency of all nitrogen atoms. The measured binding energy (E_B) of 399.8 eV is in accord with NH_2 groups on aromatic moieties, with similar E_Bs reported for aniline,[191,192] 1,3-phenyldiamine,[193] tetraamine,[190] and melamine[194] adsorbed on various metals surfaces. The C 1s XP spectrum shown in Figure 6.2(b) required fitting with two chemically shifted components with E_Bs of 284.7eV and 285.7 eV, resulting in a peak area ratio of 67 : 33. The C 1s component at higher E_B corresponds to the amino-substituted carbons, the component at lower E_B corresponds to the unsubstituted carbons of the triphenylene core.[191,195,196] Hence, the deduced ratio perfectly reflects the HATP stoichiometry.

The submonolayer spectra presented in Figures 6.2(c) and (d) are essentially similar to the multilayer. Only N 1s exhibits a slight shift of ∼0.39 eV towards higher E_B. Yet, core-hole screening and deprotonation would both result in shifts to lower E_B, and can hence be excluded.[64,65,99,100,191,194,197,198] There are no notable shifts in C 1s, indicating a specific surface-influence on the nitrogen atoms, such as for in-

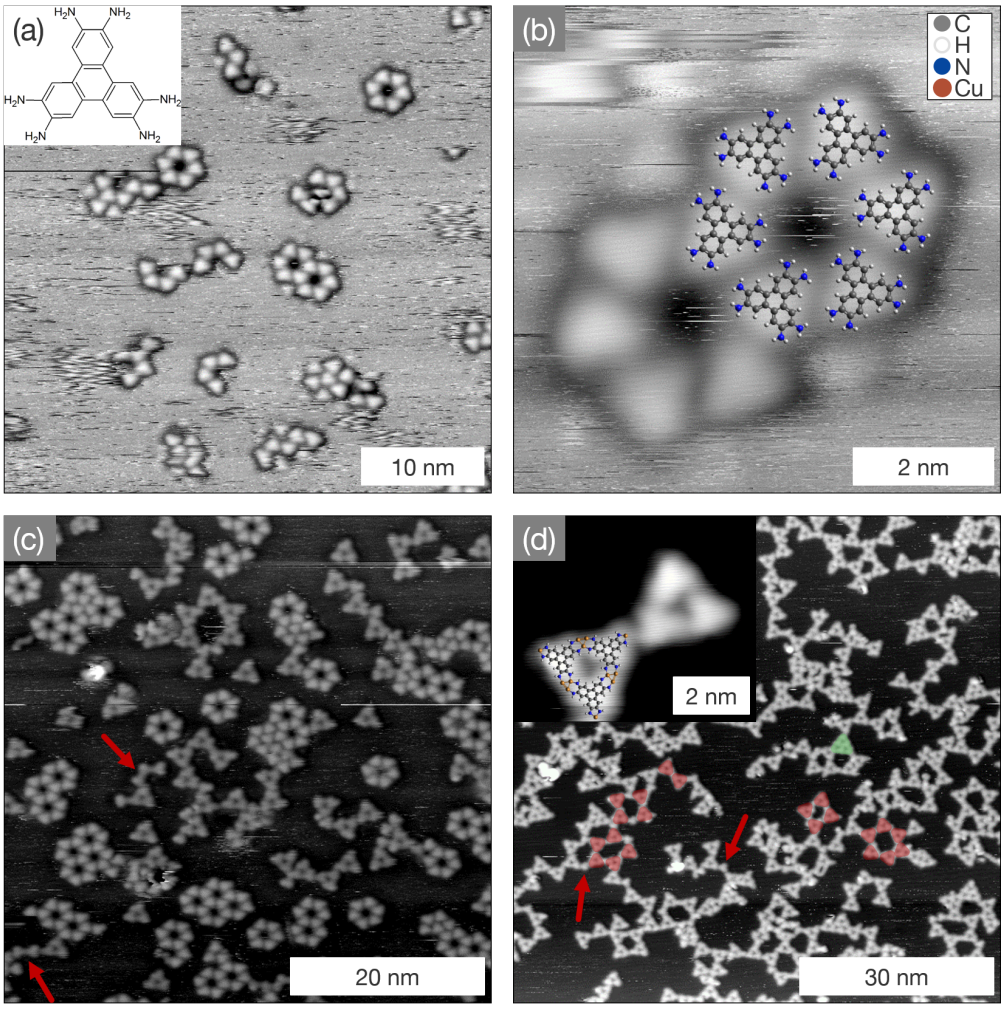

Figure 6.1: STM images acquired after (a) / (b) room temperature deposition of HATP onto Cu(111) and subsequent annealing to (c) 100 °C (red arrows highlight straight dimers) and (d) 200 °C (red arrows highlight single HATP molecules interlinking trimers). The inset in (a) shows the chemical structure of HATP; DFT-optimized structures were used for the overlays. (tunneling parameters: (a) 0.73 V, 54 pA; (b) 0.73 V, 51 pA; (c) 0.89 V, 59 pA; (d) 0.87 V, 90 pA; (d, inset) 0.33 V, 20 pA)

stance formation of N-Cu bonds. In summary, XPS indicates adsorption of HATP molecules with intact NH_2 groups after room temperature deposition onto Cu(111), in accord with results obtained for a comparable compound.[199] To address the question as to what interactions drive the self-assembly of these aggregates, DFT simulations of both single HATP molecules and cyclic hexamers on Cu(111) were conducted. Various starting geometries consistently resulted in adsorption geometries, where the centers of all aromatic rings of the triphenylene backbone resided above three-fold hollow sites (either fcc- or hcp-sites). Accordingly, half of the carbon atoms also resided on three-fold hollow sites, and the remaining carbon atoms on top-sites of the Cu(111) surface. This preferred adsorption geometry is well known for benzene on transition metals,[200,201] and the match between the spacing of the aromatic rings in triphenylene (0.250 nm) and the Cu(111) lattice parameter (0.255 nm) makes this adsorption geometry also favorable for the larger aromatic core of HATP. Several models for the HATP hexamers on the Cu(111) surface were calculated using DFT; the experimentally found arrangement and intermolecular distances were reproduced by all calculated models within the experimental error (cf. Fig. C.6 and Table C.1). Figure 6.3(a) exemplarily shows one structure, where all aromatic rings reside above fcc-sites, which were consistently found to be 0.02 - 0.03 eV per molecule more favorable than hcp-sites. The DFT-derived center-to-center distance of two diametrically opposed HATP molecules of 2.41 nm is in good agreement with the experimental value of (2.52 $\pm$ 0.06) nm. In this particular structure half of the nitrogen atoms reside on top of copper atoms, additionally allowing N-Cu bond formation. While DFT indicates a rather strong adsorption of HATP on Cu(111) with adsorption energies around 4 eV per molecule, the intermolecular interactions in the hexamers are surprisingly weak, on the order of 0.06 - 0.18 eV per molecule. The disintegration of aggregates followed in subsequent STM images provides experimental evidence for a weak stabilization (cf. Fig. C.2). Even though amino groups could in principle act as hydrogen-bond acceptors through their nitrogen lone pair, the present DFT simulations do not provide any evidence for intermolecular hydrogen bonds. Consequently, we conclude that solely van-der-Waals interactions account for the cohesion of these aggregates.

To activate deprotonation as a prerequisite for the formation of metal-coordination bonds, samples were first annealed at 100 °C. The subsequently acquired STM image in Figure 6.1(c) shows the emergence of new cyclic triangular entities, but also the persistence of the original hexamers with unchanged dimensions. Occasionally,

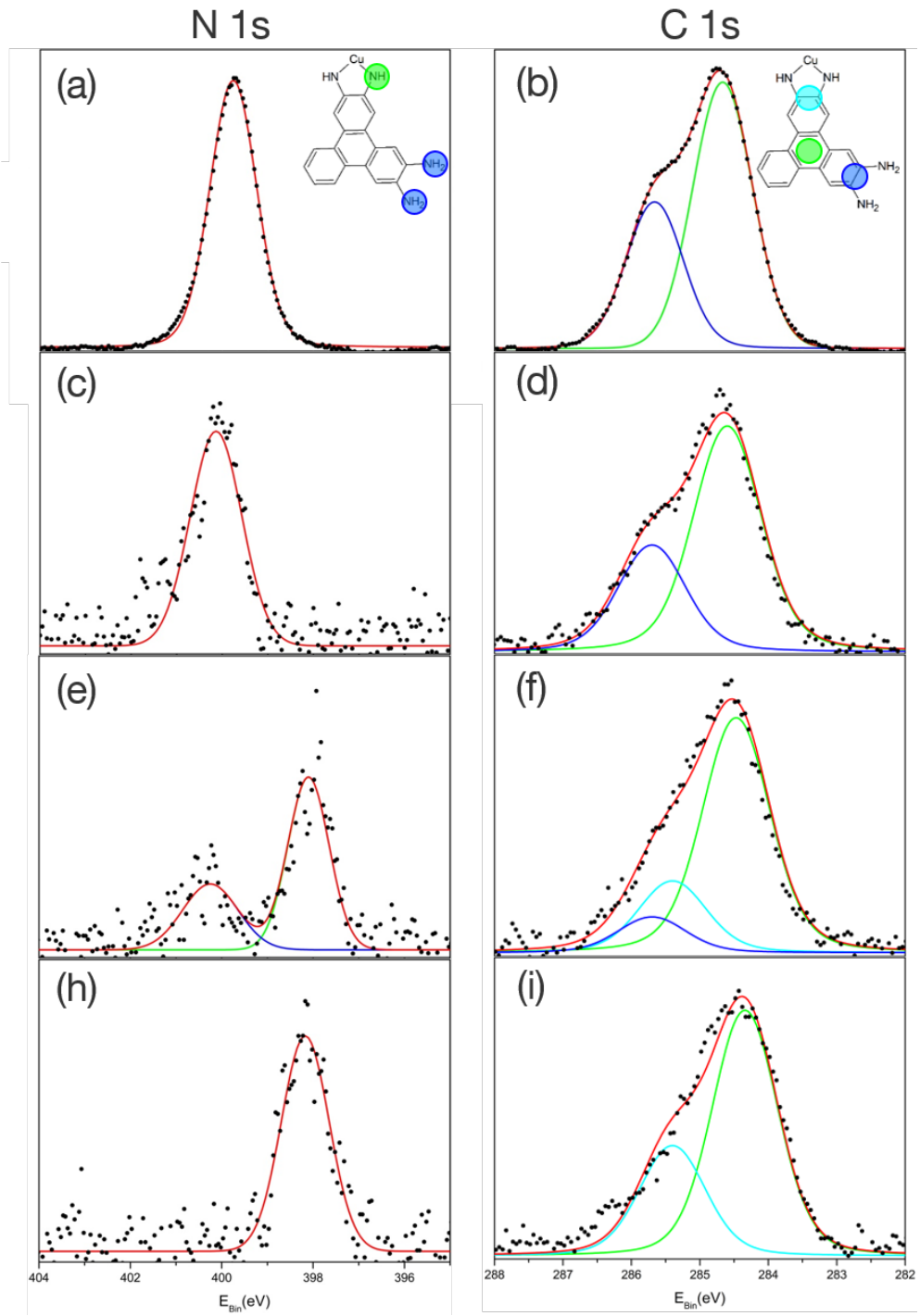

Figure 6.2: XP spectra of N 1s (left column) and C 1s (right column) acquired for HATP on Cu(111): (a) / (b) multilayer; (c) / (d) submonolayer after room temperature deposition and subsequent annealing to (e) / (f) 100 °C, and (h) / (i) 200 °C. Data are represented by black dots; red lines correspond to the sum of all fitted components; N 1s and C 1s components are assigned to the following colour scheme as also shown in the inset: NH_2 (green), NH-Cu (blue), C-C (green), C-NH_2 (blue), C-NH-Cu (light blue.)

straight interlinked dimers were also observed (examples marked by red arrows) with a center-to-center distance of (1.55 ± 0.08) nm. According to DFT calculations, the targeted bis(diimino)-Cu motif would result in a notably smaller center-to-center distance of 1.29 nm. However, a perfect match is obtained with a dimer, where molecules coordinate two copper atoms linearly arranged on the axis, resulting in a center-to-center distance of 1.54 nm (cf. Fig. C.7). The emergence of these new aggregates is also reflected in the XP spectra shown in Figures 6.2(e) and (f): N 1s is now split into two chemically shifted species, one at the original E_B with a relative peak area of 34% and a new majority component at a lower E_B of 398.1 eV with a relative peak area of 66%. The lower N 1s E_B is characteristic for singly deprotonated amino groups in metal-coordination bonds.[64,193,202] Distinct changes are similarly observed in C 1s, where the previously observed prominent high E_B shoulder appears less pronounced. A satisfying fit is obtained with three components, corresponding to unsubstituted carbons in the triphenylene backbone (C-C: 66%) and two different types of substituted carbons, either binding to fully protonated (C-NH_2: 11%) or singly deprotonated and metal-coordinated (C-NH-Cu: 22%) amino groups. The ratio between the latter two is consistent with the deprotonation ratio deduced from N 1s. Furthermore, C 1s exhibits a slight integral shift to a lower E_B of 284.5 eV for the main triphenylene peak. Annealing to 200 °C triggers progressive deprotonation and formation of metal-coordinated structures. As shown in Figures 6.2(h) and (i), the chemical changes in XPS previously observed after annealing at 100 °C are driven to completion: N 1s indicates full deprotonation, with only one main peak remaining at a lower E_B of 398.1 eV. Accordingly, C 1s again consists of two components, corresponding to carbons in the triphenylene core and carbons substituted with metal-coordinated amino groups, respectively. The deduced peak area ratio of 68 : 32 again reflects the HATP stoichiometry. The integral peak shift of C 1s to lower E_Bs is continued with a E_B of 284.3 eV, suggesting a correlation with the amount of metal-coordination sites on the molecules.[194] The total intensities of both N 1s and C 1s did not change notably during heating, indicating the absence of molecular desorption. The chemical changes observed in XPS are also accompanied by structural changes as illustrated in the STM image in Figure 6.1(d). Hexamers cannot be discerned anymore; instead, a large variety of different aggregates are observed with a triangular HATP trimer as the common basic unit. These trimers are interlinked into various configurations: (1) head-to-head; (2) cyclic rings consisting of four, five, or six trimers; in addition, individual HATP molecules can be identified either attached

at the periphery of larger aggregates either as interlink or termination, respective examples are marked by red arrows in Figure 6.1(d).

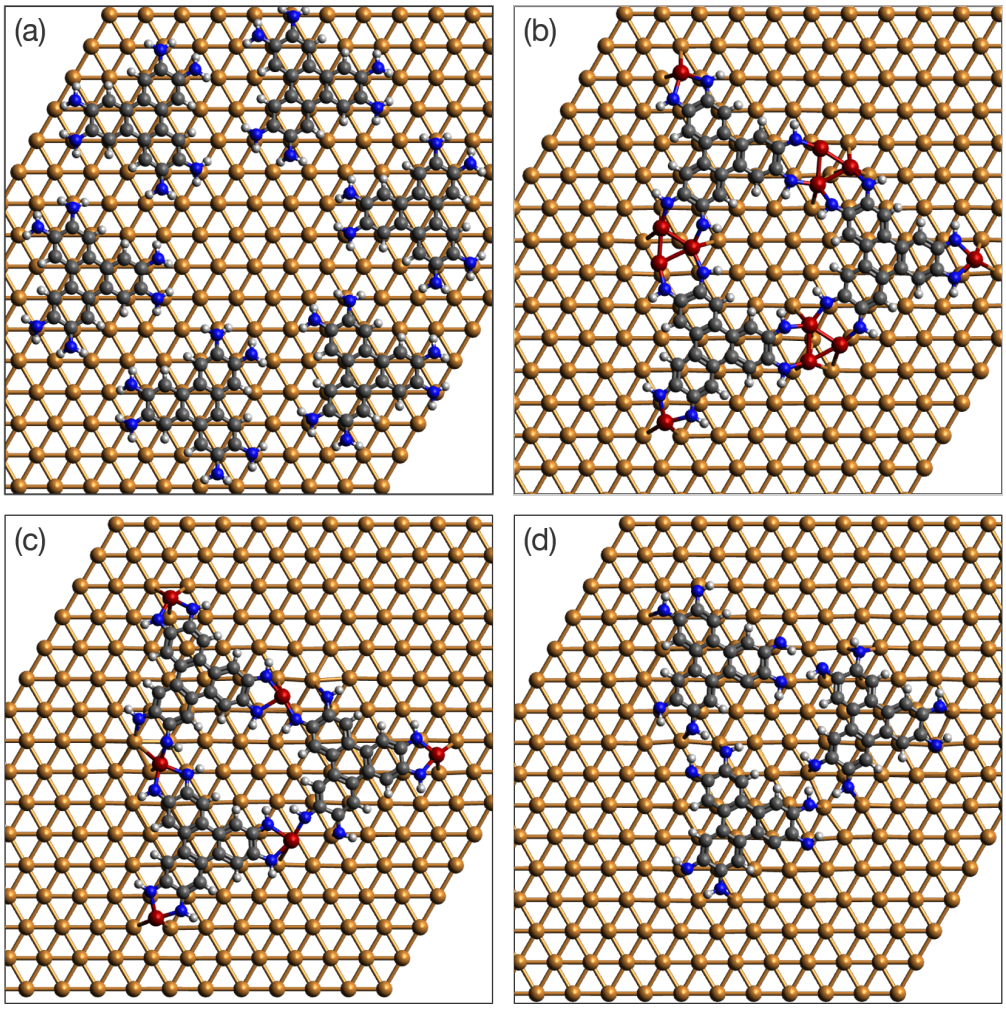

Figure 6.3: DFT-optimized geometries of HATP structures on Cu(111): (a) hexamer of fully protonated HATP; (b) trimer with Cu_3 coordination centers; (c) trimer with single Cu atom coordination centers; (d) imine based hydrogen bonded trimer. (only the topmost copper layer is shown, Cu adatoms are depicted in red)

For understanding the structural changes, it is pivotal to resolve the nature of the intermolecular interactions in the trimer. The threefold-symmetry in STM indicates equivalent orientations of all molecules in a trimer, whereas XPS suggests chemical equivalency and deprotonation of all amino groups. Based on this information, DFT simulations were carried out for two metal-coordinated models: either with single Cu atoms or Cu_3 clusters as coordination centers. Alternatively, an imine based hydrogen bonded trimer was considered. The DFT optimized structures of these trimer

models on Cu(111) are presented in Figures 6.3(b) - (d), with intermolecular distances of 1.34 nm, 1.31 nm, and 1.20 nm, for the Cu-, Cu_3-, and hydrogen bonded trimer, respectively. All of these intermolecular distances are consistent with the experimental value of (1.28 ± 0.03) nm within the experimental error. Yet, the best agreement is achieved with the Cu_3 coordination centers that were similarly proposed for tetrahydroxy benzene on Cu(111).[81] Additional support for the Cu_3 coordination centers comes from the XPS data: N 1s indicates a single chemical nitrogen species, whereas the trimer with single Cu atom coordination features nitrogen atoms in inequivalent chemical environments. This argument similarly applies to the hydrogen bonded trimer that contains two types of nitrogen species: hydrogen-bonded and free imine nitrogen atoms. In addition, the literature consistently reports copper-coordination of deprotonated amino groups on copper surfaces,[26,64,194] rendering the formation of this hydrogen bonded structure improbable. It is worth noting that N 1s XPS indicates deprotonation and copper coordination of all amino groups. Accordingly, copper coordination was also introduced at the peripheral amino groups of the metal-coordinated trimers, and could similarly explain the linking of the trimers into aggregates and networks. Additional experiments with three-fold reduced heating rates (0.50 °C min^{-1} instead of 1.66 °C min^{-1}) did not increase the network quality (cf. Fig. C.3). Neither did further annealing to 300 °C, where both STM and XPS studies consistently indicate molecular degradation: both a low E_B organometallic shoulder at C 1s and the diminished intensity of N 1s suggest dissociation of amino groups (cf. Fig. C.4 for STM images and Fig. C.5 for XP spectra).

HATP on Cu(111) + Ni

To achieve the formation of honeycomb networks based on the four-fold planar bis(diimino)-metal linkages, further experiments were conducted with additional Ni atoms on the surface. First, HATP was deposited onto Cu(111) held at room temperature, followed by co-deposition of Ni. The subsequently acquired STM image in Figure 6.4(a) unveils interlinking of molecules into hexagonal porous structures that resemble the targeted honeycomb network. Chemical changes are also corroborated by XPS shown in Figure 6.5: direct comparison of N 1s and C 1s spectra before and after Ni co-deposition clearly confirms a Ni-induced deprotonation of ∼50% of the amino groups. These give rise to a third component in C 1s, similar to the thermally activated deprotonation on pristine Cu(111). A good fit is achieved by applying the deprotonation ratio obtained from N 1s as a constraint for the relative ratios of the

C 1s components. These striking differences to the self-assembled hexamers observed on pristine Cu(111) after room temperature deposition can evidently be attributed to the presence of Ni, whereby the changes in XPS are similar to the thermally activated deprotonation on pristine Cu(111).

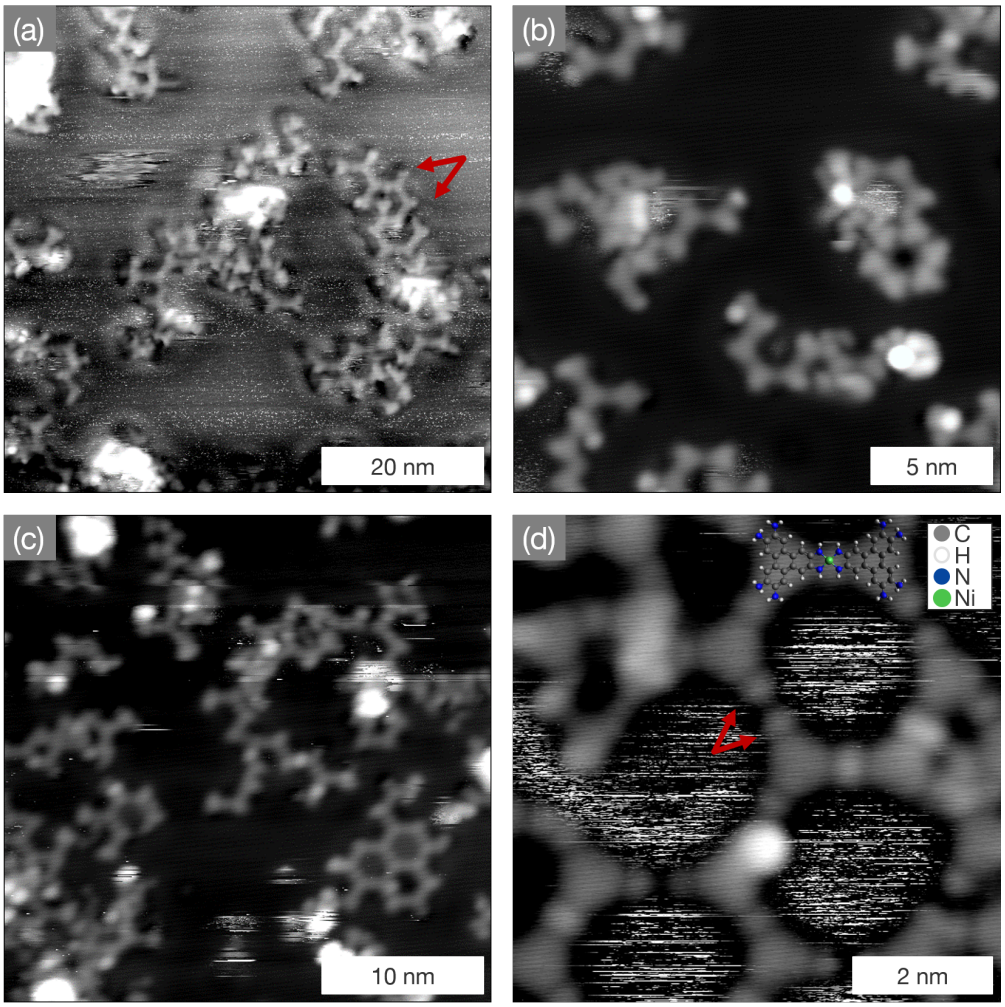

Figure 6.4: STM images acquired after deposition of HATP and Ni onto Cu(111) at (a) room temperature, and after annealing to (b) 100 °C, and (c) / (d) 200 °C; the red arrows highlight terminating Ni atoms (tunneling parameters: (a) 0.90 V, 87 pA; (b) 0.95 V, 92 pA; (c) 3.27 V, 91 pA; (d) 0.88 V, 93 pA)

To activate further deprotonation and network formation, the samples were subsequently annealed to 100 °C. XPS confirms the progressive deprotonation of now 72% of the amino groups directly in N 1s, and indirectly in C 1s by an increase of the metal-organic component, but also as an integral peak shift to a lower E_B of 284.4 eV. The not yet complete deprotonation is also reflected in STM by the occa-

sional observation of self-assembled hexamers. Yet, the STM image in Figure 6.4(b) does not show complete pores or networks. To drive deprotonation to completion, a second annealing step to 200 °C was performed, resulting in full deprotonation as confirmed by the N 1s and C 1s XP spectra presented in Figures 6.5(h) and (i): N 1s consist of a single peak at lower E_B and C 1s shows full development of the metal-organic component up to the stoichiometric ratio of 33 : 67 with a constant amount of carbon. The STM image in Figure 6.4(c) now shows network patches consisting of up to three hexagonal pores, but incomplete pores were still frequently observed. The high resolution image in Figure 6.4(d) clearly confirms formation of the expected bis(diimino)-Ni binding motif with head-to-head oriented molecules interlinked by a straight metal-coordination bond. Also the experimental center-to-center distance of (1.45 ± 0.04) nm is in accord with the DFT-derived value. Furthermore, a clear signature of the Ni coordination center can now be discerned in the STM contrast as opposed to Cu coordination centers that are often invisible to the STM.[64–66,72,78,203] Despite the possibility to form a similar bis(diimino)-Cu motif with intrinsic adatoms of the Cu(111) surface, the Ni motif is strongly preferred, presumably on energetic grounds: the binding energy in the bis(diimino)-Ni coordinated dimer with respect to isolated constituents is calculated to be -9.7 eV, while in the Cu-coordinated dimer it is only -6.0 eV. Interestingly, the termini of the incomplete pores show bright protrusions, indicating saturation with Ni atoms at the periphery (examples are marked by red arrows in Figure 6.4(d)). While further annealing to 260 °C did not improve the network quality, annealing at 300 °C resulted in disordered structures in STM, while XPS indicated molecular decomposition (cf. Fig. C.4 for STM images and Fig. C.5 for XP spectra).

To achieve the growth of extended and highly regular metal-coordination networks, the ratio of molecules to coordination centers is a further, potentially decisive parameter.[204,205] Therefore, additional experiments were carried out with lower (∼30%) and higher (∼4-fold) amounts of Ni, while the amount of molecules was kept constant. Similarly, HATP was deposited first onto Cu(111) held at room temperature, then Ni was co-deposited in the three different coverages, and finally, the samples were annealed to 200 °C. The STM image for "low" Ni coverage in Figure 6.6(a) shows two co-existing different metal-coordination motifs: the triangular structures as observed on pristine Cu(111) and the straight motifs as observed in the presence of Ni. This indicates that the amount of Ni was too small to suppress Cu coordination. For the previously applied Ni coverage the results are consistent,

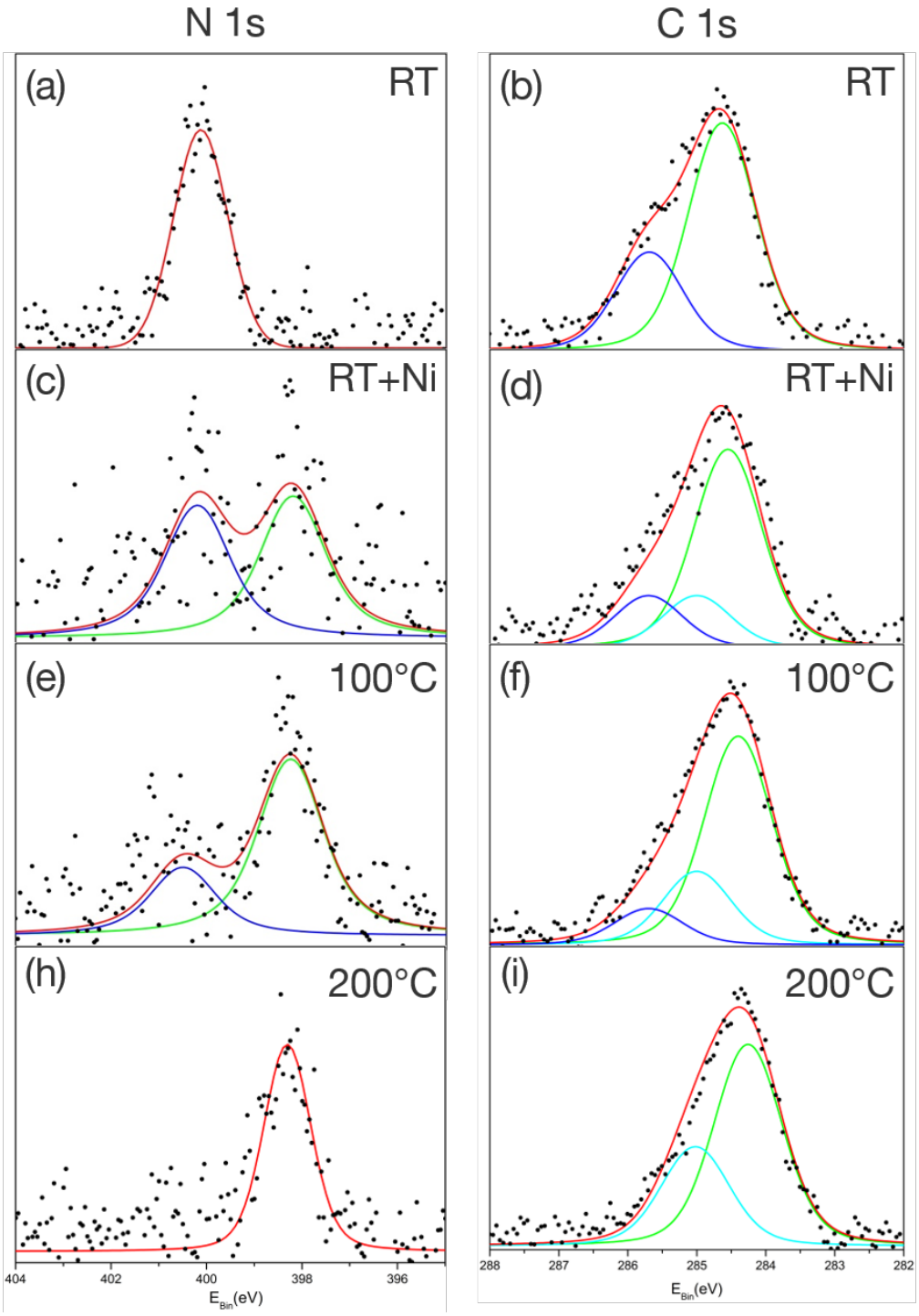

Figure 6.5: XP spectra of N 1s and C 1s core levels acquired after (a) / (b) room temperature deposition of HATP on Cu(111), (c) / (d), after additional deposition of Ni, and annealing to (e) / (f) 100 °C, and (h) / (i) 200 °C. Data is represented by black dots; red lines correspond to the sum of all fitted components; N 1s and C 1s components are assigned to the following colour scheme: NH_2 (green), NH-Ni (blue), C-C (green), C-NH_2 (blue), C-NH-Ni (light blue).

exclusively showing the bis(diimino)-Ni motif. At "high" Ni coverage the onset of cluster formation on the surface can be seen in Figure 6.6(c). Although exclusively the Ni coordination motif is observed, the size of metal-organic networks is markedly diminished.

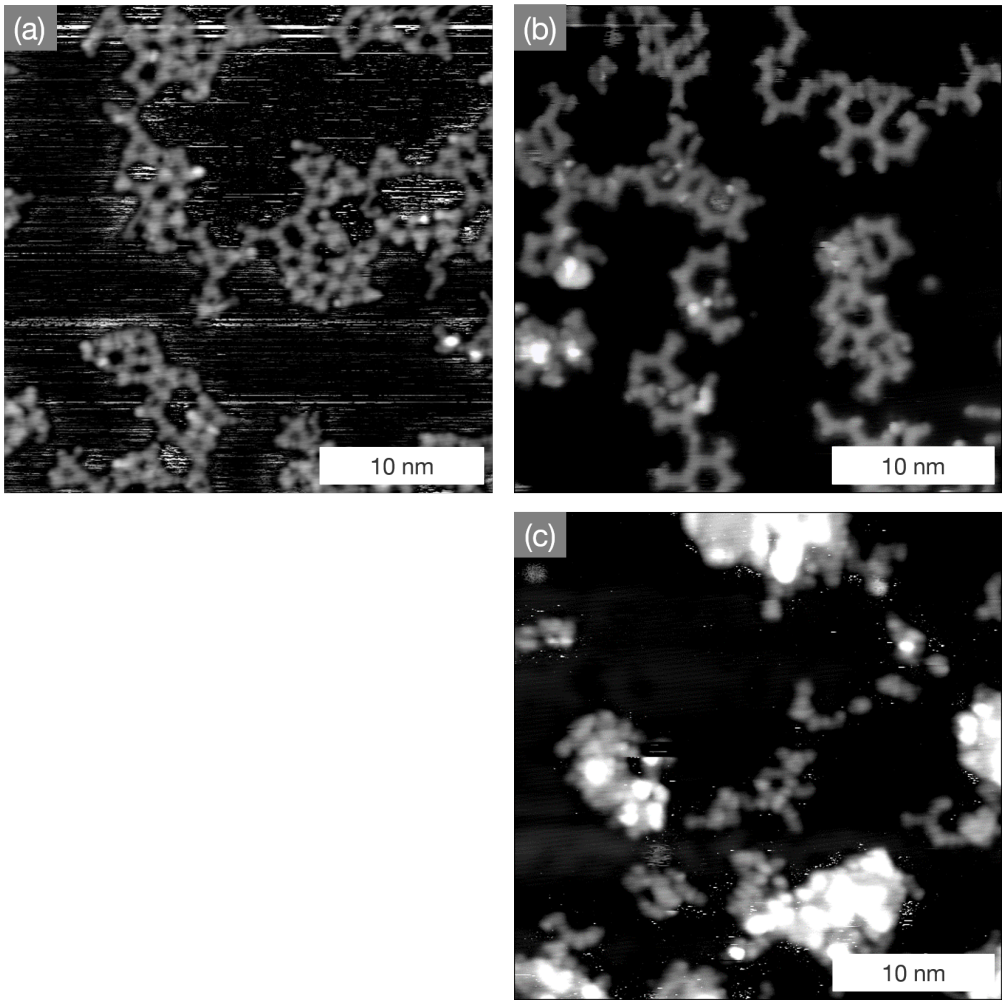

Figure 6.6: STM images of HATP on Cu(111) acquired after deposition of different amounts of Ni and subsequent annealing to 200 °C; (a) "low" Ni coverage (30%); (b) previously applied Ni coverage (100%); (c) "high" Ni coverage (400%) (tunneling parameters: (a) 0.88 V, 55 pA; (b) 1.80 V, 100 pA; (c) 3.20 V, 89 pA).

6.4 Conclusion

The observed structural and chemical changes of HATP on pristine and Ni-covered Cu(111) surfaces are summarized in Figure 6.7. HATP molecules remained chemically unaltered upon room temperature deposition onto pristine Cu(111). The ab-

sence of deprotonation of amino-functionalized compounds under these conditions is common,[26,64,199] whereas on more reactive Ni(111) surfaces partial deprotonation can readily occur.[191,193] Despite the fact that HATP molecules are not equipped for strong intermolecular bonds, stable self-assemblies could be imaged by STM at room temperature. According to DFT calculations, a strong and site-specific adsorption of the triphenylene core on Cu(111) largely accounts for the stabilization. Subsequent annealing triggered the well-known thermally activated deprotonation on pristine Cu(111).[26,64,199] This provided the basic prerequisite for formation of metal-coordination bonds, unexpectedly with Cu_3 clusters as coordination centers. Albeit single atom coordination motifs are most common on surfaces, a similar Cu_3 motif was previously proposed for tetrahydroxy benzene on Cu(111).[81] In this respect, it appears more surprising that the expected bis(diimino)-Cu motif was not observed on Cu(111), given its predominance at liquid interfaces.[17] This hints towards thermodynamic preference for the copper-rich Cu_3 coordination on Cu(111). Notwithstanding that this motif would in principle allow the extension into fully reticulated and regular 2D networks, only linked trimers were observed. A possible explanation is offered by pronounced adsorption-site preferences of both the triphenylene backbones and the Cu_3 clusters that cannot be met both at the same time in larger networks.

Co-deposition of more reactive Ni triggers deprotonation already at room temperature, clearly indicating adatom mediated surface chemistry. In the competition with metal-coordination by Cu adatoms, a distinct preference for Ni-coordination is expressed. Accordingly, insufficient amounts of Ni can be held responsible for the observed co-existence of Ni-coordination and Cu-coordination. Here we found 50% deprotonation after co-deposition of Ni at room temperature, whereas the thermally induced further deprotonation showed a temperature progression comparable to pristine Cu(111). This suggests a Cu-driven process without any further notable contributions from Ni. Even though small patches of the targeted honeycomb network were formed, extended regular structures remained elusive. This observation is attributed to a limited bond reversibility of the strong Ni coordination bonds, preventing the fusion of the smaller fragments into extended networks. The diminished size of molecular aggregates observed for larger amounts of Ni provides further experimental evidence for this hypothesis. This restricted bond reversibility is a decisive difference compared to the situation at liquid interfaces, where extended self-supporting networks can be obtained.[178] Consequently, the aqueous subphase must play a vitally important role for the reversibility of the metal-organic coordination bonds. Higher

temperatures, that could in principle induce bond reversibility also on Cu(111), are prohibitive, as this leads to molecular decomposition, presumably by dissociation of the amino groups.

In summary, studying the formation of metal-coordinated networks from HATP on Cu(111) under UHV conditions substantially benefits from the possibility of acquiring high-resolution STM images and complementary chemical information from XPS. Important differences to the synthesis at liquid interfaces become apparent: (1) the high availability of adatoms as coordination centers on solid metal surfaces promotes the expression of multi-atomic coordination motifs; (2) distinct adsorption-site preferences impose further constraints on crystalline surfaces that may hamper the formation of extended networks in the present case; (3) the absence of the liquid subphase substantially affects metal-organic bond formation, with possible consequences for bond reversibility.

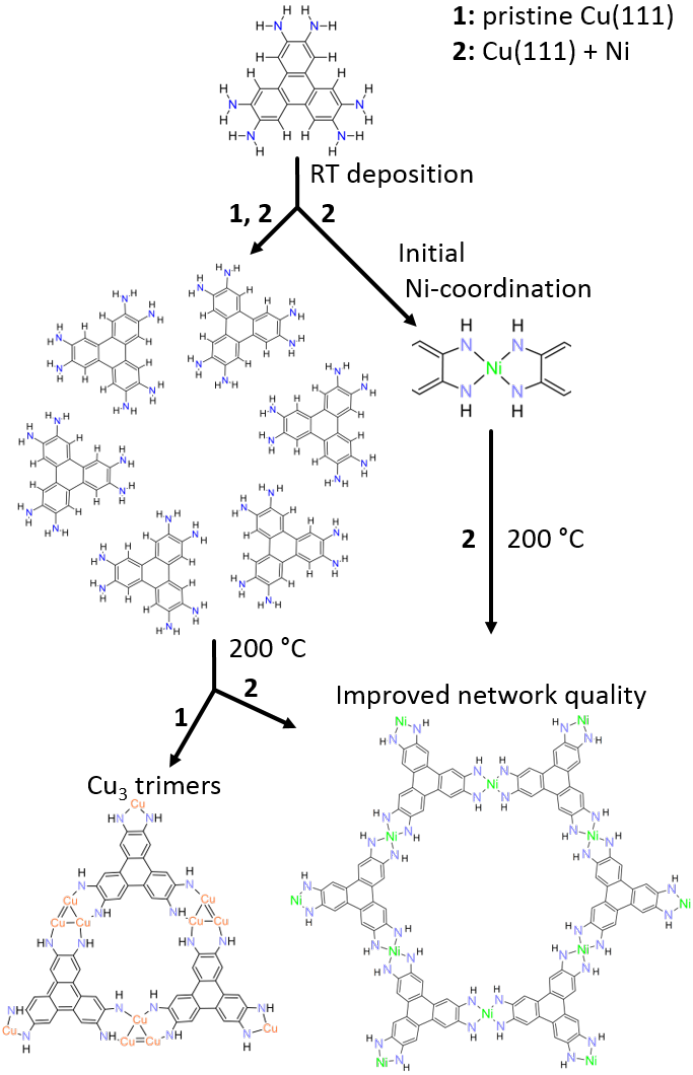

Figure 6.7: Summary of thermally and Ni-induced structural and chemical changes of HATP on pristine and Ni-covered Cu(111).

6.5 Materials and methods

STM and XPS experiments were carried out under UHV conditions at base pressures below 3×10^{-10} mbar. For STM (XPS) experiments Cu(111) single crystals were prepared by cycles of 0.5 (1.0) keV Ar^+-ion sputtering and radiative (e-beam) annealing at 500 °C. HATP was deposited by sublimation from a home-built Knudsen-cell[91] with a crucible temperature of 225 °C at a pressure of 3×10^{-9} mbar. Nickel (0.5 mm diameter wire, 99.99%, MaTecK) was deposited from an Omicron EFM 3 e-beam evaporator using a molybdenum crucible and deposition rates were controlled with the internal flux monitor. For all sample annealing steps a standard heating and cooling rate of 1.66 °C min^{-1} was applied, if not noted otherwise.

STM data were acquired in-situ at room temperature with a home-built instrument controlled by an SPM100 controller (RHK Technology Inc.). XPS measurements were carried out in a SPECS system equipped with a monochromatic XR50M X-ray source and Phoibos 150 electron analyzer. XP spectra were acquired using a Al-Kα source with a photon energy of 1486.3 eV at normal electron emission with a pass energy of 20 eV. For energy calibration a Cu $3p_{3/2}$ binding energy of 70.1 eV was used as internal standard.[206] XP spectra were fitted by Voigt-functions after subtraction of linear backgrounds. For a given element similar peak widths were applied for all chemically shifted components.

DFT simulations were carried out with the CP2K software.[207,208] The PBE functional was employed[138] with the D3 dispersion correction,[209] Goedecker-Teter-Hutter pseudopotentials,[210] and double-zeta valence polarized basis sets.[211] The Brillouin zone was sampled only at the Γ point. Isolated molecules and oligomers were modelled as non-periodic systems. The Cu(111) surface was modelled using two-layer thick 16×16-expanded periodic slabs; the bottom layer of the Cu slab was fixed, while the top layer and all adsorbates were allowed to relax.

7 Conclusion and outlook

The present thesis demonstrates systematical and detailed studies of on-surface synthesis using aromatic molecules for a bottom-up approach to fabricate 2D nanostructures on solid surfaces with the aim to realize defect-free and extended reticular networks under UHV conditions. Therefore, a complementary approach of STM, XPS, and NEXAFS, as surface-sensitive analysis tools was applied for in-situ structural, chemical, and electronic characterization of the nanostructures, as well as to monitor the reaction pathway during the surface-assisted polymerization. The experimental approach was supplemented by Density Functional Theory calculations provided by cooperation partners. Two well established on-surface polymerization and coupling reactions were further studied: (1) The surface-assisted Ullmann coupling and (2) the surface-mediated metal-organic coordination. Herein, previously[42,43,48,52] reported dependences on reaction parameters and factors that influence the formation of low dimensional structures and interlinking of molecular building blocks were confirmed: Different temperature thresholds for halogen cleavage during hierarchical polymerization of iodine and bromine functional groups on Au(111), respectively (Sec. 4.1), as well as the initial partial debromination of a precursor after RT deposition on Ag(111) (Sec. 4.4). In addition, the transformation by subsequent heating from intact precursors into organometallic intermediates or metal-organic coordinated structures (Sec. 5.3 and 6.3), was confirmed. Foremost, the unique and previously not considered influence factors, for instance fluorine substituents instead of hydrogen, were explored, including a discussion of the observed limitations and advantages of the complementary approach by STM, XPS and NEXAFS for the polymer characterization:

Surface-assisted Ullmann coupling

Steric hindrance vs. hierarchical polymerization - After RT deposition of the doubly brominated and iodinated pyrene derivate on Au(111) the commonly observed total iodine cleavage was not observed, only a partial I-C dissociation was detected. Further heating to 100 °C is necessary to form the expected 1D chains. However, direct covalent coupling is not achieved due to the steric repulsion by linking on the 1/1'-position. Instead, C-Au-C organometallic intermediates could be observed which is commonly reported for aryl-aryl coupling on Au surfaces for molecules with strong repulsive interactions.[46] Subsequent heating in order to further induce debromination

neither leads to 2D non-planar adsorbed covalent nor to planar organometallic networks. Again, the strong repulsive interaction between the organic backbones hinders the formation of ordered covalently interlinked nanostructures, but in principle the dehalogenation reaction is still steered by different temperature thresholds for I-C and C-Br bond scission, respectively.

Steric hindrance vs. adatoms - Furthermore, the comparative study of the halogenated pyrene derivative on Au(111) vs. Ag(111) showed the influence of intrinsic adatoms on temperature stability. The transfer of 2D organometallic into covalent networks on Ag(111) by heating at 200 °C was not achieved, but only a not anticipated desorption of the small pyrene building blocks was observed. However, the subsequent annealing on less reactive and less interacting Au(111) led to non-ordered interlinked nanostructures. Considering the initial C-Au and C-Ag intermediates, the C-Ag organometallic bond reversibility started at lower annealing temperatures, due to the lower bond energy as compared to the C-Au analogue. Additional DFT calculations indicated that the reaction barrier on Ag(111) cannot be overcome, and is induced by the repulsive hydrogen-hydrogen interaction. As a consequence, the pyrene molecule desorbs from the hot Ag(111) surface. In contrast, on Au(111), DFT calculations showed that the C-Au bond is strong enough to persist until a surface temperature is reached where the reaction barrier for covalently interlinking the nanostructures can be overcome. Yet, owing to the still strong steric hindrance the organic moieties are non-planar bonded.

Remote functionalization and conformational mechanics - The initial debromination of brominated molecules and organometallic interlinking is a commonly observed reaction on Ag(111) after RT deposition. However, the initial 1D organometallic chain formation of a fourfold brominated and perfluorinated biphenyl as well as for the hydrogenated analogue on Ag(111) is surprising. The required site-selective 3,5'-didebromination is mediated by the remote functionalization of the molecules. The debromination at the 3-position and C-Ag formation pins this site down to the surface and deactivates the 5-position by an increased adsorption height. Consequently, the Br atom at the 5'-position is decreased of the adsorption height and is cleaved from the molecule. This results in an unique 1D chain formation for a fourfold brominated and twofold symmetric molecule. The 1D chain formation is highly sensitive with respect to the surface temperature and is ceased by deposition onto a

preheated surface already at 50 °C.

Perflourination, polymorphism, and structural stability - A further unique observation for the perflourinated molecule is the structural polymorphism after converting the 1D chains into fully organometallic 2D structures, resulting in both a checkerboard (centered rectangular unit cell) and a flower structure (hexagonal unit cell). This polymorphism was exclusively observed for the perfluorinated precursor, whereas the hydrogenated analogue showed only the checkerboard structure. This seems to be strongly influenced by fluorine, but is not finally understood yet. Interestingly, organometallic networks (flower structure) of the perflourinated molecules showed a high temperature stability (∼300 °C) induced by an increased strength of the C-Ag-C linkages. However, organometallic networks of the hydrogenated precursor are transferred into covalently interlinked networks around 200 °C. Furthermore, perfluorinated precursor with its large dihedral angle between the phenyl rings, as compared to the hydrogenated analogue, features a reduced molecule-surface interaction. As a consequence, the perfluorinated molecule formed a more extended and reticular organometallic structure due to an enhanced diffusivity, respectively.

Surface-mediated metal-organic coordination

Liquid / air vs. on-surface synthesis - HATP as ligand in metal-organic coordinated nanostructures at the liquid / air interface was reported to form extended and reticular networks with the thermodynamically favored bis(diimino)-Cu motif.[17] However, neither Cu nor Ni coordinated structures on Cu(111) exhibited a comparable structural quality as in the solution chemistry based approach at the liquid / air interface. Upon coordination with the intrinsic adatoms of the Cu(111) surface, Cu_3 coordinated structures were favored, whereas extrinsic Ni adatoms showed the targeted bis(diimino)-Ni binding motif. Both, the intrinsic Cu and the extrinsic Ni adatoms, showed no extended networks and only less ordered metal-organic moieties (vide infra). Obviously, the transfer of a preparation protocol from the liquid / air interphase to surface-assisted polymerization is not directly feasible. Especially, the role of the absent liquid subphase affects metal-organic bond formation, and presumably induces a reduced bond reversibility.

Adsorption-sites vs. network formation - After RT deposition of HATP onto pristine Cu(111), XPS indicates intact molecules on the surface, i.e. non-deprotonated precursors. The HATP precursor with non-deprotonated amino groups is not able to form an extended self-assembly based on hydrogen bonds. Interestingly, well-defined cyclic hexamers are observed. DFT indicates that the self-assembly is driven by a strong affinity for preferred adsorption-sites. Analogous to the initial formed hexamers, the dominance of the preferred adsorption-sites is also presumed in the metal-organic coordination structures after heating. Both, the preferred adsorption-site of the triphenylene core and the coordinating Cu_3 cluster presumably hamper the formation of extended and ordered networks.

Intrinsic vs. extrinsic adatoms - For the HATP molecule on the pristine Cu(111) substrate slight heating activates the functional amino sites by means of dehydrogenation, followed by interlinking through metal-organic bonds. Coordination by intrinsic Cu adatoms results in Cu_3 cluster coordination with a strong affinity to preferred adsorption sites. However, the co-deposition of more reactive nickel results in an initial dehydrogenation and expression of a bis(diimino)-Ni coordination motif already after RT deposition. Interestingly, the nickel based metal-organic structures show also no extended network formation of the expected honeycomb structure, but nickel saturated binding sites at the termini. This may indicate that the bond reversibility is limited by the strong bis(diimino)-Ni coordination. This is further corroborated by the reduced domain sizes upon deposition of larger amounts of nickel.

Complementary approach of surface-sensitive analysis techniques

Advantages and limitations - In general, the present thesis demonstrates and confirms the excellent analytical strength of the complementary experimental approach of real-space imaging by STM and probing core level binding energies / unoccupied molecular orbitals by XPS and NEXAFS, respectively. For instance, for the non-planar adsorbed nanostructures, as presented in Sec. 4.3, STM cannot resolve any internal details, whereas XPS confirms a covalent coupling and NEXAFS proves the intactness of the aromatic system of the molecular backbone. Furthermore, the thermally induced desorption of the nanostructures is consistently found as the reduced coverage by local STM imaging and a decreased intensity in the corresponding XP spectra (Sec. 4.4). The study of metal-organic nanostructures (Sec. 6) showed that

the intuitive interpretation of the STM images of the hexamer formation after room temperature deposition of HATP, as a dehydrogenated imide self-assembly structure is indefensible. The corresponding XP spectra provide unambiguous evidence for intact tectons at room temperature. Moreover, the subsequent deprotonation and metal-organic coordination by additional thermal activation is monitored.

On the contrary, Sec. 5 showed the limitations of the complementary approach of STM and X-ray spectroscopy: After heating to 200 °C, STM clearly depicts organometallic networks, whereas XP spectroscopy shows a markedly reduced organometallic shoulder and an increased peak in the commonly covalent C 1s binding energy range. On the first view, this observation is contrary to the expectation. This apparent contradiction was only resolved by additional DFT core level calculations that showed a distinct difference in C 1s core level E_B depending on the degree of debromination. For fully organometallic networks C 1s is shifted towards higher E_B which could have been misinterpreted as covalently interlinked nanostructures. In addition to the not intuitively interpretable XP spectra, the corresponding NEXAFS spectra showed an unrealistically high tilt angle with respect to the surface for the obviously flat adsorbed organometallic structures. Consequently, a straightforward interpretation of the NEXAFS data assuming the transition dipole moment perpendicular to the phenyl ring is not indicated. This could possibly be induced by hybridization of molecular with surface electronic states or upward bending of fluorine substituents.

Outlook

The on-surface synthesis of nanostructures from molecular building blocks is a powerful approach with a potential for atomic structural precision. For the surface-mediated interlinking of the precursors a large progress was achieved in the fundamental understanding of surface-assisted polymerization and reaction during the last decade, but some issues are still neglected. With focus on possible applications, the dehalogenative coupling concentrates on the covalent bonding with its extraordinary stability, but with the disadvantage of an irreversibility of the bonds. Consequently, the absence of a bond reversibility represents a large challenge regard to the limited network size and high defect density.

As presented in this thesis, the organometallic and metal-organic coordination may provide appropriate alternatives to covalently interlinked nanostructures. Interlinking of the organic backbones via metal adatoms features the possibility of self-healing, and foremost the stability is raised for organometallic moieties by modi-

fying the side-groups of the molecular building blocks. For instance, hydrogen can be replaced by fluorine as presented in Sec. 5. To further study the influence of the side-groups, additional experiments are suggested, for instance by increasing the length of the perfluorinated biphenyl to a perfluorinated terphenyl and quarterphenyl, respectively. For both, a perfluorinated terphenyl and a quarterphenyl with bromine functional groups an initial debromination after RT deposition on Ag(111) is expected. The intension of such an experiment to study on an initial cis / trans organometallic chain formation by a site-selective 3,3"/ 3,5"'didebromination also for the terphenyl and quarterphenyl tecton through conformational mechanics, respectively. The crucial question is, if the dihedral angle between the phenyl rings is large enough to drive the necessary site-selective didebromination, or if the dihedral angle becomes reduced by an increased adsorbate-surface interaction. In addition, full organometallic networks of terphenyl and quarterphenyl precursors could possibly give further insights on polymorphism and temperature stability for on-surface synthesis of perfluorinated precursors. Furthermore, a molecule with a combination of hydrogen and fluorine side-groups could be studied, in order to determine whether a reduced amount of fluorine at the precursor leads to structures with an improved temperature stability.

In contrast to organometallic nanostructures, the stability of metal-organic networks could be enhanced by applying a denticity >1 per functional-site per precursor. Hence, both the coordination number of the metal coordination center and the bond strength are increased. Furthermore, more suitable substrates like less reactive Au(111) and an appropriate extrinsic metal coordination center may permit likewise self-healing of the nanostructures and an adequate strength of intermolecular interlinking. This approach could serve as basis for further post-synthetic decoupling of the metal-organic structures, for instance by iodine intercalation.[61,62]

Additionally, the introduction of a novel immersion-scanning-tunneling-microscope at liquid-solid interfaces, developed by Ochs et al.,[212] could be directly applied to monitor the single layer formation of metal-organic interlinked HATP molecules in an ionic solution on (non-)metallic surfaces. This newly introduced STM enables the necessary in-situ thermal activation.

List of Publications

8. **M. Lischka**, R. Dong, M. Wang, M. Fritton, L. Grossmann, N. Martsinovich, W. M. Heckl, X. Feng, and M. Lackinger: Initial metal-coordination of hexaaminotriphenylene on Ag(111) and extrinsic nickel induced polymorphism, **2018**, in preparation

7. **M. Lischka**, R. Dong, M. Wang, M. Fritton, L. Grossmann, N. Martsinovich, W. M. Heckl, X. Feng, and M. Lackinger: Competitive metal-coordination of hexaaminotriphenylene on Cu(111) by intrinsic copper versus extrinsic nickel adatoms, *Chem. Eur, J.*, **2018**, submitted

6. **M. Lischka**, G. S. Michelitsch, N. Martsinovich, J. Eichhorn, A. Rastgoo-Lahrood, T. Strunskus, R. Breuer, K. Reuter, M. Schmittel, W. M. Heckl, and M. Lackinger: Remote functionalization in surface-assisted dehalogenation guided by conformational mechanics: organometallic self-assembly of 3,3',5,5'-tetrabromo-2,2',4,4',6,6'-hexafluorobiphenyl on Ag(111), *Nanoscale*, **2018**, 10, 12035–12044

5. **M. Lischka**, M. Fritton, J. Eichhorn, V. S. Vyas, T. Strunskus, B. V. Lotsch, J. Björk, W. M. Heckl, and M. Lackinger: On-Surface Polymerization of 1,8-Dibromo-3,6-diiodopyrene – a Comparative Study on Au(111) vs. Ag(111) by STM, XPS, and NEXAFS, *J. Chem. Phys. C*, **2018**, 122, 5967–5977

4. A. Rastgoo-Lahrood, **M. Lischka**, J. Eichhorn, D. Samanta, M. Schmittel, W. M. Heckl, and M. Lackinger: Reversible intercalation of iodine monolayers between on-surface synthesised covalent polyphenylene networks and Au(111), *Nanoscale*, **2017**, 9, 4995–5001

3. A. Rastgoo-Lahrood, N. Martsinovich, **M. Lischka**, J. Eichhorn, P. Szabelski, D. Nieckarz, T. Strunskus, K. Das, M. Schmittel, W. M. Heckl, and M. Lackinger: From Au–Thiolate chains to thioether Sierpiński triangles: The versatile surface chemistry of 1,3,5-Tris(4-mercaptophenyl)benzene on Au(111), *ACS Nano*, **2016**, 10 (12), 10901–10911

2. A. Rastgoo-Lahrood, J. Björk, **M. Lischka**, J. Eichhorn, S. Kloft, M. Fritton, T. Strunskus, D. Samanta, M. Schmittel, W. M. Heckl, M. Lackinger: Post-Synthetic decoupling of on-surface-synthesized covalent nanostructures from Ag(111), *Angew. Chem. Int. Ed.*, **2016**, 55, 7650–7654.

1. T. Sirtl, **M. Lischka**, J. Eichhorn, A. Rastgoo-Lahrood, T. Strunskus, W. M. Heckl, and M. Lackinger, From benzenetrithiolate self-assembly to Copper Sulfide adlayers on Cu(111): Temperature-Induced irreversible and reversible phase transitions, *J. Phys. Chem. C*, **2014**, 118 (7), 3590–3598

Appendix A

Supplementary information of Br_2I_2Py on Au(111) and Ag(111)

A.1 STM data on Au(111)

Formation of organometallic trimers after RT deposition

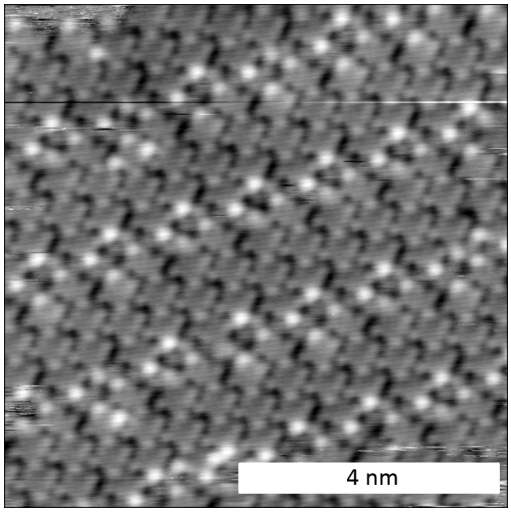

Figure A.1: STM image acquired after RT deposition of Br_2I_2Py onto Au(111) showing occasionally observed organometallic trimers. Remaining iodine-substituents appear as bright protrusion. Formation of organometallic trimers requires full deiodination of the central pyrene moiety, i.e. correspond to an overall degree of deiodination of 67%. Self-assembly of the organometallic trimers into densely packed structures is again directed by halogen-halogen bonds (tunneling parameters: 33.7 pA, 0.03 V).

Deposition onto preheated Au(111) with different deposition rates

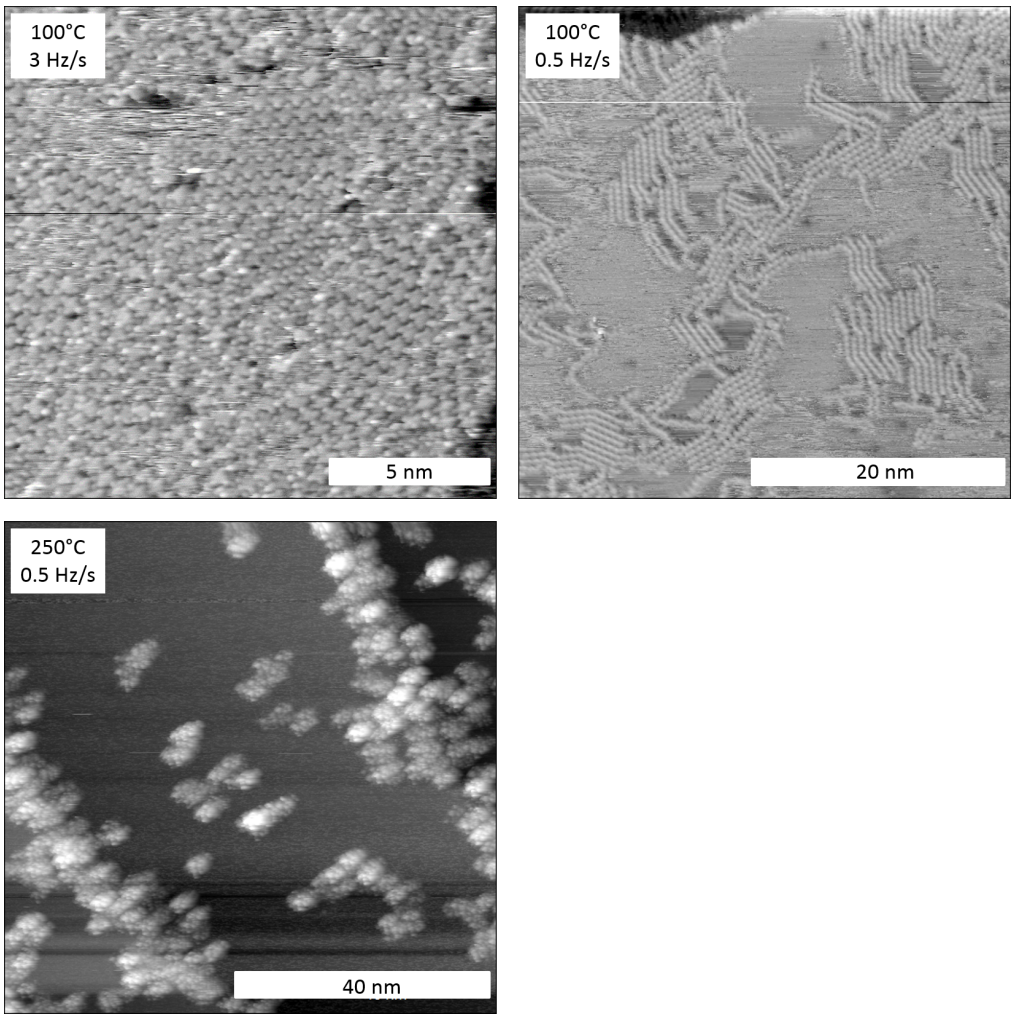

Figure A.2: STM images acquired after deposition of Br_2I_2Py onto Au(111) held at temperatures of 100 °C and 250 °C, respectively. For the 100 °C deposition the results were obtained with two different deposition rates, i.e. (a) 3.0 Hz/s ($T_{crucible}$ = 180 °C, $t_{deposition}$ = 3.0 min) and (b) 0.50 Hz/s ($T_{crucible}$ = 165 °C, $t_{deposition}$ = 18 min), yielding comparable coverages. Here the eigenfrequency decline $\frac{\Delta f}{\Delta t}$ of a quartz crystal microbalance (QCMB) serves as a quantitative measure of the deposition rate. No significant differences were observed in comparison to samples prepared according to the standard preparation protocol, i.e. RT deposition with a rate corresponding to 3.0 Hz/s and subsequent annealing to 100 °C. (tunneling parameters: 58.2 pA, 0.67 V; 90.1 pA, 0.90 V; 43.9 pA, 0.91 V).

Reduced heating and cooling rate

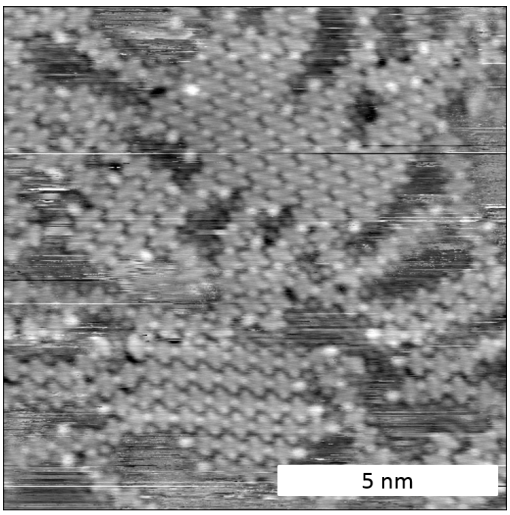

Figure A.3: STM image acquired after RT deposition of Br_2I_2Py onto Au(111) and subsequent annealing to 100 °C with reduced heating and cooling rate of 0.28 °C min^{-1}. Yet, no differences to heating treatments with the normally applied heating and cooling rate of 6.6 °C min^{-1} could be discerned in STM. (tunneling parameters: 49.2 pA, 580 mV)

A.2 STM data on Ag(111)

Reduced heating and cooling rate

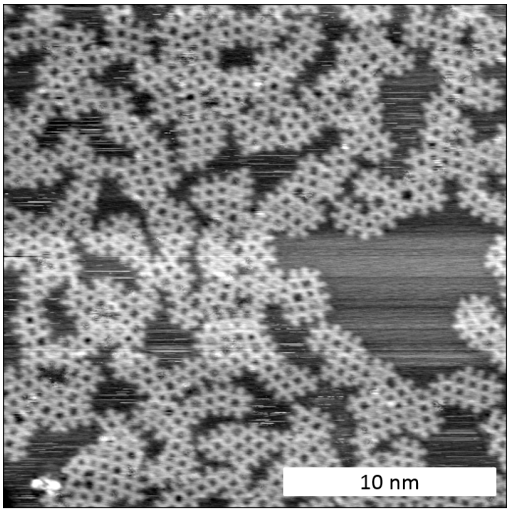

Figure A.4: STM image acquired after RT deposition of Br_2I_2Py onto Ag(111) and subsequent annealing to 125 °C with reduced heating and cooling rate of 0.28 °C min^{-1}. Yet, no improvement of the long-range order of the 2D organometallic networks was observed as compared to heating treatments with the normally applied heating and cooling rate of 6.6 °C min^{-1}. (tunneling parameters: 52.6 pA, 680 mV)

A.3 XPS data on Ag(111)

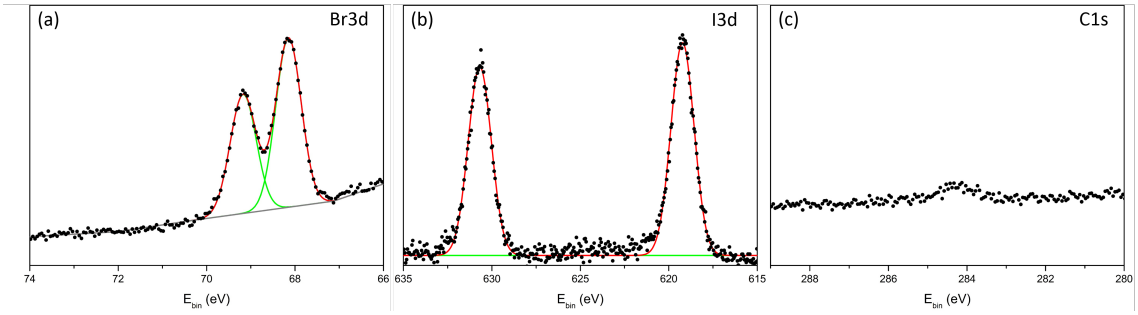

Figure A.5: XP spectra of (a) Br 3d, (b) I 3d, and (c) C 1s (c) acquired after RT deposition of Br_2I_2Py onto Ag(111) and subsequent annealing to 250 °C. Raw data are represented by dots; solid lines show fits with a Gaussian line shape and linear background; red lines correspond to the sum of all components. The remaining Br is chemisorbed on Ag(111) and the 30% reduced intensity indicates substantial desorption. Annealing to 250 °C did not result in any changes of I 3d neither in binding energy nor in intensity, indicating stable adsorption of the split off iodine. Except for a small remainder, the C 1s intensity diminished, indicating nearly complete desorption of the molecules.

A.4 DFT calculations

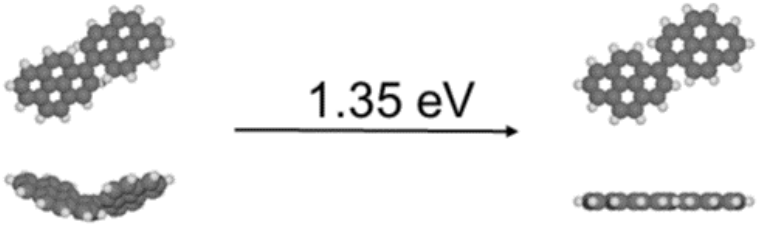

Figure A.6: DFT-optimized geometries of the 1-1' covalently linked pyrene with (left) unconstrained and (right) constrained to planar geometry, respectively. The energy difference, i.e. the energy cost of planarization, amounts to +1.35 eV.

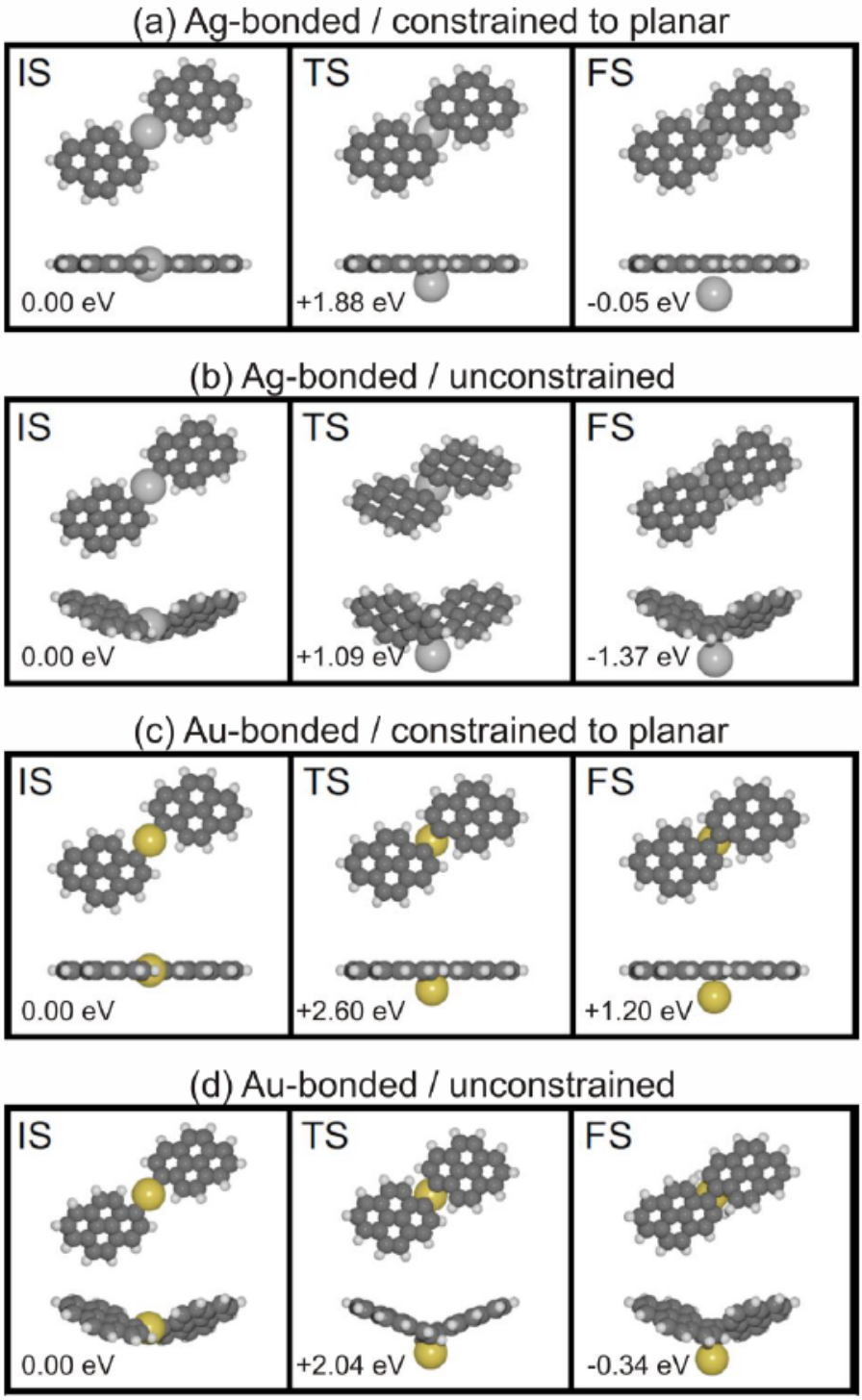

Figure A.7: DFT-derived reaction barriers for the conversion of organometallic into covalent pyrene dimers in the gas phase. (a) Ag-bonded, constrained to planar; (b) Ag-bonded, unconstrained; (c) Au-bonded, unconstrained; (d) Au-bonded, constrained to planar; In all cases, the initial state (IS) energy corresponds to 0.00 eV, and the respective transition state (TS) and final state (FS) energies are indicated.

Appendix B

Supplementary information of Br_4F_6BP and Br_4BP on Ag(111)

B.1 STM and XPS data: Br_4F_6BP on Ag(111)

Overview STM images after room temperature deposition

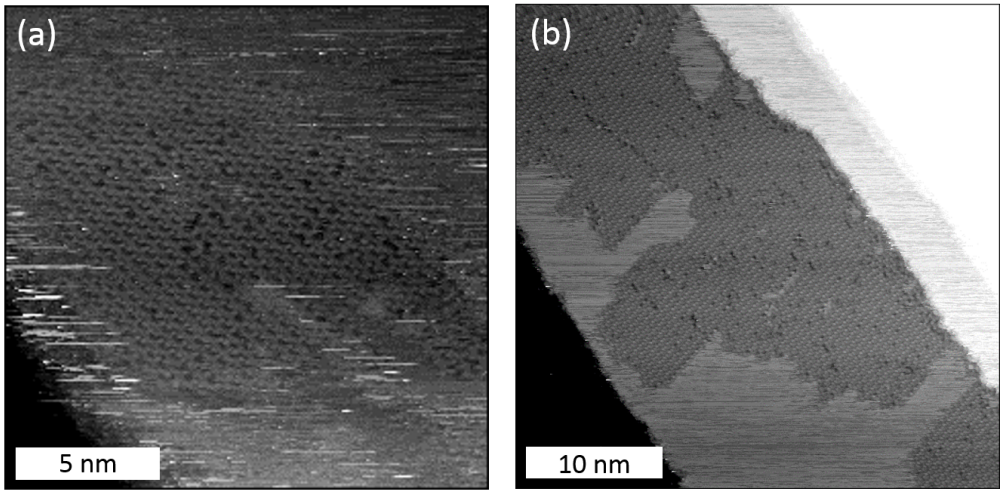

Figure B.1: Large-scale STM images acquired after room-temperature deposition of Br_4F_6BP on Ag(111), showing (a) more loosely (corresponding to Fig. 5.2(a) in the manuscript) and (b) more densely (corresponding to Fig. 5.2(b) in the manuscript) packed arrangements of 1D organometallic chains; Interestingly, the average chain lengths as derived from these images corresponding to (a) (12.7 ± 11) nm and (b) (14.7 ± 13.6) nm (b) are relatively similar. (tunneling parameters: (a) 0.09 V, 115 pA; (b) 0.91 V, 91 pA)

Overview STM images after annealing

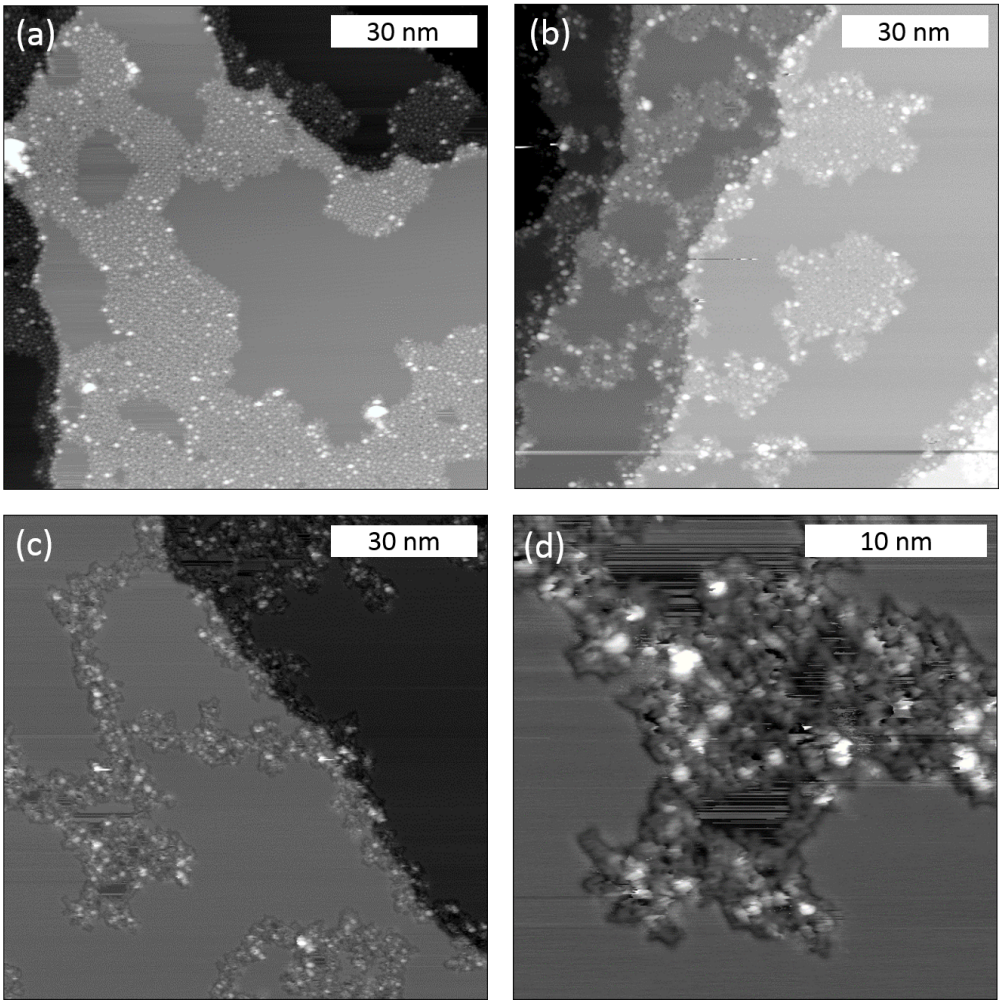

Figure B.2: Large-scale STM images acquired after room-temperature deposition of Br_4F_6BP onto Ag(111) and subsequent annealing at (a) 200 °C, (b) 300 °C, and (c) 400 °C; (d) close-up image recorded after annealing to 400 °C; no ordered molecular structures cannot be resolved anymore, even though the disordered aggregates appear with relatively uniform height; formation of covalent aggregates is highly plausible, but cannot unambiguously proven by these data. (all overview images are measured in an area of (100 × 100) nm^2; tunneling parameters: (a) 0.93 V, 63 pA; (b) 0.88 V, 93 pA; (c) 0.88 V, 90 pA; (d) 0.88 V, 110 pA)

Annealing to 200 °C with reduced heating and cooling rates

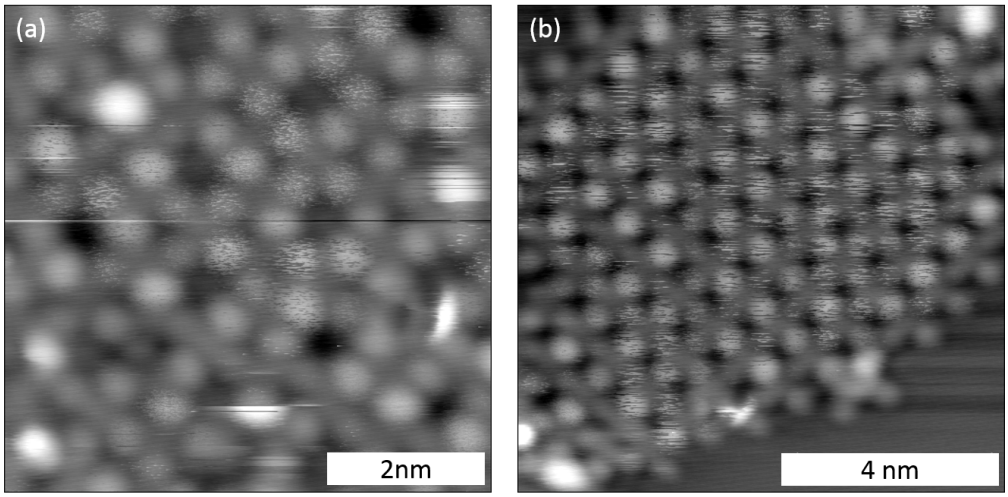

Figure B.3: STM images acquired after RT deposition of Br_4F_6BP onto Ag(111) and subsequent annealing to 200 °C with a reduced heating and cooling rate of 1.5 °C min^{-1}. Yet, no differences to heating treatments for the (a) flower and (b) checkerboard structure with the normally applied heating and cooling rate of 5.8 °C min^{-1} could be discerned. (tunneling parameters: (a) 0.71 V, 39 pA; (b) 0.93 V, 45 pA)

Statistical analysis of the 3,5'-site-selectivity

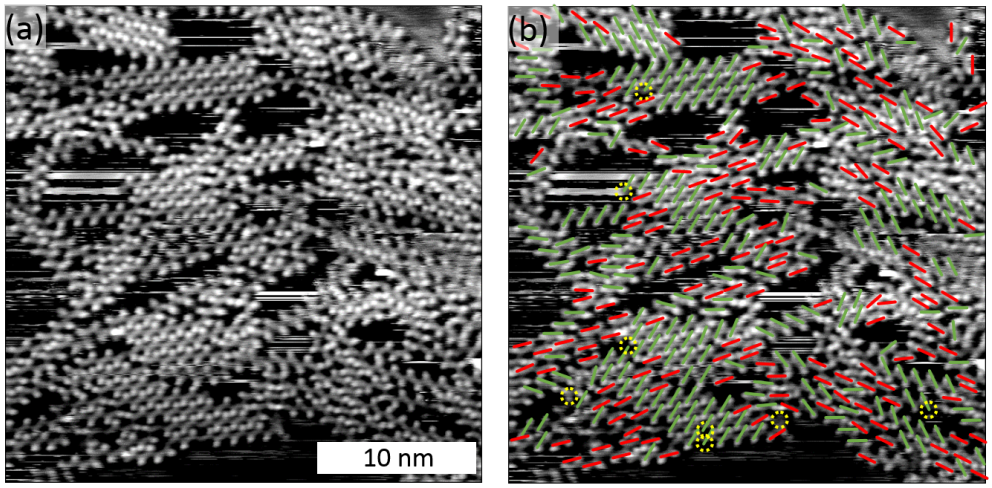

Figure B.4: Statistical analysis of a STM images acquired after room temperature deposition of Br_4F_6BP on Ag(111); (a) raw image, (b) same image with color coding for the debromination; green corresponds to the expected site-selective 3,5'-didebromaintion (255 counts), whereas red indicates defects with a 3,3'-didebromaintion (180 counts); yellow circles show molecules with one remaing bromine substituent. (tunneling parameters: 1.26 V, 22 pA)

Spatial distribution of noisy appearing vs. stably imaged Ag atoms

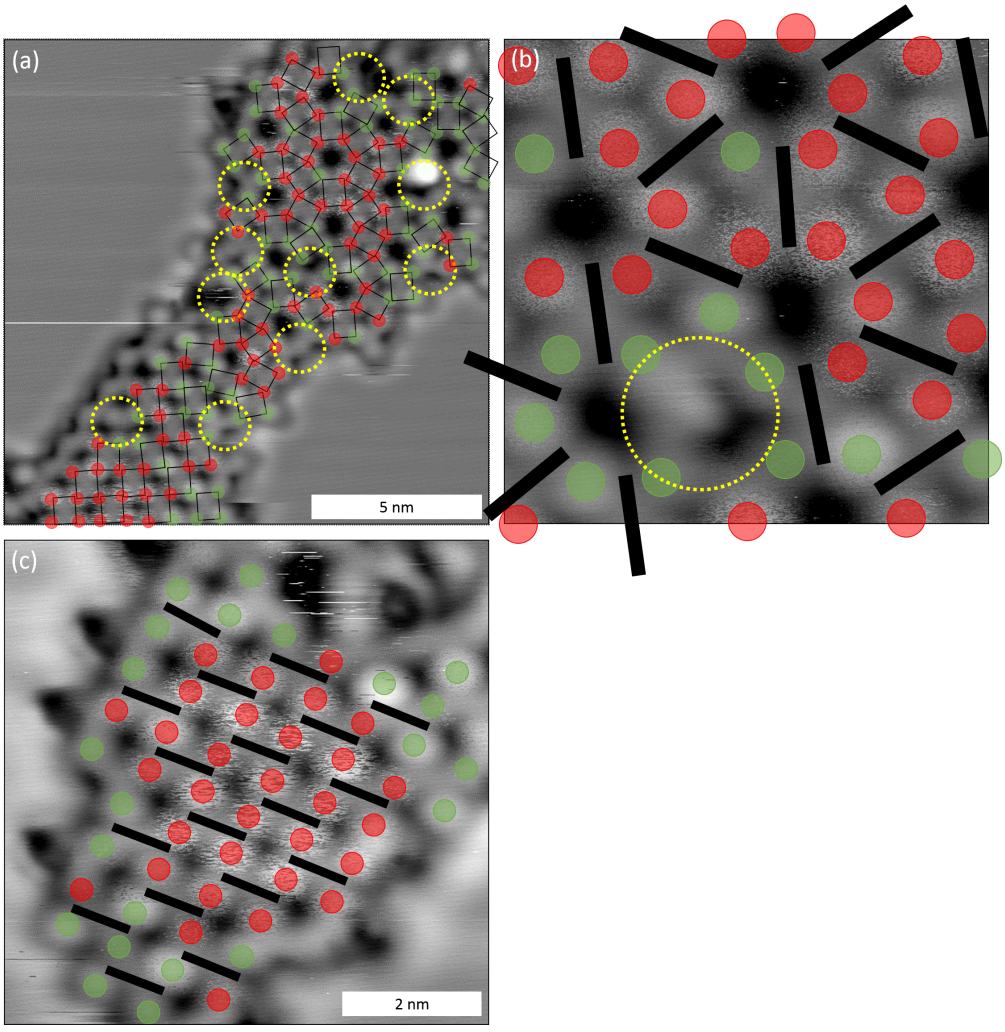

Figure B.5: STM images of Br_4F_6BP on Ag(111) after annealing to 200 °C; (a) overview, (b) flower, (c) checkerboard structure; two different types of STM contrast could be distinguished for Ag atoms in the organometallic linkages: (1) noisy appearing Ag atoms (red) and (2) stable appearing Ag atoms. The color code aids in illustrate the spatial distribution of both contrast types, black bars symbolize biphenyl units. Nosiy Ag atoms are the dominant species within well ordered organometallic domains, whereas stable Ag atoms (green) are mostly located at domain boundaries and around vacancies (marked by yellow circles). (tunneling parameters: (a) 0.58 V, 45 pA; (b) 0.58 V, 45 pA; (c) 0.60 V, 47 pA)

F 1s XP spectra of Br_4F_6BP on Ag(111)

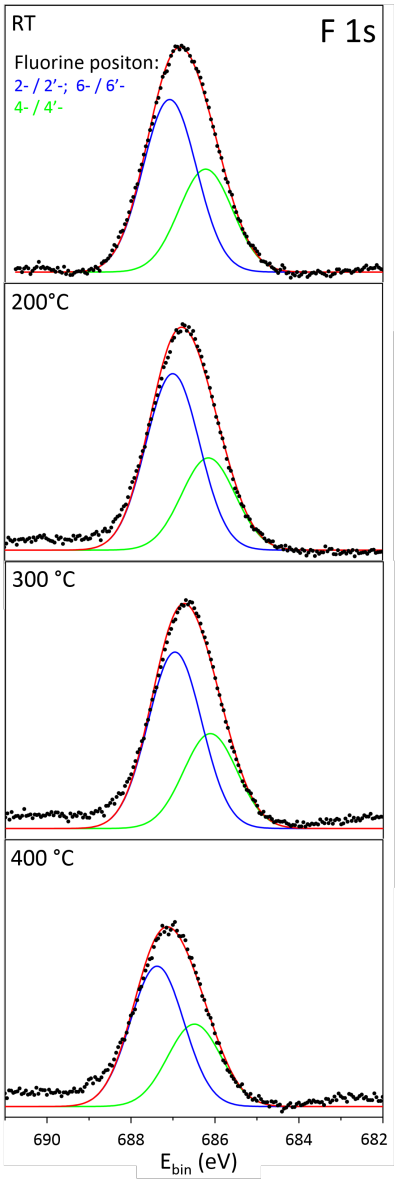

Figure B.6: F 1s XP spectra acquired after deposition of Br_4F_6BP onto Ag(111) held at room temperature and successive annealing to the indicated temperatures up to 400 °C. Raw data are represented by dots; solid lines show fits with Gaussian line-shape and linear background. F 1s spectra were fitted with two components corresponding to the inequivalent fluorine substituents: F at 4- / 4'-position: green; F at 2- / 2'-position and 6- / 6'-position: blue; according to the molecular structure a fixed 1:2 ratio was applied; Annealing at 400 °C already results in a loss of fluorine due to degradation of the molecules by defluorination.

XPS fitting parameters for Br_4F_6BP on Ag(111)

C 1s at RT Fig. 5.3(a)					
peak	peak type	FWHM	E_B (eV)	rel. area (%)	assigned to
1	Gaussian	1.2	283.6	12	$^1/_2$Br / $^1/_2$C-Ag
2	Gaussian	1.2	285.0	20	C-C
3	Gaussian	1.2	285.5	24	C-Br
4	Gaussian	1.2	286.8	27	C-F (4,4')
5	Gaussian	1.2	286.9	17	C-F (2,6';2',6)
C 1s at 200 °C Fig. 5.3(c)					
peak	peak type	FWHM	E_B (eV)	rel. area (%)	assigned to
1	Gaussian	1.0	283.6	7	$^1/_2$Br / $^1/_2$C-Ag
2	Gaussian	1.0	284.8	28	C-Ag
3	Gaussian	1.0	284.8	2	C-Br
4	Gaussian	1.0	284.9	18	C-C
5	Gaussian	1.0	286.5	15	C-F (2,6';2',6)
6	Gaussian	1.0	286.7	30	C-F (4,4')
C 1s at 300 °C Fig. 5.3(e)					
peak	peak type	FWHM	E_B (eV)	rel. area (%)	assigned to
1	Gaussian	1.0	283.6	5	$^1/_2$Br / $^1/_2$C-Ag
2	Gaussian	1.0	284.8	38	C-Ag
3	Gaussian	1.0	284.8	2	C-Br
4	Gaussian	1.0	284.9	13	C-C
5	Gaussian	1.0	286.5	15	C-F (2,6';2',6)
6	Gaussian	1.0	286.7	27	C-F (4,4')

Table B.1: C 1s XPS fitting parameters for Br_4F_6BP on Ag(111).

Br 3d at RT Fig. 5.3(b)					
peak	peak type	FWHM	E_B (eV)	rel. area (%)	assigned to
1	Gaussian	0.7	68.1	22	Chemisorbed Br ($Br_{d5/2}$)
2	Gaussian	0.8	69.1	17	Chemisorbed Br ($Br_{d3/2}$)
3	Gaussian	0.9	70.2	35	Br-C ($Br_{d5/2}$)
4	Gaussian	1.0	71.3	26	Br-C ($Br_{d3/2}$)
Br 3d at 200 °C Fig. 5.3(d)					
peak	peak type	FWHM	E_B (eV)	rel. area (%)	assigned to
1	Gaussian	0.7	68.0	45	Chemisorbed Br ($Br_{d5/2}$)
2	Gaussian	0.8	69.1	42	Chemisorbed Br ($Br_{d3/2}$)
3	Gaussian	1.2	70.3	9	Br-C ($Br_{d5/2}$)
4	Gaussian	0.9	71.4	4	Br-C ($Br_{d3/2}$)
Br 3d at 300 °C Fig. 5.3(f)					
peak	peak type	FWHM	E_B (eV)	rel. area (%)	assigned to
1	Gaussian	0.7	68.1	51	Chemisorbed Br ($Br_{d5/2}$)
2	Gaussian	0.8	69.1	39	Chemisorbed Br ($Br_{d3/2}$)
3	Gaussian	1.3	70.2	7	Br-C ($Br_{d5/2}$)
4	Gaussian	0.9	71.5	2	Br-C ($Br_{d3/2}$)

Table B.2: Br 3d XPS fitting parameters for Br_4F_6BP on Ag(111).

F 1s at RT Fig. B.6					
peak	peak type	FWHM	E_B (eV)	rel. area (%)	assigned to
1	Gaussian	1.5	686.2	37	4- / 4'-
2	Gaussian	1.5	687.1	63	2- / 2'-; 6- / 6'-
F 1s at 200 °C Fig. B.6					
peak	peak type	FWHM	E_B (eV)	rel. area (%)	assigned to
1	Gaussian	1.5	686.1	34	4- / 4'-
2	Gaussian	1.5	687.0	66	2- / 2'-; 6- / 6'-
F 1s at 300 °C Fig. B.6					
peak	peak type	FWHM	E_B (eV)	rel. area (%)	assigned to
1	Gaussian	1.5	686.1	35	4- / 4'-
2	Gaussian	1.5	687.0	65	2- / 2'-; 6- / 6'-
F 1s at 400 °C Fig. B.6					
peak	peak type	FWHM	E_B (eV)	rel. area (%)	assigned to
1	Gaussian	1.5	686.1	37	4- / 4'-
2	Gaussian	1.5	687.0	63	2- / 2'-; 6- / 6'-

Table B.3: F 1s XPS fitting parameters for Br_4F_6BP on Ag(111).

B.2 STM data: Br_4BP on Ag(111)

Chain formation via site-selective debromination and influence of surface temperature

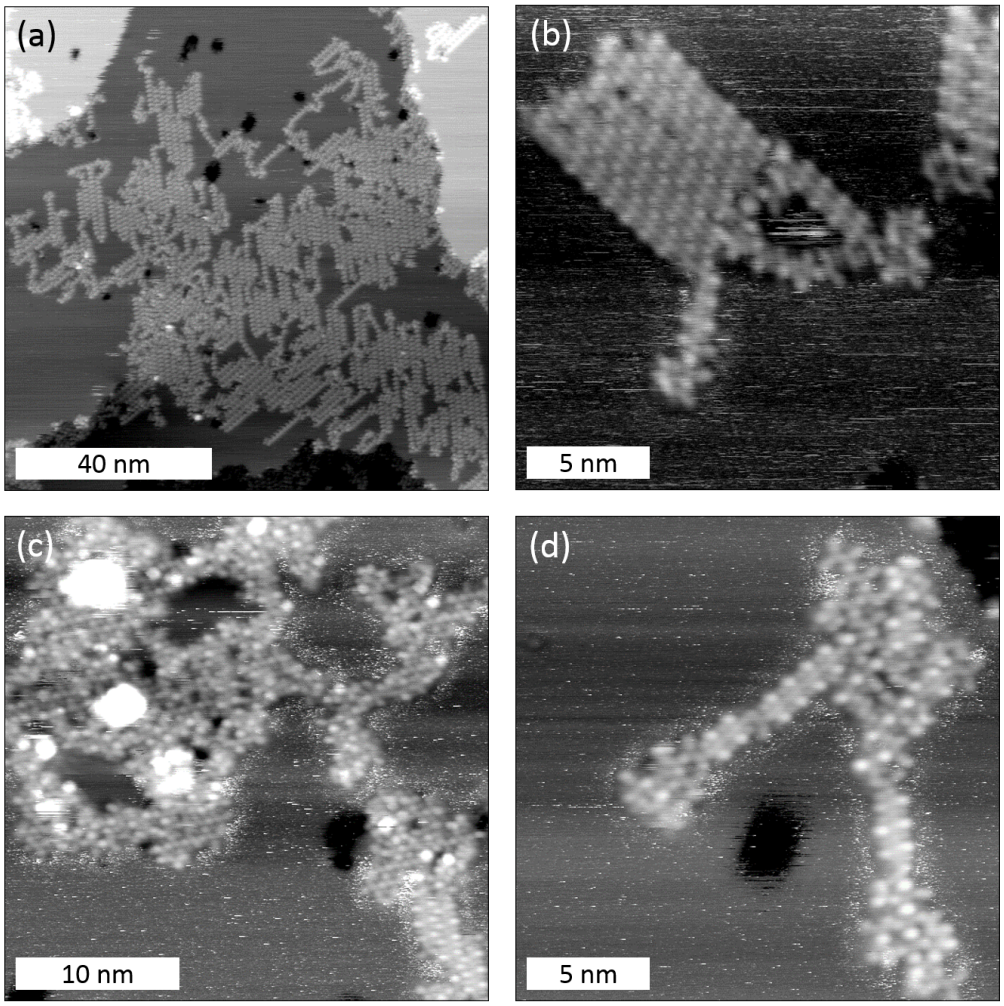

Figure B.7: STM images acquired after RT deposition of Br_4BP onto Ag(111) with the (a) / (b) the surface held at room temperature and (c) / (d) preheated to 50 °C; the overview image (a) shows the formation of linear structures, clearly resolved as organometallic chains in the close-up in (b); the repeat distance of (1.06 ± 0.04) nm perfectly matches the Br_4F_6BP derived organometallic chains; Yet, the chain formation by site-selective debromination is highly sensitive on the surface temperature as shown in (c) and (d): deposition onto sample surface preheated to 50 °C induces a higher number of defects and also leads to the first expression of 2D patterns by progressive debromination; only short segments of organometallic chains are still observed; (tunneling parameters: (a) 0.86 V, 94 pA; (b) 0.48 V, 93 pA; (c) 1.49 V, 95 pA; (d) 1.49 V, 96 pA).

STM images of Br_4BP on Ag(111) after annealing

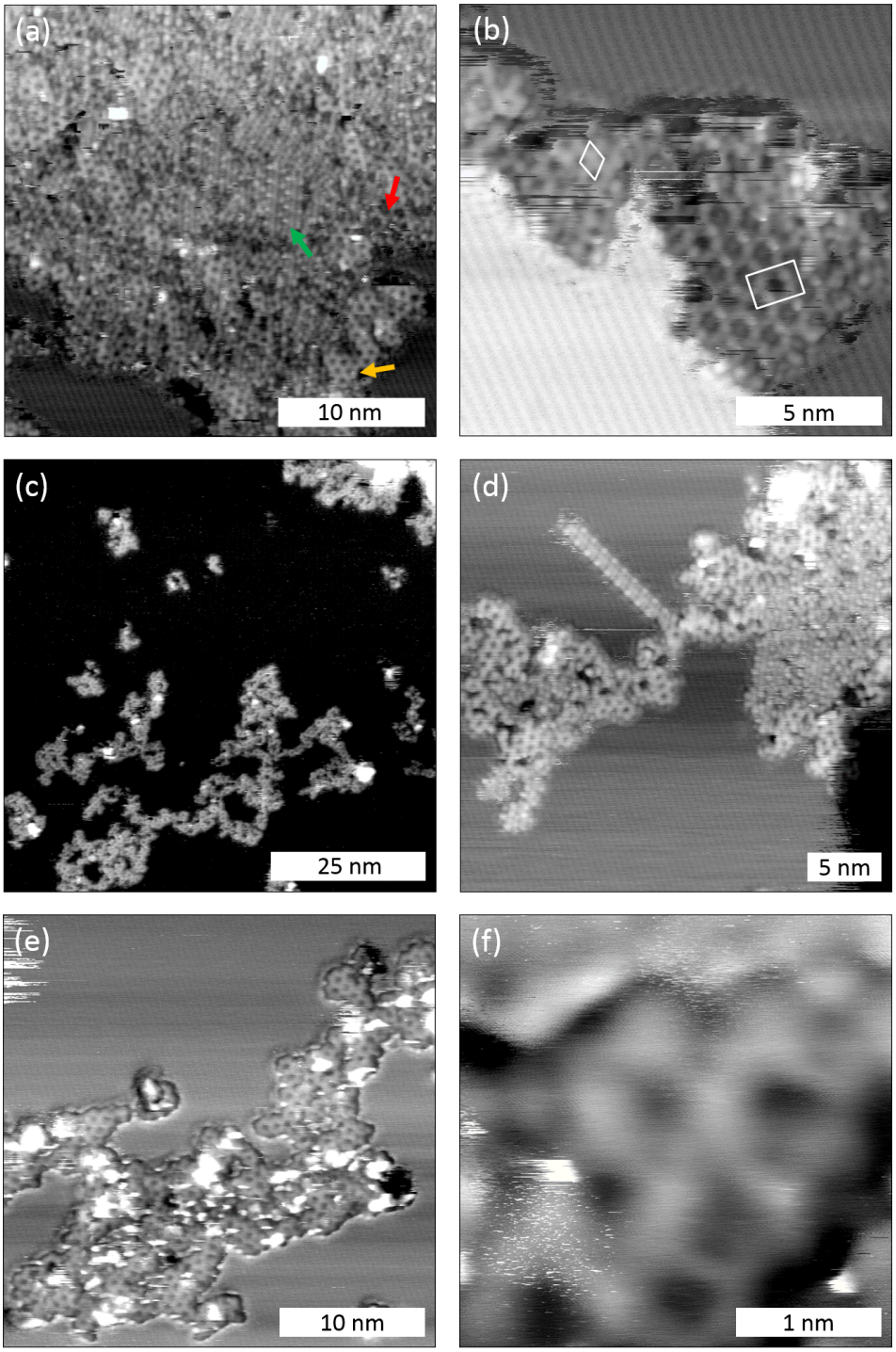

Figure B.8: STM images of Br_4BP on Ag(111) acquired after subsequent annealing to (a) / (b) 200 °C; (c) / (d) 300 °C; (e) / (f) 400 °C, with a heating and cooling rate of 3.33 °C min^{-1}. After annealing at 200 °C three different structures can be observed by STM: (1) 1D organometallic chains (green arrow), →

(2) small patches of the centered rectangular organometallic checkerboard structure (red arrow in (a), white rectangle in (b)) with lattice parameters of a = (1.75 ± 0.10) nm, b = (1.20 ± 0.07) nm that are within the experimental error identical to the Br_4BP derived checkerboard structure; (3) a porous structure pores with a hexagonal unit cell with a = b = (0.83 ± 0.06) nm (yellow arrow in (a), white diamond in (b); this lattice parameter could not be match with any of the derived structures, but corresponds to a covalent checkerboard structure that is similar with "porous graphene" previously reported by Fasel and coworkers[113]; upon further annealing the 1D chains are replaced by the organometallic checkerboard pattern, yet with relatively small domain sizes and a high amount of more disordered areas; subsequently, the organometallic structures are converted into covalent structures, as deduced from the change of lattice parameters; In contrast to Br_4F_6BP, for Br_4BP large portions of the surface are covered by closed layers of dissociated Br (see striped structures in (b)); the origin of this interesting difference is not clear, but might account for the high disorder and small domain sizes in the organometallic self-assembly of Br_4BP; (tunneling parameters: (a) 0.89 V, 85 pA; (b) 0.89 V, 84 pA; (c) 1.10 V, 94 pA; (d) 1.52 V, 95 pA; (e) 1.27 V, 91 pA; (f) 1.27 V, 91 pA)

B.3 DFT simulations

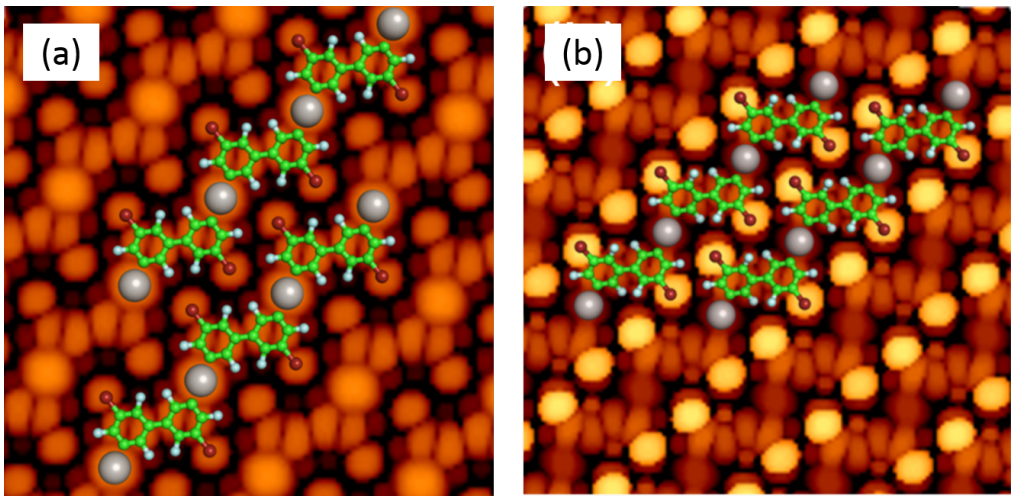

Figure B.9: STM image simulations of both (a) planar and (b) tilted free-standing organometallic chains, i.e. without Ag(111) substrate. The underlying DFT-optimized structures are shown as overlays. For the non-planar chain all Ag atoms were constrained to the same height. This results in a tilting of the phenyl rings in the biphenyl unit with a dihedral angle of ∼49°. In the adsorbed state for a symmetric geometry, the phenyl tilt angle with respect to the surface is given by half of the dihedral angle.

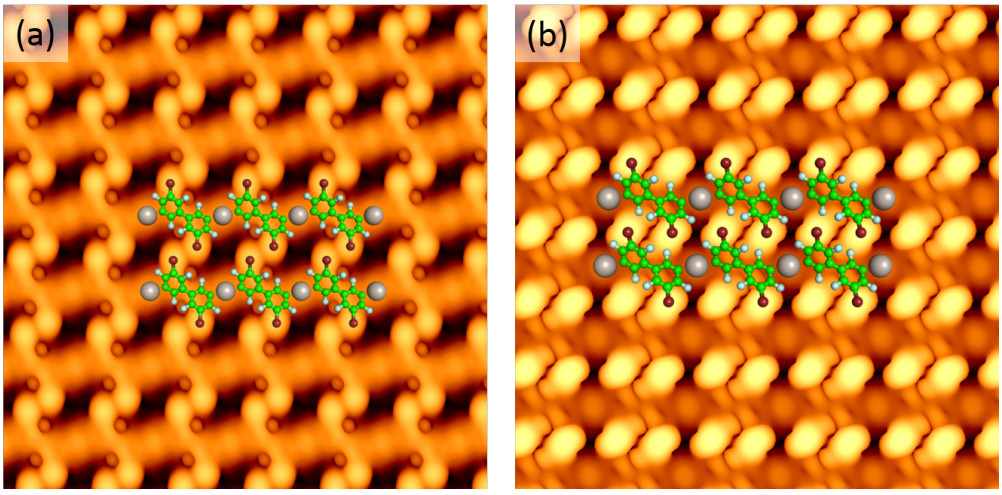

Figure B.10: STM image simulations of adsorbed organometallic chains including the Ag(111) substrate; the underlying DFT-optimized structures are shown as overlays: (a) less densely packed structure with a repeat distance along the chain of 1.05 nm and a chain separation of 1.05 nm (b) more densely packed structure with a repeat distance along the chain of 1.05 nm and a chain separation of 0.78 nm; in both structures the phenyl rings remain tilted with respect to the surface; the simulated STM images are in perfect agreement with the experiment.

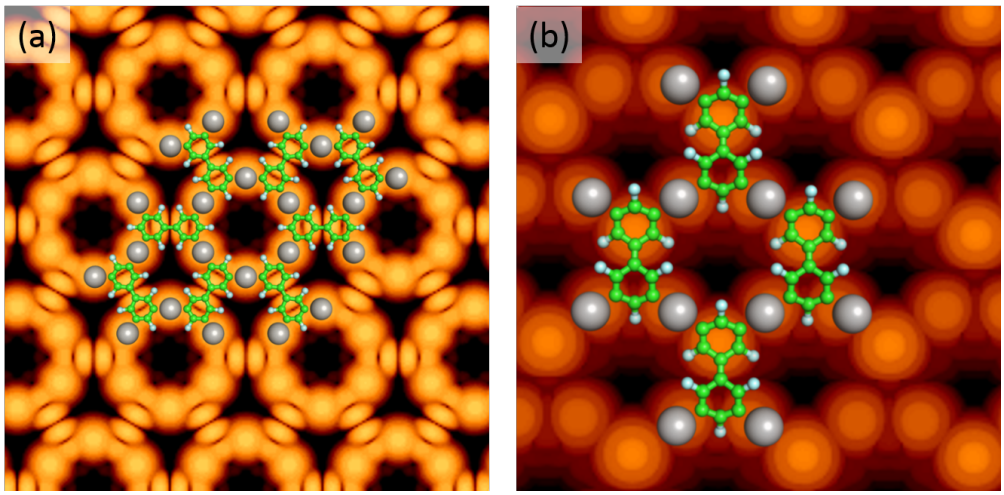

Figure B.11: STM image simulations of both organometallic (a) flower and (b) checkerboard structure. The underlying DFT-optimized structures with enforced planar geometry are shown as overlays. In both cases, the Ag atoms in the C-Ag-C linkages appear with a pronounced contrast in accordance with the experiment.

B.4 STM and XPS data: Br_4F_6BP on Au(111)

STM images of Br_4F_6BP on Au(111)

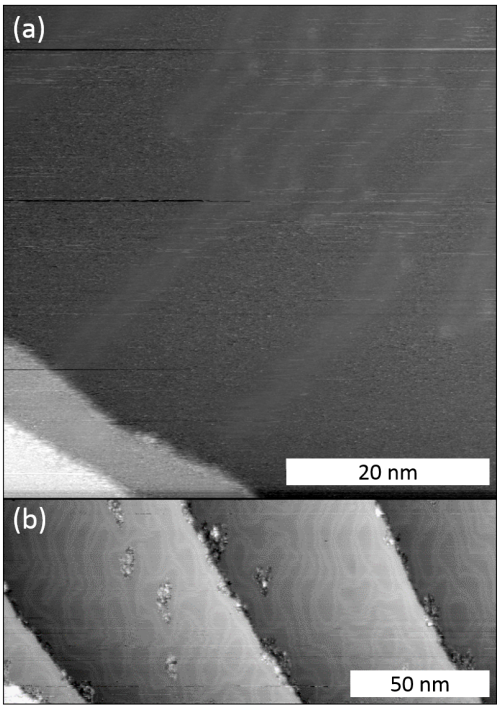

Figure B.12: STM data acquired after deposition of Br_4F_6BP on Au(111) at (a) room temperature and (b) after annealing to 200 °C. At room temperature, the intact monomers are too mobile to be imaged with STM and the surface appears empty, even though the herringbone reconstruction is locally perturbed. Upon annealing, the majority of molecules was desorbed (cf. XPS in Fig. B.13), yet not further resolved aggregates were found scattered across the surface. (tunneling parameters: (a) 1.54 V, 48 pA; (b) 0.98 V, 82 pA).

XP spectra of C 1s and Br 3d core-levels of Br_4F_6BP on Au(111)

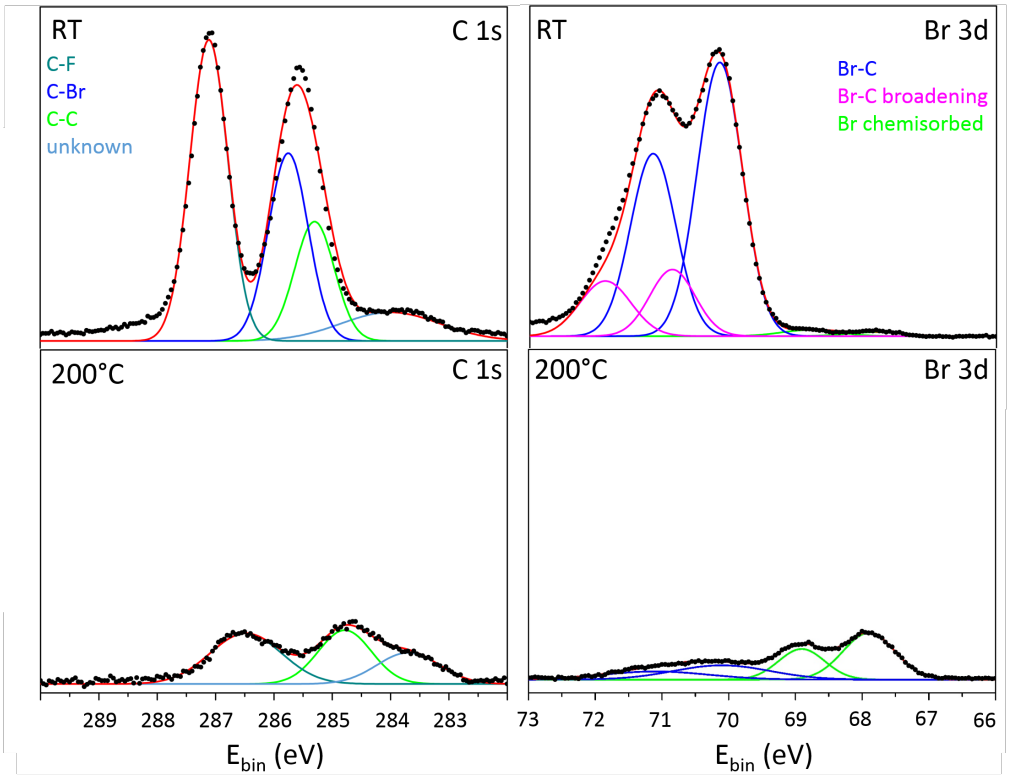

Figure B.13: C 1s and Br 3d XP spectra acquired after deposition of Br_4F_6BP on Au(111) at (a) room temperature and (b) after annealing to 200 °C. At room temperature almost no Br is dissociated, hence mostly intact monomers are present on the surface. Obtaining a reasonable fit required an additional Br 3d doublet with a higher binding energy, account for 21% of the total intensity. This additional Br species is tentatively assigned to molecules in special adsorption-sites or second layer coverage, but the exact origin remains unclear at the moment. After annealing, most molecules and Br desorbed, with small remainders of a carbonaceous species and split off Br still present. Raw data are represented by dots; solid lines show fits (fitted with a Gaussian line shape and linear background), where red lines corresponds to the sum of all components.

XPS fitting parameters for Br_4F_6BP on Au(111)

C 1s at RT Fig. B.13					
peak	peak type	FWHM	E_B (eV)	rel. area (%)	assigned to
1	Gaussian	2	284	11	-
2	Gaussian	0.8	285.3	18	C-C
3	Gaussian	0.8	285.8	28	C-Br
4	Gaussian	0.8	287.1	43	C-F
C 1s at 200 °C Fig. B.13					
peak	peak type	FWHM	E_B (eV)	rel. area (%)	assigned to
1	Gaussian	1.3	283.7	23	-
2	Gaussian	1.1	284.8	33	C-C
3	Gaussian	1.4	286.5	43	C-F

Table B.4: C 1s XPS fitting parameters for Br_4F_6BP on Au(111).

Br 3d at RT Fig. B.13					
peak	peak type	FWHM	E_B (eV)	rel. area (%)	assigned to
1	Gaussian	1	67.8	1	Chemisorbed Br ($Br_{d5/2}$)
2	Gaussian	1	68.8	1	Chemisorbed Br ($Br_{d3/2}$)
3	Gaussian	0.8	70.2	46	Br-C ($Br_{d5/2}$)
4	Gaussian	0.8	70.9	11	Br-C ($Br_{d5/2}$) broadening
5	Gaussian	0.8	71.2	31	Br-C ($Br_{d3/2}$)
6	Gaussian	0.9	71.9	10	Br-C ($Br_{d3/2}$) broadening
Br 3d at 200 °C Fig. B.13					
peak	peak type	FWHM	E_B (eV)	rel. area (%)	assigned to
1	Gaussian	0.9	67.8	40	Chemisorbed Br ($Br_{d5/2}$)
2	Gaussian	0.8	68.9	29	Chemisorbed Br ($Br_{d3/2}$)
3	Gaussian	1.7	70.1	23	Br-C ($Br_{d5/2}$)
4	Gaussian	1.9	71.1	14	Br-C ($Br_{d3/2}$)

Table B.5: Br 3d XPS fitting parameters for Br_4F_6BP on Au(111).

Appendix C

Supplementary information of HATP on Cu(111) and on nickel-covered Cu(111)

C.1 STM data: HATP on Cu(111) and on Cu(111) + Ni

Overview images

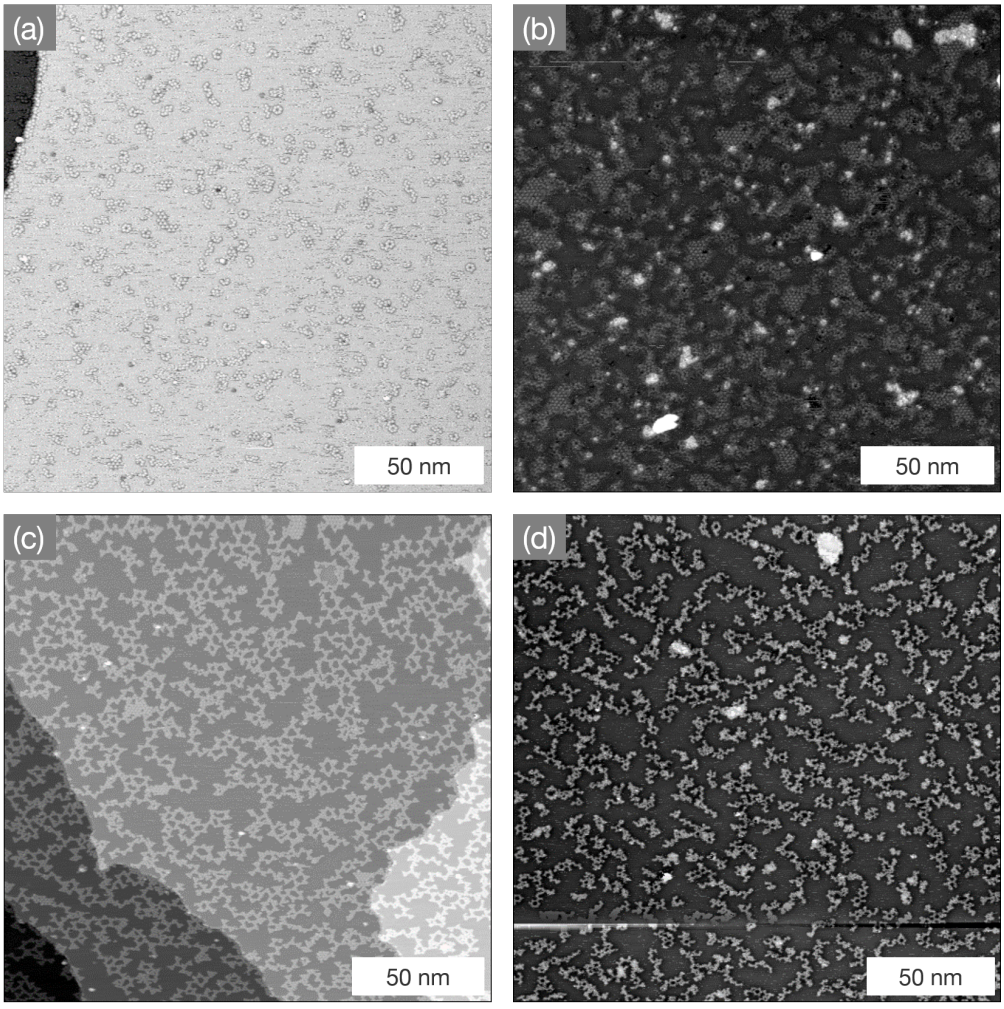

Figure C.1: Overview STM images acquired after room temperature deposition of HATP (upper row) and subsequent annealing to 200 °C (lower row) on (a) / (c) pristine Cu(111), and (b) / (d) nickel-covered Cu(111); (tunneling parameters: (a) 0.80 V, 61 pA; (b) 0.87 V, 92 pA; (c) 0.92 V, 91 pA; (d) 0.91 V, 95 pA)

Hexamer stability

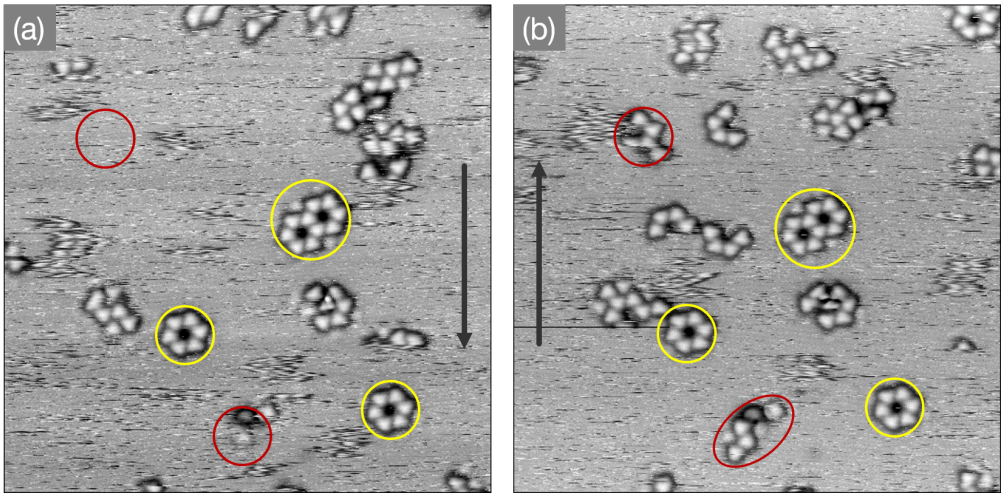

Figure C.2: STM image acquired after room temperature deposition of HATP onto pristine Cu(111). (a) and (b) show two subsequently acquired images, the vertical arrows indicate the slow scan direction; while less compact aggregates (examples marked in red) undergo considerable changes, the cyclic hexamers (marked in yellow) remain unchanged; this indactes overall weak intermolecular interactions as well as a relatively high stability of the hexamers and analogous structures; (image size 30 × 30 nm^2; tunneling parameters: 0.73 V, 53 pA)

Annealing to 200 °C with reduced heating and cooling rates

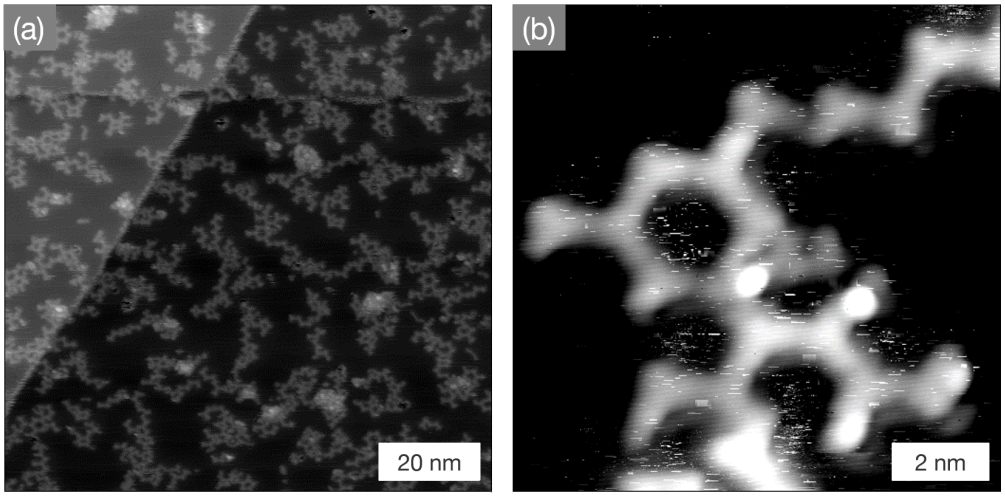

Figure C.3: (a) overview and (b) close-up STM images of HATP on nickel-covered Cu(111) acquired after annealing to 200 °C with a reduced heating and cooling rate of 0.86 °C min^{-1}. No obvious improvement of the structural quality was observed in comparison to experiments with the normally applied heating and cooling rate of 1.66 °C min^{-1}. (tunneling parameters: (a) 2.61 V, 59 pA; (b) 1.28 V, 95 pA)

High temperature annealing

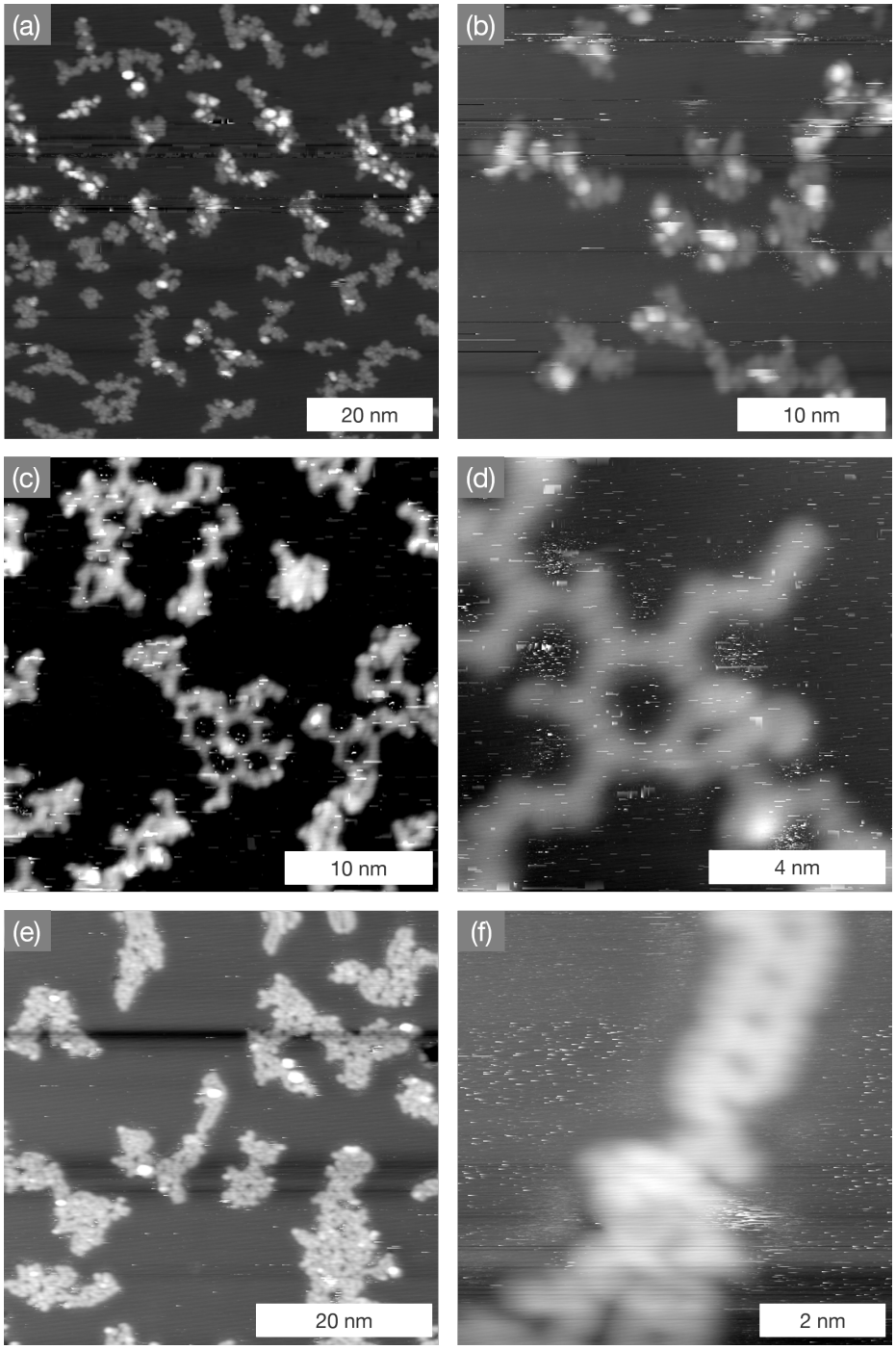

Figure C.4: (a) overview and (b) close-up STM images of HATP on pristine Cu(111) acquired after annealing to 300 °C. The network sizes are relatively small and internal details of these less regular structures were not resolved, presumably due to decomposition of the molecules. (c) overview and (d) close-up STM images of HATP on nickel-covered Cu(111) acquired after annealing to 260 °C, showing still →

intact organometallic networks; (e) overview and (f) close-up STM images of HATP on nickel-covered Cu(111) acquired after annealing to 300 °C. Similar to pristine Cu(111) the structures are mostly irregular due to decomposition of the molecules. (tunneling parameters: (a) 1.72 V, 77 pA; (b) 3.83 V, 88 pA; (c) 2.61 V, 59 pA; (d) 1.28 V, 95 pA; (e) 3.83 V, 88 pA; (f) 1.24 V, 34 pA)

C.2 XPS data: HATP on Cu(111) and on Cu(111) + Ni

High temperature annealing

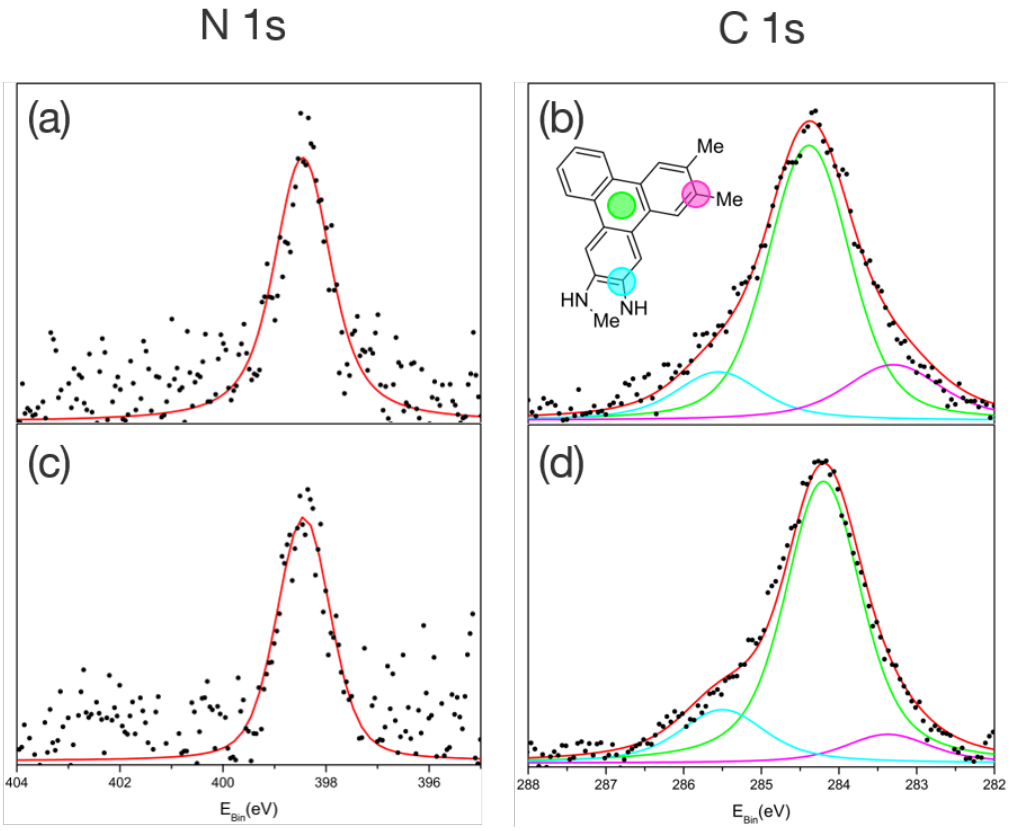

Figure C.5: N 1s (left) and C 1s (right) XP spectra of HATP acquired on (a) / (b) pristine Cu(111), and (c) / (d) nickel-covered Cu(111) after annealing to 300 °C for 10 min. On both surfaces, the high temperature annealing results in intensity losses of both N 1s (pristine Cu(111) ∼43% / Cu(111) + Ni: ∼72%) and C 1s (pristine Cu(111) ∼84% / Cu(111) + Ni: ∼78%). The values in parentheses refer to the intensities measured directly after room temperature deposition. On pristine Cu(111), the relative loss of nitrogen is considerably higher than that of carbon, indicating decomposition of the molecules by dissociation of amino groups. This is in line with the emergence of an additional low E_B shoulder in C 1s at ∼283.2 eV. This shoulder can be interpreted as an organometallic carbon-metal bond (C-M),[42,213] in line with the similarly observed integral shift of the C 1s peak by +0.15 eV to lower E_B as compared to the value after annealing to 200 °C.[29,214] Formation of organometallic bonds indicates dissociation of carbon-nitrogen bonds.

C.3 DFT data: HATP on Cu(111)

competing structural models for the self-assembled hexamers

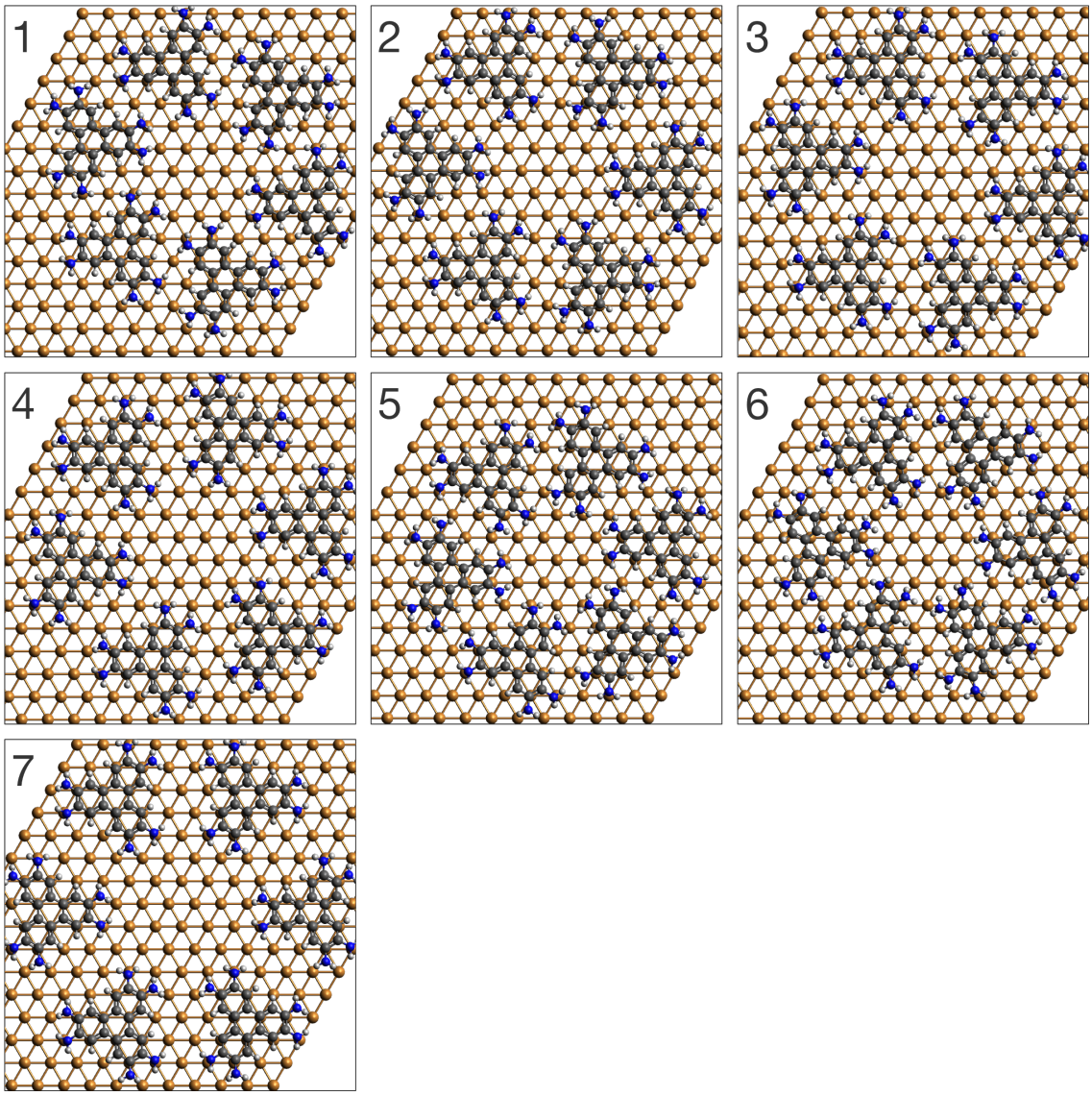

Figure C.6: DFT-optimized geometries for the self-assembled cyclic hexamers of non-deprotonated HATP molecules on pristine Cu(111). The simulations were carried out on a two-layer copper slab, but only one slab is shown for clarity. Seven competing models with comparable intermolecular distances are presented that are all consistent with the experimental result within the experimental error. Moreover, the binding energies of all models are rather similar. These simulations reveal a pronounced adsorption-site preference of HATP molecules, where all aromatic rings of the triphenylene backbone reside above three-fold hollow sites of the Cu(111) surface; all binding energies and structural parameters are summarized in Table C.1.

Dimer

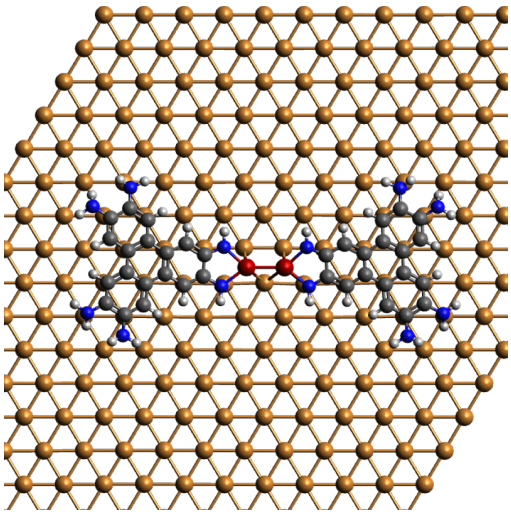

Figure C.7: DFT-optimized geometry of a metal-organic HATP dimer on Cu(111) with an axially aligned Cu_2 coordination center. The center-to-center distance between the two molecules of 1.55 nm in this model is in perfect agreement with the experimental value of (1.55 ± 0.08) nm.

model #	E_{total} (eV/molecule)	$E_{molecule-molecule}$ (eV/molecule)	$d_{(mol-mol)}$ (nm)
1	-4.04	-0.12	2.235
2	-4.08	-0.17	2.352
3-fcc	-4.11	-0.16	2.378
3-hcp	-4.07	-0.16	2.378
4-fcc	-4.11	-0.17	2.399
4-hcp	-4.07	-0.16	2.399
5	-4.00	-0.08	2.165
6-fcc	-3.99	-0.06	2.140
6-hcp	-3.98	-0.07	2.140
7-fcc	-4.13	-0.18	2.591
7-hcp	-4.11	-0.17	2.591

Table C.1: Binding energies and structural parameters for the models of the cyclic hexamers shown in Fig. C.6. E_{total} denotes the total binding energy including contributions from molecule-surface and molecule-molecule interactions (E_{total} = [$E_{hexamer\,on\,Cu}$ - E_{Cu} - 6 E_{HATP}] / 6), whereas $E_{molecule-molecule}$ refers to the intermolecular binding energies ($E_{molecule-molecule}$ = [$E_{hexamer\,in\,vacuum}$ - 6 E_{HATP}] / 6), evaluated for the unchanged structures of the adsorbed species. For the models 3, 4, 6, and 7 all aromatic rings of each of the six molecules reside above similar three-fold hollow sites (either fcc or hcp). In these cases the binding energies were also evaluated for the respective other three-fold hollow site. $d_{mol-mol}$ refers to the center-to-center distance of two diametrically opposed HATP molecules.

References

[1] Novoselov, K. S. Electric Field Effect in Atomically Thin Carbon Films. *Science* **2004**, *306*, 666–669.

[2] Novoselov, K. S.; Jiang, D.; Schedin, F.; Booth, T. J.; Khotkevich, V. V.; Morozov, S. V.; Geim, A. K. Two-dimensional atomic crystals. *Proc. Natl. Acad. Sci. U S A* **2005**, *102*, 10451–10453.

[3] Ferrari, A. C. et al. Science and technology roadmap for graphene, related two-dimensional crystals, and hybrid systems. *Nanoscale* **2015**, *7*, 4598–4810.

[4] Kawai, S.; Saito, S.; Osumi, S.; Yamaguchi, S.; Foster, A. S.; Spijker, P.; Meyer, E. Atomically controlled substitutional boron-doping of graphene nanoribbons. *Nat. Commun.* **2015**, *6*, 8098.

[5] Elias, D. C.; Nair, R. R.; Mohiuddin, T. M. G.; Morozov, S. V.; Blake, P.; Halsall, M. P.; Ferrari, A. C.; Boukhvalov, D. W.; Katsnelson, M. I.; Geim, A. K.; Novoselov, K. S. Control of Graphenes Properties by Reversible Hydrogenation: Evidence for Graphane. *Science* **2009**, *323*, 610–613.

[6] Nair, R. R. et al. Fluorographene: A Two-Dimensional Counterpart of Teflon. *Small* **2010**, *6*, 2877–2884.

[7] Novoselov, K. S.; ko, V. I. F.; Colombo, L.; Gellert, P. R.; Schwab, M. G.; Kim, K. A roadmap for graphene. *Nature* **2012**, *490*, 192–200.

[8] Lackinger, M. Surface-assisted Ullmann coupling. *Chem. Commun.* **2017**, *53*, 7872–7885.

[9] Dong, L.; Gao, Z.; Lin, N. Self-assembly of metal–organic coordination structures on surfaces. *Prog. Surf. Sci.* **2016**, *91*, 101–135.

[10] Lackinger, M. On-surface polymerization - a versatile synthetic route to two-dimensional polymers. *Polym. Int.* **2015**, *64*, 1073–1078.

[11] Auwärter, W.; Écija, D.; Klappenberger, F.; Barth, J. V. Porphyrins at interfaces. *Nat. Chem.* **2015**, *7*, 105–120.

[12] Cai, J.; Ruffieux, P.; Jaafar, R.; Bieri, M.; Braun, T.; Blankenburg, S.; Muoth, M.; Seitsonen, A. P.; Saleh, M.; Feng, X.; Müllen, K.; Fasel, R. Atomically precise bottom-up fabrication of graphene nanoribbons. *Nature* **2010**, *466*, 470–473.

[13] Ruffieux, P.; Wang, S.; Yang, B.; Sánchez-Sánchez, C.; Liu, J.; Dienel, T.; Talirz, L.; Shinde, P.; Pignedoli, C. A.; Passerone, D.; Dumslaff, T.; Feng, X.; Müllen, K.; Fasel, R. On-surface synthesis of graphene nanoribbons with zigzag edge topology. *Nature* **2016**, *531*, 489–492.

[14] Kimouche, A.; Ervasti, M. M.; Drost, R.; Halonen, S.; Harju, A.; Joensuu, P. M.; Sainio, J.; Liljeroth, P. Ultra-narrow metallic armchair graphene nanoribbons. *Nat. Commun.* **2015**, *6*, 10177.

[15] Schlickum, U.; Decker, R.; Klappenberger, F.; Zoppellaro, G.; Klyatskaya, S.; Ruben, M.; Silanes, I.; Arnau, A.; Kern, K.; Brune, H.; Barth, J. V. Metal-Organic Honeycomb Nanomeshes with Tunable Cavity Size. *Nano Lett.* **2007**, *7*, 3813–3817.

[16] Gutzler, R.; Perepichka, D. F. π-Electron Conjugation in Two Dimensions. *J. Am. Chem. Soc.* **2013**, *135*, 16585–16594.

[17] Campbell, M. G.; Sheberla, D.; Liu, S. F.; Swager, T. M.; Dincă, M. Cu3(hexaiminotriphenylene)2 : An Electrically Conductive 2D Metal-organic Framework for Chemiresistive Sensing. *Angew. Chem. Int. Ed.* **2015**, *54*, 4349–4352.

[18] Sakamoto, R.; Takada, K.; Sun, X.; Pal, T.; Tsukamoto, T.; Phua, E. J. H.; Rapakousiou, A.; Hoshiko, K.; Nishihara, H. The coordination nanosheet (CONASH). *Coord. Chem. Rev.* **2016**, *320-321*, 118–128.

[19] Sakamoto, J.; van Heijst, J.; Lukin, O.; Schlüter, A. Two-Dimensional Polymers: Just a Dream of Synthetic Chemists? *Angew. Chem. Int. Ed.* **2009**, *48*, 1030–1069.

[20] Schlüter, A. D.; Sakamoto, J. Putting aromatic compounds to work: Rational synthesis of organic 2D polymers. *Pure Appl. Chem.* **2012**, *84*, 861–867.

[21] Nacci, C.; Hecht, S.; Grill, L. *Advances in Atom and Single Molecule Machines*; Springer International Publishing, 2016; pp 1–21.

[22] Shen, Q.; Gao, H.-Y.; Fuchs, H. Frontiers of on-surface synthesis: From principles to applications. *Nano Today* **2017**, *13*, 77–96.

[23] Bouju, X.; Mattioli, C.; Franc, G.; Pujol, A.; Gourdon, A. Bicomponent Supramolecular Architectures at the Vacuum–Solid Interface. *Chem. Rev.* **2017**, *117*, 1407–1444.

[24] Hammer, B.; Nørskov, J. K. Why gold is the noblest of all the metals. *Nature* **1995**, *376*, 238–240.

[25] Dai, J.; Fan, Q.; Wang, T.; Kuttner, J.; Hilt, G.; Gottfried, J. M.; Zhu, J. The role of the substrate structure in the on-surface synthesis of organometallic and covalent oligophenylene chains. *Phys. Chem. Chem. Phys.* **2016**, *18*, 20627–20634.

[26] Knor, M.; Gao, H.-Y.; Amirjalayer, S.; Studer, A.; Gao, H.; Du, S.; Fuchs, H. Stereoselective formation of coordination polymers with 1,4-diaminonaphthalene on various Cu substrates. *Chem Commun* **2015**, *51*, 10854–10857.

[27] Bieri, M.; Nguyen, M.-T.; Gröning, O.; Cai, J.; Treier, M.; Aït-Mansour, K.; Ruffieux, P.; Pignedoli, C. A.; Passerone, D.; Kastler, M.; Müllen, K.; Fasel, R. Two-Dimensional Polymer Formation on Surfaces: Insight into the Roles of Precursor Mobility and Reactivity. *J. Am. Chem. Soc.* **2010**, *132*, 16669–16676.

[28] Zhang, H.; Franke, J.-H.; Zhong, D.; Li, Y.; Timmer, A.; Arado, O. D.; Mönig, H.; Wang, H.; Chi, L.; Wang, Z.; Müllen, K.; Fuchs, H. Surface Supported Gold-Organic Hybrids: On-Surface Synthesis and Surface Directed Orientation. *Small* **2013**, *10*, 1361–1368.

[29] Pham, T. A.; Song, F.; Nguyen, M.-T.; Li, Z.; Studener, F.; Stöhr, M. Comparing Ullmann Coupling on Noble Metal Surfaces: On-Surface Polymerization of 1,3,6,8-Tetrabromopyrene on Cu(111) and Au(111). *Chem. Eur. J* **2016**, *22*, 5937–5944.

[30] Ullmann, F. Ueber symmetrische Biphenylderivate. *Liebigs Ann. Chem.* **1904**, *332*, 38–81.

[31] Hla, S.-W.; Bartels, L.; Meyer, G.; Rieder, K.-H. Inducing All Steps of a Chemical Reaction with the Scanning Tunneling Microscope Tip: Towards Single Molecule Engineering. *Phys. Rev. Lett.* **2000**, *85*, 2777–2780.

[32] Grill, L.; Dyer, M.; Lafferentz, M., L. Persson; Peters, M. V.; Hecht, S. Nanoarchitectures by covalent assembly of molecular building blocks. *Nat. Nano.* **2007**, *2*, 687–691.

[33] Clark, T.; Hennemann, M.; Murray, J. S.; Politzer, P. Halogen bonding: the σ-hole. *J. Mol. Model.* **2007**, *13*, 291–296.

[34] Politzer, P.; Murray, J. S.; Clark, T. Halogen bonding: an electrostatically-driven highly directional noncovalent interaction. *Phys. Chem. Chem. Phys.* **2010**, *12*, 7748–7757.

[35] Clark, T. σ-Holes. *WIREs Comput. Mol. Sci.* **2012**, *3*, 13–20.

[36] Palma, C.-A. et al. Photoinduced C–C Reactions on Insulators toward Photolithography of Graphene Nanoarchitectures. *J. Am. Chem. Soc.* **2014**, *136*, 4651–4658.

[37] McMillen, D. F.; Golden, D. M. Hydrocarbon Bond Dissociation Energies. *Annu. Rev. Phys. Chem.* **1982**, *33*, 493–532.

[38] Blanksby, S. J.; Ellison, G. B. Bond Dissociation Energies of Organic Molecules. *Acc. Chem. Res.* **2003**, *36*, 255–263.

[39] Hayashi, H.; Yamaguchi, J.; Jippo, H.; Hayashi, R.; Aratani, N.; Ohfuchi, M.; Sato, S.; Yamada, H. Experimental and Theoretical Investigations of Surface-Assisted Graphene Nanoribbon Synthesis Featuring Carbon–Fluorine Bond Cleavage. *ACS Nano* **2017**, *11*, 6204–6210.

[40] Björk, J.; Hanke, F.; Stafström, S. Mechanisms of Halogen-Based Covalent Self-Assembly on Metal Surfaces. *J. Am. Chem. Soc.* **2013**, *135*, 5768–5775.

[41] Björk, J. *On-Surface Synthesis II*; Springer International Publishing, 2018; pp 19–34.

[42] Gutzler, R.; Cardenas, L.; Lipton-Duffin, J.; Garah, M. E.; Dinca, L. E.; Szakacs, C. E.; Fu, C.; Gallagher, M.; Vondráček, M.; Rybachuk, M.; Perepichka, D. F.; Rosei, F. Ullmann-type coupling of brominated tetrathienoanthracene on copper and silver. *Nanoscale* **2014**, *6*, 2660–2668.

[43] Eichhorn, J.; Strunskus, T.; Rastgoo-Lahrood, A.; Samanta, D.; Schmittel, M.; Lackinger, M. On-surface Ullmann polymerization via intermediate organometallic networks on Ag(111). *Chem. Commun.* **2014**, *50*, 7680–7682.

[44] Dong, L.; Wang, S.; Wang, W.; Chen, C.; Lin, T.; Adisoejoso, J.; Lin, N. Transition Metals Trigger On-Surface Ullmann Coupling Reaction: Intermediate, Catalyst and Template. On-Surface Synthesis. Cham, 2016; pp 23–42.

[45] Saywell, A.; Greń, W.; Franc, G.; Gourdon, A.; Bouju, X.; Grill, L. Manipulating the Conformation of Single Organometallic Chains on Au(111). *J. Phys. Chem. C* **2014**, *118*, 1719–1728.

[46] Urgel, J. I.; Hayashi, H.; Giovannantonio, M. D.; Pignedoli, C. A.; Mishra, S.; Deniz, O.; Yamashita, M.; Dienel, T.; Ruffieux, P.; Yamada, H.; Fasel, R. On-Surface Synthesis of Heptacene Organometallic Complexes. *J. Am. Chem. Soc.* **2017**, *139*, 11658–11661.

[47] Zhang, H.; Lin, H.; Sun, K.; Chen, L.; Zagranyarski, Y.; Aghdassi, N.; Duhm, S.; Li, Q.; Zhong, D.; Li, Y.; Müllen, K.; Fuchs, H.; Chi, L. On-Surface Synthesis of Rylene-Type Graphene Nanoribbons. *J. Am. Chem. Soc.* **2015**, *137*, 4022–4025.

[48] Eichhorn, J.; Nieckarz, D.; Ochs, O.; Samanta, D.; Schmittel, M.; Szabelski, P. J.; Lackinger, M. On-Surface Ullmann Coupling: The Influence of Kinetic Reaction Parameters on the Morphology and Quality of Covalent Networks. *ACS Nano* **2014**, *8*, 7880–7889.

[49] Shi, K. J.; Yuan, D. W.; Wang, C. X.; Shu, C. H.; Li, D. Y.; Shi, Z. L.; Wu, X. Y.; Liu, P. N. Ullmann Reaction of Aryl Chlorides on Various Surfaces and the Application in Stepwise Growth of 2D Covalent Organic Frameworks. *Org. Lett.* **2016**, *18*, 1282–1285.

[50] Shi, K. J.; Zhang, X.; Shu, C. H.; Li, D. Y.; Wu, X. Y.; Liu, P. N. Ullmann coupling reaction of aryl chlorides on Au(111) using dosed Cu as a catalyst and the programmed growth of 2D covalent organic frameworks. *Chem. Commun.* **2016**, *52*, 8726–8729.

[51] Schlögl, S.; Heckl, W. M.; Lackinger, M. On-surface radical addition of triply iodinated monomers on Au(111) - the influence of monomer size and thermal post-processing. *Surf. Sci.* **2012**, *606*, 999–1104.

[52] Lafferentz, L.; Eberhardt, V.; DriC.,; Africh, C.; Comelli, G.; Esch, F.; Hecht, S.; Grill, L. Controlling on-surface polymerization by hierarchical and substrate-directed growth. *Nat. Chem.* **2012**, *4*, 215–220.

[53] Steiner, C.; Gebhardt, J.; Ammon, M.; Yang, Z.; Heidenreich, A.; Hammer, N.; Görling, A.; Kivala, M.; Maier, S. Hierarchical on-surface synthesis and electronic structure of carbonyl-functionalized one- and two-dimensional covalent nanoarchitectures. *Nat. Commun.* **2017**, *8*, 14765.

[54] Treier, M.; Pignedoli, C. A.; Laino, T.; Rieger, R.; Müllen, K.; Passerone, D.; Fasel, R. Surface-assisted cyclodehydrogenation provides a synthetic route towards easily processable and chemically tailored nanographenes. *Nat. Chem.* **2010**, *3*, 61–67.

[55] Ammon, M.; Sander, T.; Maier, S. On-Surface Synthesis of Porous Carbon Nanoribbons from Polymer Chains. *J. Am. Chem. Soc.* **2017**, *139*, 12976–12984.

[56] Jiang, L.; Niu, T.; Lu, X.; Dong, H.; Chen, W.; Liu, Y.; Hu, W.; Zhu, D. Low-Temperature, Bottom-Up Synthesis of Graphene via a Radical-Coupling Reaction. *J. Am. Chem. Soc.* **2013**, *135*, 9050–9054.

[57] Sun, Q.; Cai, L.; Ma, H.; Yuan, C.; Xu, W. Dehalogenative Homocoupling of Terminal Alkynyl Bromides on Au(111): Incorporation of Acetylenic Scaffolding into Surface Nanostructures. *ACS Nano* **2016**, *10*, 7023–7030.

[58] Zhao, W.; Dong, L.; Huang, C.; Win, Z. M.; Lin, N. Cu- and Pd-catalyzed Ullmann reaction on a hexagonal boron nitride layer. *Chem. Commun.* **2016**, *52*, 13225–13228.

[59] Morchutt, C.; Björk, J.; Krotzky, S.; Gutzler, R.; Kern, K. Covalent coupling via dehalogenation on Ni(111) supported boron nitride and graphene. *Chem. Commun.* **2015**, *51*, 2440–2443.

[60] Kittelmann, M.; Rahe, P.; Nimmrich, M.; Hauke, C. M.; Gourdon, A.; Kühnle, A. On-Surface Covalent Linking of Organic Building Blocks on a Bulk Insulator. *ACS Nano* **2011**, *5*, 8420–8425.

[61] Rastgoo-Lahrood, A.; Björk, J.; Lischka, M.; Eichhorn, J.; Kloft, S.; Fritton, M.; Strunskus, T.; Samanta, D.; Schmittel, M.; Heckl, W. M.; Lackinger, M. Post-Synthetic Decoupling of On-Surface-Synthesized Covalent Nanostructures from Ag(111). *Angew. Chem. Int. Ed.* **2016**, *55*, 7650–7654.

[62] Rastgoo-Lahrood, A.; Lischka, M.; Eichhorn, J.; Samanta, D.; Schmittel, M.; Heckl, W. M.; Lackinger, M. Reversible intercalation of iodine monolayers between on-surface synthesised covalent polyphenylene networks and Au(111). *Nanoscale* **2017**, *9*, 4995–5001.

[63] Janiak, C. In *Moderne Anorganische Chemie*, 4th ed.; Riedel, E., Ed.; Walter de Gruyter, 2007; p 381–579.

[64] Shchyrba, A.; Wäckerlin, C.; Nowakowski, J.; Nowakowska, S.; Björk, J.; Fatayer, S.; Girovsky, J.; Nijs, T.; Martens, S. C.; Kleibert, A.; Stöhr, M.; Ballav, N.; Jung, T. A.; Gade, L. H. Controlling the Dimensionality of On-Surface Coordination Polymers via Endo- or Exoligation. *J. Am. Chem. Soc.* **2014**, *136*, 9355–9363.

[65] Matena, M.; Björk, J.; Wahl, M.; Lee, T.-L.; Zegenhagen, J.; Gade, L. H.; Jung, T. A.; Persson, M.; Stöhr, M. On-surface synthesis of a two-dimensional porous coordination network: Unraveling adsorbate interactions. *Phys. Rev. B* **2014**, *90*, 125408.

[66] Walch, H.; Dienstmaier, J.; Eder, G.; Gutzler, R.; Schlögl, S.; Sirtl, T.; Das, K.; Schmittel, M.; Lackinger, M. Extended Two-Dimensional Metal–Organic Frameworks Based on Thiolate–Copper Coordination Bonds. *J. Am. Chem. Soc.* **2011**, *133*, 7909–7915.

[67] Rastgoo-Lahrood, A.; Martsinovich, N.; Lischka, M.; Eichhorn, J.; Szabelski, P.; Nieckarz, D.; Strunskus, T.; Das, K.; Schmittel, M.; Heckl, W. M.; Lackinger, M. From Au–Thiolate Chains to Thioether Sierpiński Triangles: The Versatile Surface Chemistry of 1,3,5-Tris(4-mercaptophenyl)benzene on Au(111). *ACS Nano* **2016**, *10*, 10901–10911.

[68] Sirtl, T.; Lischka, M.; Eichhorn, J.; Rastgoo-Lahrood, A.; Strunskus, T.; Heckl, W. M.; Lackinger, M. From Benzenetrithiolate Self-Assembly to Copper Sulfide Adlayers on Cu(111): Temperature-Induced Irreversible and Reversible Phase Transitions. *J. Phys. Chem. C* **2014**, *118*, 3590–3598.

[69] Stepanow, S.; Lin, N.; Barth, J. V.; Kern, K. Surface-Template Assembly of Two-Dimensional Metal-Organic Coordination Networks. *J. Phys. Chem. B* **2006**, *110*, 23472–23477.

[70] Stepanow, S.; Lin, N.; Payer, D.; Schlickum, U.; Klappenberger, F.; Zoppellaro, G.; Ruben, M.; Brune, H.; Barth, J.; Kern, K. Surface-Assisted Assembly of 2D Metal–Organic Networks That Exhibit Unusual Threefold Coordination Symmetry. *Angew. Chem. Int. Ed.* **2007**, *119*, 724–727.

[71] Li, Y.; Xiao, J.; Shubina, T. E.; Chen, M.; Shi, Z.; Schmid, M.; Steinrück, H.-P.; Gottfried, J. M.; Lin, N. Coordination and Metalation Bifunctionality of Cu with 5,10,15,20-Tetra(4-pyridyl)porphyrin: Toward a Mixed-Valence Two-Dimensional Coordination Network. *J. Am. Chem. Soc.* **2012**, *134*, 6401–6408.

[72] Sirtl, T.; Schlögl, S.; Rastgoo-Lahrood, A.; Jelic, J.; Neogi, S.; Schmittel, M.; Heckl, W. M.; Reuter, K.; Lackinger, M. Control of Intermolecular Bonds by Deposition Rates at Room Temperature: Hydrogen Bonds versus Metal Coordination in Trinitrile Monolayers. *J. Am. Chem. Soc.* **2013**, *135*, 691–695.

[73] Pawin, G.; Wong, K.; Kim, D.; Sun, D.; Bartels, L.; Hong, S.; Rahman, T.; Carp, R.; Marsella, M. A Surface Coordination Network Based on Substrate-Derived Metal Adatoms with Local Charge Excess. *Angew. Chem. Int. Ed.* **2008**, *47*, 8442–8445.

[74] Faraggi, M. N.; Jiang, N.; Gonzalez-Lakunza, N.; Langner, A.; Stepanow, S.; Kern, K.; Arnau, A. Bonding and Charge Transfer in Metal–Organic Coordination Networks on Au(111) with Strong Acceptor Molecules. *J. Phys. Chem. C* **2012**, *116*, 24558–24565.

[75] Sun, Q.; Cai, L.; Ma, H.; Yuan, C.; Xu, W. On-surface construction of a metal–organic Sierpiński triangle. *Chem. Commun.* **2015**, *51*, 14164–14166.

[76] Li, L.; Hollinger, J.; Guerin, G.; Seferos, D. S. Synthesis and Network-Like Self-Assembly of Porphyrin-Polyselenophene Complexes. *ChemPhysChem* **2012**, *13*, 4110–4115.

[77] Urgel, J. I.; Écija, D.; Lyu, G.; Zhang, R.; Palma, C.-A.; Auwärter, W.; Lin, N.; Barth, J. V. Quasicrystallinity expressed in two-dimensional coordination networks. *Nat. Chem.* **2016**, *8*, 657–662.

[78] Tait, S. L.; Langner, A.; Lin, N.; Stepanow, S.; Rajadurai, C.; Ruben, M.; Kern, K. One-Dimensional Self-Assembled Molecular Chains on Cu(100): Interplay between Surface-Assisted Coordination Chemistry and Substrate Commensurability. *J. Phys. Chem. C* **2007**, *111*, 10982–10987.

[79] Skomski, D.; Tempas, C. D.; Smith, K. A.; Tait, S. L. Redox-Active On-Surface Assembly of Metal-Organic Chains with Single-Site Pt(II). *J. Am. Chem. Soc.* **2014**, *136*, 9862–9865.

[80] Skomski, D.; Tempas, C. D.; Cook, B. J.; Polezhaev, A. V.; Smith, K. A.; Caulton, K. G.; Tait, S. L. Two- and Three-Electron Oxidation of Single-Site

Vanadium Centers at Surfaces by Ligand Design. *J. Am. Chem. Soc.* **2015**, *137*, 7898–7902.

[81] Bebensee, F.; Svane, K.; Bombis, C.; Masini, F.; Klyatskaya, S.; Besenbacher, F.; Ruben, M.; Hammer, B.; Linderoth, T. R. A Surface Coordination Network Based on Copper Adatom Trimers. *Angew. Chem. Int. Ed.* **2014**, *53*, 12955–12959.

[82] Klappenberger, F. Two-dimensional functional molecular nanoarchitectures – Complementary investigations with scanning tunneling microscopy and X-ray spectroscopy. *Prog. Surf. Sci.* **2014**, *89*, 1–55.

[83] Binnig, G.; Rohrer, H.; Gerber, C.; Weibel, E. Surface Studies by Scanning Tunneling Microscopy. *Phys. Rev. Lett.* **1982**, *49*, 57–61.

[84] Laukkanen, P.; Sadowski, J.; Guina, M. *Semiconductor Research*; Springer Berlin Heidelberg, 2012; pp 1–21.

[85] Fauster, T. *Oberflächenphysik (German Edition)*; Oldenbourg Wissenschaftsverlag, 2013.

[86] Bardeen, J. Tunnelling from a Many-Particle Point of View. *Phys. Rev. Lett.* **1961**, *6*, 57–59.

[87] Yao, N., Wang, Z. L., Eds. *Handbook of Microscopy for Nanotechnology*; Springer US: Boston, MA, 2005; pp 55–112.

[88] Tersoff, J.; Hamann, D. R. Theory of the scanning tunneling microscope. *Phys. Rev. B* **1985**, *31*, 805–813.

[89] Ochs, O. M. Entwicklung einer ultravakuumtauglichen Raster-Tunnel-Mikroskops und Integration in eine bestehende Vakuumanlage. M.Sc. thesis, Hochschule München für angewande Wissenschaft - FH, 2013.

[90] Schmucker, S.; Kumar, N.; Abelson, J.; Daly, S.; Girolami, G.; Bischof, M.; Jaeger, D.; Reidy, R.; Gorman, B.; Alexander, J.; Ballard, J.; Randall, J.; Lyding, J. Field-directed sputter sharpening for tailored probe materials and atomic-scale lithography. *Nat. Commun.* **2012**, *3*, 935.

[91] Gutzler, R.; Heckl, W.; Lackinger, M. Combination of a Knudsen effusion cell with a quartz crystal microbalance: In situ measurement of molecular evaporation rates with a fully functional deposition source. *Rev. Sci. Instrum.* **2010**, *81*, 015108.

[92] Seah, M. P.; Dench, W. A. Quantitative electron spectroscopy of surfaces: A standard data base for electron inelastic mean free paths in solids. *Surf. Interface Anal.* **1979**, *1*, 2–11.

[93] Willmott, P. *An Introduction to Synchrotron Radiation*; John Wiley & Sons, Ltd, 2011.

[94] Hertz, H. Ueber einen Einfluss des ultravioletten Lichtes auf die electrische Entladung. *Ann. Phys.* **1887**, *267*, 983–1000.

[95] Einstein, A. Über einen die Erzeugung und Verwandlung des Lichtes betreffenden heuristischen Gesichtspunkt. *Ann. Phys.* **1905**, *322*, 132–148.

[96] Siegbahn, K. M. *Electron Spectroscopy for Atoms, Molecules and Condensed Matter*; Elsevier Publishing Company, 1981; Chapter Nobel Lecture.

[97] Hofmann, S. *Auger- and X-Ray Photoelectron Spectroscopy in Materials Science*; Springer Berlin Heidelberg, 2013.

[98] Hähner, G. Near edge X-ray absorption fine structure spectroscopy as a tool to probe electronic and structural properties of thin organic films and liquids. *Chem. Soc. Rev.* **2006**, *35*, 1244–1255.

[99] Chiang, T.-C.; Kaindl, G.; Mandel, T. Layer-resolved shifts of photoemission and Auger spectra from physisorbed rare-gas multilayers. *Phys. Rev. B* **1986**, *33*, 695–711.

[100] Kohiki, S.; Oki, K.; Konishi, F. Extra-atomic relaxation effect on the binding energy of reference gold in X-ray photoelectron spectroscopy. *Anal. Sci.* **1985**, *1*, 115–117.

[101] Goddard, P.; Schwaha, K.; Lambert, R. Adsorption-desorption properties and surface structural chemistry of bromine on clean and sodium-dosed Ag(111). *Surf. Sci.* **1978**, *71*, 351–363.

[102] Stöhr, J. *NEXAFS Spectroscopy*; Springer Berlin Heidelberg, 1992.

[103] Reiß, S.; Krumm, H.; Niklewski, A.; Staemmler, V.; Wöll, C. The adsorption of acenes on rutile TiO_2(110): A multi-technique investigation. *J. Chem. Phys.* **2002**, *116*, 7704–7713.

[104] Hänel, K.; Söhnchen, S.; Lukas, S.; Beernik, G.; Birkner, A.; Strunskus, T.; Witte, G.; Wöll, C. Organic molecular-beam deposition of perylene on Cu(110): Results from near-edge x-ray absorption spectroscopy, x-ray photoelectron spectroscopy, and atomic force microscopy. *J. Mater. Res.* **2004**, *19*, 2049–2056.

[105] Oji, H.; Mitsumoto, R.; Ito, E.; Ishii, H.; Ouchi, Y.; Seki, K.; Yokoyama, T.; Ohta, T.; Kosugi, N. Core hole effect in NEXAFS spectroscopy of polycyclic aromatic hydrocarbons: Benzene, chrysene, perylene, and coronene. *J. Chem. Phys.* **1998**, *109*, 10409–10418.

[106] Söhnchen, S.; Lukas, S.; Witte, G. Epitaxial growth of pentacene films on Cu(110). *J. Chem. Phys.* **2004**, *121*, 525–534.

[107] Zwaneveld, N. A. A.; Pawlak, R.; Abel, M.; Catalin, D.; Gigmes, D.; Bertin, D.; Porte, L. Organized Formation of 2D Extended Covalent Organic Frameworks at Surfaces. *J. Am. Chem. Soc.* **2008**, *130*, 6678–6679.

[108] Colson, J. W.; Dichtel, W. R. Rationally synthesized two-dimensional polymers. *Nat. Chem.* **2013**, *5*, 453–465.

[109] Perepichka, D. F.; Rosei, F. CHEMISTRY: Extending Polymer Conjugation into the Second Dimension. *Science* **2009**, *323*, 216–217.

[110] Walch, H.; Gutzler, R.; Sirtl, T.; Eder, G.; Lackinger, M. Material- and Orientation-Dependent Reactivity for Heterogeneously Catalyzed Carbon-Bromine Bond Homolysis. *J. Phys. Chem. C* **2010**, *114*, 12604–12609.

[111] Gutzler, R.; Walch, H.; Eder, G.; Kloft, S.; Heckl, W. M.; Lackinger, M. Surface mediated synthesis of 2D covalent organic frameworks: 1,3,5-tris(4-bromophenyl)benzene on graphite(001), Cu(111), and Ag(110). *Chem. Commun.* **2009**, *0*, 4456–4458.

[112] Lipton-Duffin, J. A.; Ivasenko, O.; Perepichka, D. F.; Rosei, F. Synthesis of Polyphenylene Molecular Wires by Surface-Confined Polymerization. *Small* **2009**, *5*, 592–597.

[113] Bieri, M.; Treier, M.; Cai, J.; Aït-Mansour, K.; Ruffieux, P.; Gröning, O.; Gröning, P.; Kastler, M.; Rieger, R.; Feng, X.; Müllen, K.; Fasel, R. Porous graphenes: two-dimensional polymer synthesis with atomic precision. *Chem. Commun.* **2009**, *0*, 6919–6921.

[114] Jiang, J.-X.; Trewin, A.; Adams, D. J.; Cooper, A. I. Band gap engineering in fluorescent conjugated microporous polymers. *Chem. Sci.* **2011**, *2*, 1777.

[115] Stylianou, K. C.; Heck, R.; Chong, S. Y.; Bacsa, J.; Jones, J. T. A.; Khimyak, Y. Z.; Bradshaw, D.; Rosseinsky, M. J. A Guest-Responsive Fluorescent 3D Microporous Metal-Organic Framework Derived from a Long-Lifetime Pyrene Core. *J. Am. Chem. Soc.* **2010**, *132*, 4119–4130.

[116] Guo, L.; Cao, D. Color tunable porous organic polymer luminescent probes for selective sensing of metal ions and nitroaromatic explosives. *J. Mater. Chem. C* **2015**, *3*, 8490–8494.

[117] Kaposi, T.; Joshi, S.; Hoh, T.; Wiengarten, A.; Seufert, K.; Paszkiewicz, M.; Klappenberger, F.; Ecija, D.; Đorđević, L.; Marangoni, T.; Bonifazi, D.; Barth, J. V.; Auwärter, W. Supramolecular Spangling, Crocheting, and Knitting of Functionalized Pyrene Molecules on a Silver Surface. *ACS Nano* **2016**, *10*, 7665–7674.

[118] Smerieri, M.; Píš, I.; Ferrighi, L.; Nappini, S.; Lusuan, A.; Valentin, C. D.; Vaghi, L.; Papagni, A.; Cattelan, M.; Agnoli, S.; Magnano, E.; Bondino, F.; Savio, L. Synthesis of graphene nanoribbons with a defined mixed edge-site sequence by surface assisted polymerization of (1,6)-dibromopyrene on Ag(110). *Nanoscale* **2016**, *8*, 17843–17853.

[119] Pham, T. A.; Song, F.; Nguyen, M.-T.; Stöhr, M. Self-assembly of pyrene derivatives on Au(111): substituent effects on intermolecular interactions. *Chem. Commun.* **2014**, *50*, 14089–14092.

[120] Rastgoo-Lahrood, A.; Björk, J.; Heckl, W. M.; Lackinger, M. 1,3-Diiodobenzene on Cu(111) – an exceptional case of on-surface Ullmann coupling. *Chem. Commun.* **2015**, *51*, 13301–13304.

[121] Smykalla, L.; Shukrynau, P.; Korb, M.; Lang, H.; Hietschold, M. Surface-confined 2D polymerization of a brominated copper-tetraphenylporphyrin on Au(111). *Nanoscale* **2015**, *7*, 4234–4241.

[122] Eder, G.; Smith, E. F.; Cebula, I.; Heckl, W. M.; Beton, P. H.; Lackinger, M. Solution Preparation of Two-Dimensional Covalently Linked Networks by Polymerization of 1,3,5-Tri(4-iodophenyl)benzene on Au(111). *ACS Nano* **2013**, *7*, 3014–3021.

[123] Migani, A.; Illas, F. A Systematic Study of the Structure and Bonding of Halogens on Low-Index Transition Metal Surfaces. *J. Phys. Chem. B* **2006**, *110*, 11894–11906.

[124] Frank, K. H.; Yannoulis, P.; Dudde, R.; Koch, E. E. Unoccupied molecular orbitals of aromatic hydrocarbons adsorbed on Ag(111). *J. Chem. Phys.* **1988**, *89*, 7569–7576.

[125] Ågren, H.; Vahtras, O.; Carravetta, V. Near-edge core photoabsorption in polyacenes: model molecules for graphite. *Chem. Phys.* **1995**, *196*, 47–58.

[126] Lucas, L. A.; DeLongchamp, D. M.; Richter, L. J.; Kline, R. J.; Fischer, D. A.; Kaafarani, B. R.; Jabbour, G. E. Thin Film Microstructure of a Solution Processable Pyrene-Based Organic Semiconductor. *Chem. Mater.* **2008**, *20*, 5743–5749.

[127] Sandi, G.; Song, K.; Carrado, K. A.; Winans, R. E. A NEXAFS determination of the electronic structure of carbons for lithium-ion cells. *Carbon* **1998**, *36*, 1755–1758.

[128] Sandi, G. Raman and NEXAFS Spectroscopy Characterization of Templated-Carbon Anodes. *J. New Mater. Electrochem. Syst.* **2003**, *6*, 181 – 189.

[129] Kakavandi, R.; Savu, S.-A.; Sorace, L.; Rovai, D.; Mannini, M.; Casu, M. B. Core-Hole Screening, Electronic Structure, and Paramagnetic Character in Thin Films of Organic Radicals Deposited on SiO2/Si(111). *J. Phys. Chem. C* **2014**, *118*, 8044–8049.

[130] Kakavandi, R.; Ravat, P.; Savu, S.-A.; Borozdina, Y. B.; Baumgarten, M.; Casu, M. B. Electronic Structure and Stability of Fluorophore–Nitroxide Radicals from Ultrahigh Vacuum to Air Exposure. *ACS Appl. Mater. Interfaces* **2015**, *7*, 1685–1692.

[131] Stöhr, J.; Outka, D. A. Determination of molecular orientations on surfaces from the angular dependence of near-edge x-ray-absorption fine-structure spectra. *Phys. Rev. B* **1987**, *36*, 7891–7905.

[132] Gunlycke, D.; Li, J.; Mintmire, J. W.; White, C. T. Edges Bring New Dimension to Graphene Nanoribbons. *Nano Lett.* **2010**, *10*, 3638–3642.

[133] Abild-Pedersen, F.; Greeley, J.; Studt, F.; Rossmeisl, J.; Munter, T. R.; Moses, P. G.; Skúlason, E.; Bligaard, T.; Nørskov, J. K. Scaling Properties of Adsorption Energies for Hydrogen-Containing Molecules on Transition-Metal Surfaces. *Phys. Rev. Lett.* **2007**, *99*, 016105.

[134] Seah, M. P. AES: Energy calibration of electron spectrometers. I–An absolute, traceable energy calibration and the provision of atomic reference line energies. *Surf. Interface Anal.* **1990**, *15*, 293–308.

[135] Johansson, G.; Hedman, J.; Berndtsson, A.; Klasson, M.; Nilsson, R. Calibration of electron spectra. *J. Electron Spectrosc. Relat. Phenom.* **1973**, *2*, 295–317.

[136] Kresse, G.; Furthmüller, J. Efficient iterative schemes forab initiototal-energy calculations using a plane-wave basis set. *Phys. Rev. B* **1996**, *54*, 11169–11186.

[137] Blöchl, P. E. Projector augmented-wave method. *Phys. Rev. B* **1994**, *50*, 17953–17979.

[138] Perdew, J. P.; Burke, K.; Ernzerhof, M. Generalized Gradient Approximation Made Simple. *Phys. Rev. Lett.* **1996**, *77*, 3865–3868.

[139] Henkelman, G.; Uberuaga, B. P.; Jónsson, H. A climbing image nudged elastic band method for finding saddle points and minimum energy paths. *J. Chem. Phys.* **2000**, *113*, 9901–9904.

[140] Kästner, J.; Sherwood, P. Superlinearly converging dimer method for transition state search. *J. Chem. Phys.* **2008**, *128*, 014106.

[141] Barth, J. V.; Costantini, G.; Kern, K. Engineering atomic and molecular nanostructures at surfaces. *Nature* **2005**, *437*, 671–679.

[142] Barth, J. V. Molecular Architectonic on Metal Surfaces. *Annu. Rev. Phys. Chem.* **2007**, *58*, 375–407.

[143] Yuan, W. Z.; Shen, X. Y.; Zhao, H.; Lam, J. W. Y.; Tang, L.; Lu, P.; Wang, C.; Liu, Y.; Wang, Z.; Zheng, Q.; Sun, J. Z.; Ma, Y.; Tang, B. Z. Crystallization-Induced Phosphorescence of Pure Organic Luminogens at Room Temperature. *J. Phys. Chem. C* **2010**, *114*, 6090–6099.

[144] Wurster, B.; Grumelli, D.; Hötger, D.; Gutzler, R.; Kern, K. Driving the Oxygen Evolution Reaction by Nonlinear Cooperativity in Bimetallic Coordination Catalysts. *J. Am. Chem. Soc.* **2016**, *138*, 3623–3626.

[145] Gutzler, R.; Stepanow, S.; Grumelli, D.; Lingenfelder, M.; Kern, K. Mimicking Enzymatic Active Sites on Surfaces for Energy Conversion Chemistry. *Acc. Chem. Res.* **2015**, *48*, 2132–2139.

[146] DiGiovannantonio, M.; Contini, G. Reversibility and intermediate steps as key tools for the growth of extended ordered polymers via on-surface synthesis. *J. Phys. Condens. Matter* **2018**, *30*, 093001.

[147] Judd, C. J.; Haddow, S. L.; Champness, N. R.; Saywell, A. Ullmann Coupling Reactions on Ag(111) and Ag(110); Substrate Influence on the Formation of Covalently Coupled Products and Intermediate Metal-Organic Structures. *Sci. Rep.* **2017**, *7*, 14541.

[148] Chen, Z.; Molina-Jirón, C.; Klyatskaya, S.; Klappenberger, F.; Ruben, M. 1D and 2D Graphdiynes: Recent Advances on the Synthesis at Interfaces and Potential Nanotechnological Applications. *Ann. Phys.* **2017**, *529*, 1700056.

[149] Kuang, G.; Chen, S. Z.; Yan, L.; Chen, K. Q.; Shang, X.; Liu, P. N.; Lin, N. Negative Differential Conductance in Polyporphyrin Oligomers with Nonlinear Backbones. *J. Am. Chem. Soc.* **2018**, *140*, 570–573.

[150] Wagner, P.; Ewels, C. P.; Adjizian, J.-J.; Magaud, L.; Pochet, P.; Roche, S.; Lopez-Bezanilla, A.; Ivanovskaya, V. V.; Yaya, A.; Rayson, M.; Briddon, P.; Humbert, B. Band Gap Engineering via Edge-Functionalization of Graphene Nanoribbons. *J. Phys. Chem. C* **2013**, *117*, 26790–26796.

[151] Schmidt, C.; Breuer, T.; Wippermann, S.; Schmidt, W. G.; Witte, G. Substrate Induced Thermal Decomposition of Perfluoro-Pentacene Thin Films on the Coinage Metals. *J. Phys. Chem. C* **2012**, *116*, 24098–24106.

[152] Riley, K. E.; Murray, J. S.; Fanfrlík, J.; Řezáč, J.; Solá, R. J.; Concha, M. C.; Ramos, F. M.; Politzer, P. Halogen bond tunability I: the effects of aromatic fluorine substitution on the strengths of halogen-bonding interactions involving chlorine, bromine, and iodine. *J. Mol. Model.* **2011**, *17*, 3309–3318.

[153] Kawai, S.; Sadeghi, A.; Xu, F.; Peng, L.; Orita, A.; Otera, J.; Goedecker, S.; Meyer, E. Extended Halogen Bonding between Fully Fluorinated Aromatic Molecules. *ACS Nano* **2015**, *9*, 2574–2583.

[154] Píš, I.; Ferrighi, L.; Nguyen, T. H.; Nappini, S.; Vaghi, L.; Basagni, A.; Magnano, E.; Papagni, A.; Sedona, F.; Valentin, C. D.; Agnoli, S.; Bondino, F. Surface-Confined Polymerization of Halogenated Polyacenes: The Case of Dibromotetracene on Ag(110). *J. Phys. Chem. C* **2016**, *120*, 4909–4918.

[155] Clark, D. T.; Kilcast, D.; Musgrave, W. K. R. Molecular core binding energies for some monosubstituted benzenes, as determined by X-ray photoelectron spectroscopy. *J. Chem. Soc. D* **1971**, *0*, 516b–518.

[156] Clark, D.; Kilcast, D.; Adams, D.; Musgrave, W. An ESCA study of the molecular core binding energies of the fluorobenzenes. *J. Electron Spectrosc. Relat. Phenom.* **1972**, *1*, 227 – 250.

[157] Okudaira, K. K.; Ohara, K.; Setoyama, H.; Suzuki, T.; Sakamoto, Y.; Imamura, M.; Hasegawa, S.; Mase, K.; Ueno, N. Excited states of perfluorinated oligo(p-phenylene) by inner-shell excitation. *Nucl. Instrum. Methods Phys. Res., Sect. B* **2003**, *199*, 265–269.

[158] Mainka, C.; Bagus, P. S.; Schertel, A.; Strunskus, T.; Grunze, M.; Wöll, C. Linear dichroism in X-ray absorption spectroscopy of strongly chemisorbed planar molecules: role of adsorption induced rehybridisations. *Surf. Sci.* **1995**, *341*, L1055–L1060.

[159] Ramsey, M. G.; Netzer, F. P.; Steinmüller, D.; Steinmüller-Nethl, D.; Lloyd, D. R. Evolution of the core and unoccupied orbitals of biphenyl and bithiophene on Cs doping. *J. Chem. Phys.* **1992**, *97*, 4489–4495.

[160] Fan, Q.; Wang, C.; Liu, L.; Han, Y.; Zhao, J.; Zhu, J.; Kuttner, J.; Hilt, G.; Gottfried, J. M. Covalent, Organometallic, and Halogen-Bonded Nanomeshes from Tetrabromo-Terphenyl by Surface-Assisted Synthesis on Cu(111). *J. Phys. Chem. C* **2014**, *118*, 13018–13025.

[161] Duhm, S.; Hosoumi, S.; Salzmann, I.; Gerlach, A.; Oehzelt, M.; Wedl, B.; Lee, T.-L.; Schreiber, F.; Koch, N.; Ueno, N.; Kera, S. Influence of intramolecular polar bonds on interface energetics in perfluoro-pentacene on Ag(111). *Phys. Rev. B* **2010**, *81*, 045418.

[162] Bieri, M.; Blankenburg, S.; Kivala, M.; Pignedoli, C. A.; Ruffieux, P.; Müllen, K.; Fasel, R. Surface-supported 2D heterotriangulene polymers. *Chem. Commun.* **2011**, *47*, 10239–10241.

[163] Grein, F. Twist Angles and Rotational Energy Barriers of Biphenyl and Substituted Biphenyls. *J. Phys. Chem. A* **2002**, *106*, 3823–3827.

[164] Koch, N.; Gerlach, A.; Duhm, S.; Glowatzki, H.; Heimel, G.; Vollmer, A.; Sakamoto, Y.; Suzuki, T.; Zegenhagen, J.; Rabe, J. P.; Schreiber, F. Adsorption-Induced Intramolecular Dipole: Correlating Molecular Conformation and Interface Electronic Structure. *J. Am. Chem. Soc.* **2008**, *130*, 7300–7304.

[165] Beggan, J. P.; Boyle, N. M.; Pryce, M. T.; Cafolla, A. A. Surface-confined Ullmann coupling of thiophene substituted porphyrins. *Nanotechnology* **2015**, *26*, 365602.

[166] Sakamoto, Y.; Suzuki, T.; Miura, A.; Fujikawa, H.; Tokito, S.; Taga, Y. Synthesis, Characterization, and Electron-Transport Property of Perfluorinated Phenylene Dendrimers. *J. Am. Chem. Soc.* **2000**, *122*, 1832–1833.

[167] Leroux, F.; Simon, R.; Nicod, N. A Highly Efficient Low Temperature Modification of the Classical Ullmann Reaction. *Lett. Org. Chem.* **2006**, *3*, 948–954.

[168] Blum, V.; Gehrke, R.; Hanke, F.; Havu, P.; Havu, V.; Ren, X.; Reuter, K.; Scheffler, M. Ab initio molecular simulations with numeric atom-centered orbitals. *Comput. Phys. Commun.* **2009**, *180*, 2175–2196.

[169] Ruiz, V. G.; Liu, W.; Zojer, E.; Scheffler, M.; Tkatchenko, A. Density-Functional Theory with Screened van der Waals Interactions for the Modeling of Hybrid Inorganic-Organic Systems. *Phys. Rev. Lett.* **2012**, *108*, 146103.

[170] Besley, N. A.; Gilbert, A. T. B.; Gill, P. M. W. Self-consistent-field calculations of core excited states. *J. Chem. Phys.* **2009**, *130*, 124308.

[171] Gilbert, A. T. B.; Besley, N. A.; Gill, P. M. W. Self-Consistent Field Calculations of Excited States Using the Maximum Overlap Method (MOM). *J. Phys. Chem. A* **2008**, *112*, 13164–13171.

[172] Sakamoto, R.; Takada, K.; Pal, T.; Maeda, H.; Kambe, T.; Nishihara, H. Coordination nanosheets (CONASHs): strategies, structures and functions. *Chem. Commun.* **2017**, *53*, 5781–5801.

[173] Bauer, T.; Zheng, Z.; Renn, A.; Enning, R.; Stemmer, A.; Sakamoto, J.; Schlüter, A. D. Synthesis of Free-Standing, Monolayered Organometallic Sheets at the Air/Water Interface. *Angew. Chem. Int. Ed.* **2011**, *50*, 7879–7884.

[174] Chen, L.; Kim, J.; Ishizuka, T.; Honsho, Y.; Saeki, A.; Seki, S.; Ihee, H.; Jiang, D. Noncovalently Netted, Photoconductive Sheets with Extremely High Carrier Mobility and Conduction Anisotropy from Triphenylene-Fused Metal Trigon Conjugates. *J. Am. Chem. Soc.* **2009**, *131*, 7287–7292.

[175] Dong, R.; Zheng, Z.; Tranca, D.; Zhang, J.; Chandrasekhar, N.; Liu, S.; Zhuang, X.; Seifert, G.; Feng, X. Immobilizing Molecular Metal Dithiolene-Diamine Complexes on 2D Metal-Organic Frameworks for Electrocatalytic H2 Production. *Chem. Eur. J* **2016**, *23*, 2255–2260.

[176] Dong, R.; Pfeffermann, M.; Liang, H.; Zheng, Z.; Zhu, X.; Zhang, J.; Feng, X. Large-Area, Free-Standing, Two-Dimensional Supramolecular Polymer Single-Layer Sheets for Highly Efficient Electrocatalytic Hydrogen Evolution. *Angew. Chem. Int. Ed.* **2015**, *54*, 12058–12063.

[177] Sheberla, D.; Bachman, J. C.; Elias, J. S.; Sun, C.-J.; Shao-Horn, Y.; Dincă, M. Conductive MOF electrodes for stable supercapacitors with high areal capacitance. *Nat. Mater* **2016**, *16*, 220–224.

[178] Sheberla, D.; Sun, L.; Blood-Forsythe, M. A.; Er, S.; Wade, C. R.; Brozek, C. K.; Aspuru-Guzik, A.; Dincă, M. High Electrical Conductivity in Ni3(2,3,6,7,10,11-hexaiminotriphenylene)2, a Semiconducting Metal–Organic Graphene Analogue. *J. Am. Chem. Soc.* **2014**, *136*, 8859–8862.

[179] Giovanelli, L.; Ourdjini, O.; Abel, M.; Pawlak, R.; Fujii, J.; Porte, L.; Themlin, J.-M.; Clair, S. Combined Photoemission Spectroscopy and Scanning Tunneling Microscopy Study of the Sequential Dehydrogenation of Hexahydroxytriphenylene on Ag(111). *J. Phys. Chem. C* **2014**, *118*, 14899–14904.

[180] Coratger, R.; Calmettes, B.; Abel, M.; Porte, L. STM observations of the first polymerization steps between hexahydroxy-tri-phenylene and benzene-diboronic acid molecules. *Surf. Sci.* **2011**, *605*, 831–837.

[181] Herebian, D.; Bothe, E.; Neese, F.; Weyhermüller, T.; Wieghardt, K. Molecular and Electronic Structures of Bis-(o-diiminobenzosemiquinonato)metal(II) Complexes (Ni, Pd, Pt), Their Monocations and -Anions, and of Dimeric Dications Containing Weak Metal-Metal Bonds. *J. Am. Chem. Soc.* **2003**, *125*, 9116–9128.

[182] Miner, E. M.; Fukushima, T.; Sheberla, D.; Sun, L.; Surendranath, Y.; Dincă, M. Electrochemical oxygen reduction catalysed by Ni3(hexaiminotriphenylene)2. *Nat. Commun.* **2016**, *7*, 10942.

[183] Yang, C.; Schellhammer, K. S.; Ortmann, F.; Sun, S.; Dong, R.; Karakus, M.; Mics, Z.; Löffler, M.; Zhang, F.; Zhuang, X.; Cánovas, E.; Cuniberti, G.; Bonn, M.; Feng, X. Coordination Polymer Framework Based On-Chip Micro-Supercapacitors with AC Line-Filtering Performance. *Angew. Chem. Int. Ed.* **2017**, *56*, 3920–3924.

[184] Huang, X.; Zhang, S.; Liu, L.; Yu, L.; Chen, G.; Xu, W.; Zhu, D. Superconductivity in a Copper(II)-Based Coordination Polymer with Perfect Kagome Structure. *Angew. Chem. Int. Ed.* **2017**, *57*, 146–150.

[185] Murray, D. J.; Patterson, D. D.; Payamyar, P.; Bhola, R.; Song, W.; Lackinger, M.; Schlüter, A. D.; King, B. T. Large Area Synthesis of a Nanoporous Two-Dimensional Polymer at the Air/Water Interface. *J. Am. Chem. Soc.* **2015**, *137*, 3450–3453.

[186] Dienstmaier, J. F.; Medina, D. D.; Dogru, M.; Knochel, P.; Bein, T.; Heckl, W. M.; Lackinger, M. Isoreticular Two-Dimensional Covalent Organic Frameworks Synthesized by On-Surface Condensation of Diboronic Acids. *ACS Nano* **2012**, *6*, 7234–7242.

[187] Spitzer, S.; Rastgoo-Lahrood, A.; Macknapp, K.; Ritter, V.; Sotier, S.; Heckl, W. M.; Lackinger, M. Solvent-free on-surface synthesis of boroxine COF monolayers. *Chem. Commun.* **2017**, *53*, 5147–5150.

[188] Müller, K.; Moreno-López, J. C.; Gottardi, S.; Meinhardt, U.; Yildirim, H.; Kara, A.; Kivala, M.; Stöhr, M. Cyano-Functionalized Triarylamines on Coinage Metal Surfaces: Interplay of Intermolecular and Molecule-Substrate Interactions. *Chem. Eur. J* **2015**, *22*, 581–589.

[189] Schlickum, U.; Decker, R.; Klappenberger, F.; Zoppellaro, G.; Klyatskaya, S.; Auwärter, W.; Neppl, S.; Kern, K.; Brune, H.; Ruben, M.; Barth, J. V. Chiral Kagomé Lattice from Simple Ditopic Molecular Bricks. *J. Am. Chem. Soc.* **2008**, *130*, 11778–11782.

[190] Jiang, L.; Papageorgiou, A. C.; Oh, S. C.; Özge Sağlam,; Reichert, J.; Duncan, D. A.; Zhang, Y.-Q.; Klappenberger, F.; Guo, Y.; Allegretti, F.; More, S.; Bhosale, R.; Mateo-Alonso, A.; Barth, J. V. Synthesis of Pyrene-Fused Pyrazaacenes on Metal Surfaces: Toward One-Dimensional Conjugated Nanostructures. *ACS Nano* **2016**, *10*, 1033–1041.

[191] Huang, S. X.; Fischer, D. A.; Gland, J. L. Aniline Adsorption, Hydrogenation, and Hydrogenolysis on the Ni(100) Surface. *J. Chem. Phys.* **1996**, *100*, 10223–10234.

[192] Xu, X.; Friend, C. M. The adsorption and reactions of aniline on Rh(111). *J. Vac. Sci. Technol. A* **1991**, *9*, 1599–1603.

[193] Jones, T. S.; Ashton, M. R.; Richardson, N. V.; Mack, R. G.; Unertl, W. N. The interaction of the polyimide precursors PMDA (1,2,4,5-benzenetetracarboxylic anhydride) and m-PDA (1,3-phenylenediamine) with Ni(110). *J. Vac. Sci. Technol. A* **1990**, *8*, 2370–2375.

[194] Lin, Y.-P.; Ourdjini, O.; Giovanelli, L.; Clair, S.; Faury, T.; Ksari, Y.; Themlin, J.-M.; Porte, L.; Abel, M. Self-Assembled Melamine Monolayer on Cu(111). *J. Phys. Chem. C* **2013**, *117*, 9895–9902.

[195] Hwang, J.; Kim, Y.; Ahn, Y. Fabrication of a Superhydrophobic Triphenylene Ether Derivative Film on an Al Plate. *Bull. Korean Chem. Soc.* **2014**, *35*, 2831–2834.

[196] Solomon, J.; Madix, R.; Stöhr, J. Orientation and absolute coverage of benzene, aniline, and phenol on Ag(110) determined by NEXAFS and XPS. *Surf. Sci.* **1991**, *255*, 12–30.

[197] Papageorgiou, A. C.; Fischer, S.; Reichert, J.; Diller, K.; Blobner, F.; Klappenberger, F.; Allegretti, F.; Seitsonen, A. P.; Barth, J. V. Chemical Transformations Drive Complex Self-Assembly of Uracil on Close-Packed Coinage Metal Surfaces. *ACS Nano* **2012**, *6*, 2477–2486.

[198] Diller, K.; Klappenberger, F.; Marschall, M.; Hermann, K.; Nefedov, A.; Wöll, C.; Barth, J. V. Self-metalation of 2H-tetraphenylporphyrin on Cu(111): An x-ray spectroscopy study. *J. Chem. Phys.* **2012**, *136*, 014705.

[199] Masini, F.; Ning, Y.; Li, Z.; Lægsgaard, E.; Besenbacher, F.; Linderoth, T. R. Adsorption of the organic salt TAB(HCl)4 on Cu(111) studied using STM and XPS. *Chem. Commun.* **2013**, *49*, 8665.

[200] Liu, W.; Ruiz, V. G.; Zhang, G.-X.; Santra, B.; Ren, X.; Scheffler, M.; Tkatchenko, A. Structure and energetics of benzene adsorbed on transition-metal surfaces: density-functional theory with van der Waals interactions including collective substrate response. *New J. Phys.* **2013**, *15*, 053046.

[201] Shi, X.-Q.; Li, Y.; Hove, M. A. V.; Zhang, R.-Q. Interactions between Organics and Metal Surfaces in the Intermediate Regime between Physisorption and Chemisorption. *J. Phys. Chem. C* **2012**, *116*, 23603–23607.

[202] Davies, P. R.; Edwards, D.; Richards, D. STM and XPS Studies of the Oxidation of Aniline at Cu(110) Surfaces. *J. Phys. Chem. B* **2004**, *108*, 18630–18639.

[203] Björk, J.; Matena, M.; Dyer, M. S.; Enache, M.; Lobo-Checa, J.; Gade, L. H.; Jung, T. A.; Stöhr, M.; Persson, M. STM fingerprint of molecule–adatom interactions in a self-assembled metal–organic surface coordination network on Cu(111). *Phys. Chem. Chem. Phys.* **2010**, *12*, 8815.

[204] Zhang, X.; Gu, G.; Li, N.; Wang, H.; Tang, H.; Zhang, Y.; Hou, S.; Wang, Y. One-dimensional molecular chains formed by Sierpiński triangles on Au(111). *RSC Advances* **2018**, *8*, 1852–1856.

[205] Schlickum, U.; Klappenberger, F.; Decker, R.; Zoppellaro, G.; Klyatskaya, S.; Ruben, M.; Kern, K.; Brune, H.; Barth, J. V. Surface-Confined Metal-Organic Nanostructures from Co-Directed Assembly of Linear Terphenyl-dicarbonitrile Linkers on Ag(111). *J. Phys. Chem. C* **2010**, *114*, 15602–15606.

[206] McIntyre, N. S.; Cook, M. G. X-ray photoelectron studies on some oxides and hydroxides of cobalt, nickel, and copper. *Anal. Chem.* **1975**, *47*, 2208–2213.

[207] VandeVondele, J.; Krack, M.; Mohamed, F.; Parrinello, M.; Chassaing, T.; Hutter, J. Quickstep: Fast and accurate density functional calculations using a mixed Gaussian and plane waves approach. *Comput. Phys. Commun.* **2005**, *167*, 103–128.

[208] Hutter, J.; Iannuzzi, M.; Schiffmann, F.; VandeVondele, J. cp2k: atomistic simulations of condensed matter systems. *WIREs Comput Mol Sci* **2013**, *4*, 15–25.

[209] Grimme, S.; Antony, J.; Ehrlich, S.; Krieg, H. A consistent and accurate ab initio parametrization of density functional dispersion correction (DFT-D) for the 94 elements H-Pu. *J. Chem. Phys.* **2010**, *132*, 154104.

[210] Goedecker, S.; Teter, M.; Hutter, J. Separable dual-space Gaussian pseudopotentials. *Phys. Rev. B* **1996**, *54*, 1703–1710.

[211] VandeVondele, J.; Hutter, J. Gaussian basis sets for accurate calculations on molecular systems in gas and condensed phases. *J. Chem. Phys.* **2007**, *127*, 114105.

[212] Ochs, O.; Heckl, W. M.; Lackinger, M. Immersion-scanning-tunneling-microscope for long-term variable-temperature experiments at liquid-solid interfaces. *Rev. Sci. Instrum.* **2018**, *89*, 053707.

[213] Bushell, J.; Carley, A. F.; Coughlin, M.; Davies, P. R.; Edwards, D.; Morgan, D. J.; Parsons, M. The Reactive Chemisorption of Alkyl Iodides at Cu(110) and Ag(111) Surfaces: A Combined STM and XPS Study. *J. Phys. Chem. B* **2005**, *109*, 9556–9566.

[214] Lischka, M.; Fritton, M.; Eichhorn, J.; Vyas, V. S.; Strunskus, T.; Lotsch, B. V.; Björk, J.; Heckl, W. M.; Lackinger, M. On-Surface Polymerization of 1,6-Dibromo-3,8-diiodpyrene—A Comparative Study on Au(111) Versus Ag(111) by STM, XPS, and NEXAFS. *J. Phys. Chem. C* **2018**, *122*, 5967–5977.

List of Figures

List of Tables